Hydrodynamic effects in a paraxial fluid of light

Wei Liu

SORBONNE UNIVERSITÉ

Laboratoire Kastler Brossel
Physique quantique et applications

PhoQuS
Photons for Quantum Simulation

THÈSE DE DOCTORAT
DE SORBONNE UNIVERSITÉ

Spécialité : Physique

École doctorale nº564: Physique en Île-de-France

réalisée sous la direction de Dr. Quentin Glorieux

au Laboratoire Kastler Brossel

présentée par

Wei Liu

Sujet de la thèse :

Hydrodynamic effects in a paraxial fluid of light

soutenue le 12 10 2022

devant le jury composé de :

Mme	Pruvost Laurence,	DR,	Université Paris-Saclay,	Rapporteure
M.	Qin Zhongzhong,	PR,	Shanxi University,	Rapporteur
Mme	Minguzzi Anna,	DR,	Université Grenoble Alpes,	Examinatrice
M.	Larré Pierre-Élie,	CR,	Université Côte d'Azur,	Examinateur
Mme	Schwob Catherine,	PR,	Sorbonne Université,	Examinatrice
M.	Glorieux Quentin,	MCF,	Sorbonne Université,	Directeur de thèse

Contents

Introduction and context of this work

General context

When I first stepped into this laboratory, a question that puzzled me for a long time was how it could be possible to describe light as a fluid. So I would like to review the key findings theoretically and experimentally at the beginning with the aim of introducing certain simple concepts that will be helpful for understanding this manuscript and will open up the door to the quantum fluids of light.

What comes to mind when I mention fluid? A slow-moving stream or a raging waterfall? A spring breeze on the face or a north wind blows leaves off the trees in autumn. Of course, all of these are fluids. Fluids exist everywhere and at every moment. Nevertheless, can you imagine that there exists a kind of fluid characterized by frictionless flow due to zero viscosity? In other words, without any loss of kinetic energy in the whole process of flowing? They are called superfluids. Superfluids can flow through narrow capillaries or slits without dissipating energy, which gives rise to certain striking phenomena. For example, when the superfluid encounters an obstacle, it flows around without any disturbances. Another interesting phenomenon is a superfluid placed in a container will escape spontaneously by moving up the walls of the container to cascade on its edges [1, 2]. These landmarks and phenomena have given rise to broad experimental and theoretical research in quantum fluids. There are several approaches to creating superfluids. A fluid is placed in a rotating vessel, the fluid does not move with the vessel under critical velocity [3]. Another approach is to place the classical fluid in a rotating state and then cool it below a critical point. At this moment, if the rotational mechanism is removed, the superfluid will rotate indefinitely.

To explain this phenomenon, Allen [4], Misenerand simultaneously Kapitza [5], decided to measure the resistance to the flow of liquid Helium clamped in narrow channels and subjected to a pressure drop. They found that while the so-called He-I phase, (Helium above the lambda temperature), showed behavior that could be described in terms of a conventional viscosity. While below the lambda point (in the so-called He-II phase), the liquid flowed so easily that the concept of viscosity was not applicable at all. It was this anomalous behavior for which Kapitza coined the term ”superfluidity”. Superfluidity is one of the most striking manifestations of quantum many-body physics.

In 1938, London first recognized that the superfluidity observed in liquid ^{4}He was related to BEC from the fact that the transition temperature of the superfluid and the temperature of BEC were the same under the same experimental conditions. Bose-Einstein condensates (BEC) is Einstein's proposal for a phase transition of non-interacting atomic gases based on Bose's theory which attempted to explain the quantization of light by quantum statistics [6]. This phase transition is associated with particles occupying the lowest energy quantum state and sharing the same wave function at low temperature. The phase transition from the thermal gas of non-interacting atoms to BEC occurs when the thermal de Broglie wavelength $\lambda_T = \left(\frac{2\pi\hbar^2}{mk_BT}\right)^{1/2}$ become comparable or larger than the distance of the average particle $n^{-1/3}$ [6], where the m is the particle mass, $\hbar$ is the reduced Planck constant, k_B is the Boltzmann constant, T is the temperature and the $n = N/V$ is the particles number density of N particles occupying the volume V. According to this condition, we could arrive at the critical temperature for condensation: $T_c \approx \frac{(2\pi\hbar)^2 n^{2/3}}{mk_B}$. This means that the ensembles of bosons will form a Bose-Einstein condensate under this critical temperature T_c and the essence of this transition is the approximation of the phase coherence over macroscopic distances. Initially, it was extensively considered that Bose-Einstein condensates take place only for non-interacting particles. However, scientists found surprisingly that weakly interacting particles would be helpful for the formation of condensation [7]. For weakly interacting Bose-gas, it will give rise to the spectacular phenomenon of superfluidity, which results from the combination of quantum degeneracy and interparticle interaction. Even though Einstein predicted the Bose-Einstein condensation of non-interacting gas in 1925. The first experimental creation of Bose-Einstein condensates (BECs) was realized in atomic gases using cooling the alkali metal atoms with the lasers and magnetic evaporate tools in the laboratory after seven decades [8, 9, 10]. Compared to Superfluid helium failed to explain the fact that the ideal gas model due to strong interactions [11]. The Bose Einstein Condensate is easy to control with high precision. So numerous people turn their attention to atomic quantum gases.

Although cold atomic gas is viewed as an ideal platform for the study of superfluidity, many alternative systems and configurations have emerged to study this interesting physical phenomenon. Different experimental platforms are essential to explore the same phenomena in order to gain a better understanding and reveal their physical nature. For example, some of the scientists has started wondering whether light can be considered a fluid composed of many photons with sizable photon-photon interactions in appropriate situation.

However, in a vacuum, the interaction between photons is so weak that it is usually ignored. But it is possible for us to improve the cross-section of photons in their collision process. In the presence of a third-order non-linear medium, the nonlinear polarization of nonlinear optical media is capable of mediating interactions between photons resulting in photon coupling strength enhanced. A multi-photon system behaves as a collective quantum fluid in this case.

Quantum fluids of light are a photonic counterpart to atomic Bose gases and are defined by the hydrodynamic interpretation of the electromagnetic field, which connects photons in an optical laser beam mediated by the nonlinear optical response of the medium to an analog quantum system with interparticle interactions [12, 13].

There are different configurations for this nonlinear optical system to get the strong nonlinearity to study collective behavior. One example developed at LKB since 2003 such as the exciton-polariton gas in a microcavity. Under low temperatures, semi-conductor materials comprising exciton, a quasi-particle consisting of electron and hole attracted to each other by the electrostatic Coulomb force, interact with photons and give rise to a quasi-particle, refereed to polariton [14]. The polariton can be seen as constituting a mixture of a state of half-light and half-matter. The optical nonlinearity is enhanced thanks to the relatively strong interactions between excitons. The effective photon mass arises from the spatial confinement of the photon by planar mirrors. In addition, it is noted that the wave function of polaritons almost shares similar dynamics to the interacting atomic Bose-Einstein condensates except for an additional dissipation term, which arises from the fixed lifetime of the polariton. So now it is clear that exciton-polariton gas in microcavity undergoes Bose-Einstein condensates [12]. These polaritons all move in the same direction, like a flowing fluid, and possess great advantages compared to atomic BEC. First of all, polaritons are easier to condense in the ground state since the polariton have a lighter mass: the polaritons exhibit the Bose-Einstein condensates at higher temperatures from several kelvins [15] up to the room temperature [16] (around eight orders of magnitude larger than the atomic Bose-Einstein condensates) and with lower densities. More, it offers possibility of fully reconstructing both the density and the phase pattern of the polariton condensate from the properties of the emitted light. It has been realized huge achievements via this system, for example the superfluity of polariton around the defect [17] and the hydrodynamic nucleation of nonlinear excitations such as solitons [18] and quantized vortices [19, 20, 21] in dilute photon gases. Nevertheless, this method has some limitations. On the one hand, the effective interaction is slightly tunable because it strongly relies on the exciton-exciton coupling, which makes obtaining strong enough nonlinearities in scalable systems to study the dynamics of a strongly interacting photon gas turns out to be a major experimental challenge. On the other hand, the driven-dissipative nature of polariton introduces severe complications in the theoretical description of such systems and which is typically detrimental for the study of purely quantum features [22].

To overcome the above shortcomings, another alternative route to the regime is the cavityless system based on intriguing laser paraxial propagating in a Kerr nonlinear medium, whose refractive index depends on the laser intensity. Paraxial fluid density depend on a direct mathematical comparison between the Gross-Pitaevskii equation (GPE), which characterizes the mean field evolution of the weakly-interacting Bose-Einstein condensate (BEC), and the nonlinear Schrödinger equation (NLSE), which describes light propagation through a $\chi^{(3)}$ nonlinear medium within the so-called paraxial and slowly-varying-envelope approximations [23]. If we

further apply the Madelung transformation to express the electric field as a function of density and phase, we can get a set of hydrodynamic-like equations. It is straightforward that a sufficiently strong laser field $E(r,t)$ in a nonlinear medium behaves as a photon fluid. The fluid, whose density corresponds to the field intensity, flows at the gradient of the phase as an effective velocity in the plane perpendicular to the propagation along the optical-axis coordinate z. In other words, the propagation direction of the laser beam along the z axis in this photon fluid system replaces the effective time t in BEC. It is this time-space role exchange that makes the evolution of the beam obtained at successive planes along the propagation direction correspond to snapshots of the analogue fluid system at specified moments [24]. And the reason why this platform is referred to as (2D+1) dimensional geometry is that the t direction corresponds to a third spatial dimension in addition to the transverse x and y directions. In this paraxial-propagation of laser field in the nonlinear medium configuration, light diffraction provides an effective mass to the photon in the (x,y) plane and chromatic dispersion leads to a, typically different, effective mass in the t direction. The effective coupling between photons comes from the polarization of the nonlinear medium. So now you will be clear that the fluid of light is referred to as weakly interacting photons formed by a strong laser beam propagating through a nonlinear medium [13]. It has been reported that thermal optic liquid [25, 26], photorefractive crystal [27, 28], as well as the alkaline metal vapors [29, 13, 30] are ideal candidates for the nonlinear medium.

Our fluid of light group in LKB mainly explores the hydrodynamic behavior of the photon fluid in the warm rubidium vapors. Compared to the thermal optic liquid and photorefractive crystal, this fluid of light configuration is developed and applied thanks to the strong nonlinearity under a near-resonance excitation. The rubidium vapor cell will exhibit an intensity-dependent refractive index from a non-zero third-order dielectric susceptibility $\chi^{(3)}$. The Kerr nonlinearity of the medium gives rise to repulsive photon-photon interactions. By mediating this parameter, we can easily tune the interaction strength between photons [31, 32, 33, 34, 35]. Recent extensive reviews and hydrodynamics phenomena have been studied and explored based on this platform as a potential analog quantum simulator, including the demonstrations of superfluidity of light [36, 37, 38], the observation of the Berezinskii-Kosterlitz-Thouless transition [39], shockwaves [29, 40, 41] and precondensation [31], quantum turbulence [42], the creation of analogue rotating black hole geometries [43], the evidence of photon droplets [44].

With this simple configuration, we imprint analogues of short Bragg pulses on a photon fluid by wavefront shaping using a spatial light modulator to measure the static structure factor $S(k)$. The results demonstrate the presence of pair-correlated excitations, revealing indirectly the quantum depletion in a paraxial fluid of light. We also discuss how the relatively small fluctuations superimposing upon a coherent light field in the weak-nonlinearity regime can be treated within the framework of the Bogoliubov theory of dilute Bose-Einstein condensates.

One of the main predictions of quantum field theory concerns the possibility of producing

pairs of particles by exciting vacuum fluctuations. Furthermore, a very similar process based on the tearing apart of quantum vacuum fluctuations by an expanding universe explains the creation of the seeds for structure formation. Even though signatures of these effects can still be observed today in the cosmic microwave background (CMB) radiation, direct detection using elementary particles remain missing. To circumvent the difficulties, it has been proposed to use quasiparticles describing collective excitations of some medium. We want to unitize the dynamical Casimir effect, which is the generation of pairs of real particles or photons from the vacuum as a result of a non-adiabatic change of a system parameter or boundary condition to mimic this process. When a coherent light propagates across a weakly nonlinear medium, the photons experience a pair of sudden jumps of the interaction parameter upon crossing the front and the back faces of the nonlinear medium. As a result of these two quantum quenches, the fluid of light gets excited and we calculate the two-body quantum correlations and find the main excitation process consists of the emission of pairs of correlated counterpropagating Bogoliubov phonon. We find the multi-peak structure in the density power spectrum, known as Sakharov oscillations, conventionally discussed in the context of early universe evolution and the anisotropy of cosmic microwave background (CMB) radiation [45].

Another intriguing effect is the existence of quantum vortices predicted by Lars Onsager [46]. A quantum vortex is a density hole with the superfluid circulating the vortex axis [3, 47]. In the typical case, the closed loop circulation in the superfluid should be zero. Nevertheless, if in this region there exist a non-superfluid element, the circulation is quantized: $2\pi\hbar/m$ because the macroscopic wavefunction is a single value at the space coordinate r. It thus implies that vortices only exist with a fixed strength in the quantum fluids, and the quantum vortices sustain any rotational motion of the superfluid. Many of the early studies for the superfluid photon focus on the hydrodynamics of the quantum vortices on the coherent photon fluid. Scientists are interested in quantum vortices because several tangled quantum vortices will give rise to the creation of quantum turbulence, the counterpart of classical turbulence [48]. Turbulence is a disordered state in space and time, characterized by many degrees of freedom interacting nonlinearly over a substantial range of scales, where the kinetic energy of the fluid is transported without loss. Although the behavior of the classical turbulence is too complex, Kolomogrov's power-law scaling of the energy flow has been proposed to describe the steady behavior of the turbulence [49]. In 3D turbulence, a direct cascade of energy and vorticity towards small-length scales emerges when the system is forced at a larger-length scale. Remarkably, restricting the fluid dynamics to two dimensions (2D) results in an inverse cascade process: small-scale forcing leads to an energy flux towards larger scales [50]. Quantum turbulence with disordered tangle quantized vortices flow in the inviscous fluid will aid in comprehending turbulent behavior. It has been reported that oscillating structures such as wires, spheres, and grids are an excellent way to generate quantum turbulence in ^{4}He [51]. And rotating the external potential [52, 53] or two-axis rotation [54] is the essential method for creating vortices in trapped BECs. Moreover, it also has been reported that the hydrodynamic formation of topological excitations such as quantized vortices and dark solitons at the surface of large impenetrable obstacles. While much

great progress has been made in BEC, experimental observation of quantum turbulence in the fluid of light is still missing. Inspired by the first realization of quantum turbulence in the atomic Bose-Einstein condensates and the evidence of the quantized circulation of optical vortices possess similar behaviors like the turbulence in superfluid Helium and the Bose-Einstein condensates [55, 42], we expect to open new windows to explore quantum hydrodynamics in the fluid of light in experiment. With our two counter-streaming fluids of light, we first get the $^{k}-5/3$ Kolmogorov power law in the inertial range in the incompressible kinetic energy spectrum experimentally. The photon fluids have been demonstrated to constitute an effective platform to study quantum turbulence.

Thesis Summary

My thesis is structured as follows.

In chapter 1, I will introduce the concept of fluids of light that are relevant to this manuscript. I review the classical propagation equation of a paraxial beam of light in a cavityless nonlinear optical medium of the Kerr type. Emphasis on describing the nonlinear response when the electromagnetic field propagates through a nonlinear medium. Then I will describe the interaction between the photons and the laser field in the Kerr medium. Next, I will explain the analogy between the Nonlinear Schrödinger Equation (NLSE) and the Gross Pitvaskii Equation (GPE) and mathematically demonstrate that it is reasonable to consider light as a fluid in the case of the electric field propagating in the nonlinear medium. By further comparing the NLSE and hydrodynamics equations, I connect the optics quantities to the hydrodynamics equation to demonstrate that a laser can be considered a fluid whose intensity is equivalent to the density of the fluid and the gradient of the laser phase is related to the velocity of the fluid. We also derive the Bogoliubov dispersion relation, describing the small density waves propagating on top of a uniform background. Finally, Landau criteria are given to define whether a fluid features superfluidity.

In chapter 2, I focus on giving the structure of rubidium to help readers understand why researchers favored this Alkali metal in nonlinear optical experiments. Moreover, I present the atom density, Doppler broadening, and optical depth, which are crucial when considering the laser-atom interaction. Next, I introduce the Saturated Absorption Spectroscopy (SAS) setup used to determine spectral characteristics. Finally, I show how to precisely quantify the rubidium cell's temperature and the nonlinear refractive index that governs photon interaction.

In chapter 3, I will describe the experimental tools that accompany us almost every weekday. Begin with the working principle of the laser source and introduce the light source in our lab. The Spatial Light Modulator (SLM) is then described, which is used to modulate a specific phase of the light field through liquid crystal molecules. Next, I'll talk about the acoustic-optic modulator (AOM), which utilizes sound waves to diffract and modify the frequency of light.

Finally, I'd like to discuss some technical specifics concerning the glass cells that store the rubidium vapor and the homemade heating apparatus.

In chapter 4, I will state how to measure the static structure factor S(k), which characterizes the density-density correlations of the elementary excitations by using Bragg-like spectroscopy, which has proved to be an essential tool to study ultracold atomic BECs. Our platform uses a spatial light modulator to imprint an analogy of short Bragg pulses in the photon fluid. In addition, we also discussed how the relatively small fluctuations superimposed upon a coherent light field in the weak-nonlinearity regime can be treated within the Bogoliubov theory of diluted Bose-Einstein condensates. The dispersion relation that demonstrates a linear phononic regime for photons with weak interactions and low sound velocity. This new technique could also improve the resolution compared to the methods we used before [36, 56].

In chapter 5, with the paraxial quantum fluid of light configuration, we study the sudden change of interaction strength, also known as the interaction quenches that take place at the entrance and exit of the rubidium vapor cell, to simulate expanding and contracting universes. When the laser beam leaves the vapor cell, photon interactions abruptly cease, which causes a sudden red shift in the energy spectrum. This process resembles an expanding universe [45]. We evaluate the density structure factor after the second quench and the observed acoustic peak. This structure, known as Sakharov oscillating, resembles the angular spectrum of CMB radiation.

In chapter 6, I will provide a study of vortex turbulence, by introducing certain definitions necessary for better understanding this phenomenon, characterized by cascades of excitations across length scales. Next, I will present quantum turbulence implemented by two fluids of light with different velocities in the rubidium vapor cell, which is rooted in the resonant energy transfer from the drift velocity to the elementary Bogoliubov excitations of the photon gas. We also explore the whole instability evolution process and observe the Kolmogorov energy cascade from small to large length in an inertial range. We show that the fluid of light is an exciting platform to study quantum turbulence.

Acknowledgements

Throughout the writing of this dissertation, I have received a great deal of support and assistance.

I would first like to thank my supervisor, Quentin Glorieux, whose expertise was invaluable in formulating the research questions and methodology. Your insightful feedback pushed me to sharpen my thinking and brought my work to study. I cannot thank you enough for your invaluable advice, continuous support, and patience during my Ph.D. study. Your immense knowledge and ample experience have encouraged me in all the time of my academic research and daily life.

I would like to thank Murad Abuzarli, who gave me a lot of valuable advice and guidance when I first entered the laboratory. You help me quickly integrate and adapt to the new environment. "Any questions?" makes me feel like it is no longer difficult to ask questions. Thank you for helping me answer my questions during my Ph.D. You are kind, and I will never forget the patience that you gave me.

I would particularly like to acknowledge Myrann Abobaker. We learn from each other and make progress together. You are optimistic and uplifting, and your spirit of never giving up no matter what problems you encounter in the experiment deeply moved me. I thank you for the help in the experiment and life. I wish you all the best in the future.

I also thank Tangui Aladjidi for his valuable advice throughout my studies. Patiently and very carefully pointed out the problems in my experiment. You always find a way to make me better in every presentation. I appreciate all of the talks with you.

Finally, I could not have completed this dissertation without the support of Chengjie Ding, Maxime Jacquet, Clara Piekarski, Ferdinand Claude, Kevin Falque, and Ruggero Giampaoli, who provided stimulating discussions, support as well as happy distractions to rest my mind outside of my research.

Chapter 1

Fluid of light and superfluity

Quantum fluids of light merge many-body physics and nonlinear optics, revealing quantum hydrodynamic features of light when it propagates in nonlinear media. The theoretical framework used to describe quantum fluids of light relies on the analogy with weakly interacting Bose gases and was initially derived by Bogoliubov. I will review the classical propagation equation of a paraxial fluid of light and describe the main steps of the derivation of the well-known paraxial wave equation in a Kerr nonlinear medium. I then analyze the parameters that affect the interaction between photons. I also discuss how the relatively small fluctuations in the weak-nonlinearity regime can be considered sound waves. A fundamental property of the Bogoliubov dispersion relation is the linear dependence in the excitation wave vector at long wavelengths (soundlike) and the quadratic dependence at short wavelengths (free particle-like). Finally, I introduce how to verify a fluid is superfluid.

1.1 Background

Even though photons are fundamentally noninteracting particles in free space, photon propagation in appropriately designed nonlinear optical systems is now attracting growing interest as a novel platform for investigating the physics of interacting Bose gases, also known as quantum fluids of light.

The systems in the so-called strong light-matter coupling regime have emerged as particularly promising for obtaining the relatively strong nonlinear interactions required for collective behavior. A new mixed quasi-particle, the polariton, is created in this regime when the photon is strongly mixed with matter degrees of freedom [14, 18].

An alternative platform for studying many-body physics in photon fluids is provided by light propagating through an optical medium of the Kerr nonlinear type, whose refractive index depends on the strength of the electric field [12]. It has been demonstrated that a sufficiently intense laser propagates in a self-defocusing nonlinear refractive medium, the nonlinearity of the medium gives rise to repulsive force between photons and gives an effective mass to the photon. This particular Kerr medium consists of photo-refractive crystals [57, 37], the thermo-optic media [25, 26], and hot alkaline metal vapor [36, 34]. However, the nonlocality exhibited in the thermal optic liquid media is extremely detrimental to the observation of experimental results. On the other hand, the atomic medium can provide a large nonlinearity that will be beneficial to obtain a wider interaction scale. So our group chooses the hot atomic alkaline vapor as the nonlinear medium [25]. In our experiment, the nonlinearity is induced by the propagation of a near-resonant laser field inside a hot Rubidium atomic vapor. The sign and the strength of the interactions can be finely tuned by adjusting the laser detuning with respect to the atomic resonance. The vapor temperature, which controls the atomic density, adds another layer of control over the strength of the interactions.

In contrast to the microcavity architecture, where a driven-dissipative equation describes the temporal dynamics of the fluid of light, paraxial photon fluid propagation in a nonlinear medium has the following advantages. First of all, the highly sensitive optical detection technology provides the opportunity to precisely measure density and phase distribution. Second, it is simple to produce paraxial photon fluids without a trapping potential and a homogeneous density. In this system, the evolution of the electric field in the transverse plane along the propagation is analogous to the evolution of atomic Bose-Einstein condensates, which describe the dynamics of the wavefunction of the interacting Bose-Einstein condensates in time. The roles played by the optical-axis coordinate z and the time parameter t are exchanged: Light propagation in the z direction is naturally described in terms of evolution equations while the t direction corresponds to a third spatial dimension in addition to the transverse x and y directions. This analogy makes light have fluid properties whose initial density and flow speed is controlled by the intensity and the angle of incidence of the incident beam. Thus, it provides us more chances

to explore hydrodynamics phenomena that benefit from this flexible system [12, 38, 58]. And several phenomena have been observed, from the superfluid around the defect at low speed to the hydrodynamic formation of topological excitations such as the quantum vortex and the dark soliton.

1.2 Quantum fluid of light

This chapter discusses the analogy between this nonlinear propagation and the evolution of a paraxial photon fluid. I first describe the electric field propagating in the nonlinear medium to derive the nonlinear Schrödinger equation. By mapping it to the Gross Pitaevskii equation, the electric field of the laser beam can be regarded as a fluid flowing in the plane perpendicular to the propagation axis. In this section, we derive the propagation of the electromagnetic field in the nonlinear medium. The point is to give information on how to map the optical quantities to the hydrodynamics quantities of the quantum fluid. In other words, how to connect the nonlinear optics to the fluids of light. I also present the theoretical framework required to describe the photon fluids' elementary excitations by introducing Bogoliubov transform and the so-called Bogoliubov dispersion relation.

1.2.1 Nonlinear Schrödinger Equation

When an electromagnetic field E propagates in a nonlinear medium, it takes the form of Maxwell equations:

$$\nabla^2 E - \frac{n^2}{c^2}\frac{\partial^2 E}{\partial t^2} = \frac{1}{\epsilon_0 c^2}\frac{\partial P_{NL}^2}{\partial t^2} \tag{1.1}$$

where In this equation, $\nabla = (\partial x, \partial y, \partial z)$ denotes the nabla operator in the $\mathbf{r}$, E is the amplitude of the electric field, n is the linear refractive index and the c is the speed of light in the vacuum, ϵ_0 is the vacuum permittivity. And the P_{NL} stands for the nonlinear response of the medium to the applied field. If we assume that the wave propagates to the optical axis (z-direction) at a small angle. In such a situation, the field amplitude $E(r, z)$ slowly alters in the r $= (x, y)$ transverse plane (that is, the plane perpendicular to the z-axis). The electrical fields envelop can be expressed as:

$$E = \mathcal{E}(r, z)e^{i(k_0 z - \omega t)} \tag{1.2}$$

where ω is the frequency of the electric field, the $k_0 = 2\pi\omega/c$ is the wavevector in vacuum and $\mathcal{E}(r, z)$ is a slowly-varying function of z . If we insert the above equation into the Eq. 1.1, we can derive the gethe neral propagation equation inside a nonlinear medium.
Here is our derive process:

$$\nabla E = e^{i(k_0 z - \omega t)}\left(\nabla_\perp \mathcal{E} + \frac{\partial \mathcal{E}(r, z)}{\partial z} + ik_0\mathcal{E}\right) \tag{1.3}$$

where the $\perp$ stands for the transverse plane (x, y).

$$\nabla^2 E = ik_0 e^{i(k_0 z-\omega t)}\left(\frac{\partial \mathcal{E}}{\partial z}\right) + e^{i(k_0 z-\omega t)}\left(\frac{\partial^2 \mathcal{E}}{\partial z^2} + ik_0\frac{\partial \mathcal{E}}{\partial z}\right) \tag{1.4}$$

$$= e^{i(k_0 z-\omega t)}\left(\nabla_\perp^2 \mathcal{E} + \frac{\partial^2 \mathcal{E}}{\partial z^2} + 2ik_0\frac{\partial \mathcal{E}}{\partial z} - k_0^2\mathcal{E}\right) \tag{1.5}$$

$$\frac{\partial^2 E}{\partial t^2} = -e^{i(k_0 z-\omega t)}\omega^2\mathcal{E} \tag{1.6}$$

And we also have:

$$\frac{\partial P_{NL}^2}{\partial t^2} = -e^{i(k_0 z-\omega t)}\omega^2\chi^{(3)}\epsilon_0|\mathcal{E}|^2\mathcal{E} \tag{1.7}$$

So the final result is as follows:

$$\nabla_\perp^2 \mathcal{E} + \frac{\partial^2 \mathcal{E}}{\partial z^2} + 2ik_0\frac{\partial \mathcal{E}}{\partial z} - (k_0^2 - \frac{n^2\omega^2}{c^2})\mathcal{E} = -\frac{\omega^2}{c^2}\chi^{(3)}|\mathcal{E}|^2\mathcal{E} \tag{1.8}$$

Under the slowly varying envelope approximation (SEVA), assuming that the amplitude of the envelope $\mathcal{E}$ changes slowly along z axis comparable to the wavelength. We can apply the paraxial approximation, which is valid as long as derivative $\frac{\partial^2 \mathcal{E}}{\partial z^2} \ll \frac{\partial \mathcal{E}}{\partial z} \ll 1$. In this way, we can neglect the second order, so the above equation finally reduces to:

$$\nabla_\perp^2 \mathcal{E} + 2ik_0\frac{\partial \mathcal{E}}{\partial z} - (k_0^2 - \frac{n^2\omega^2}{c^2})\mathcal{E} = -\frac{\omega^2}{c^2}\chi^{(3)}|\mathcal{E}|^2\mathcal{E} \tag{1.9}$$

Then we decompose the refractive index as the sum of the average index and local modulation of the linear refractive index: $n = n_0 + \delta n$. Here, it is worth noting that the modulation δn can be seen as an external potential in the transverse acting on photons and play the role of the defect or a wave guide for the light beam. It can be optically generated in our system by locally driving another rubidium transition with a second laser field tuned close to resonance. Finally, the above equation can be expressed as:

$$i\frac{\partial \mathcal{E}}{\partial z} = \left(-\frac{1}{2k_0}\nabla_\perp^2 - \frac{k_0\delta n}{n_0} - \frac{k_0\chi^{(3)}|\mathcal{E}|^2}{2n_0^2} - i\frac{\alpha}{2}\right)\mathcal{E}, \tag{1.10}$$

This is the Nonlinear Schrödinger equation (NLSE), which describes a spatial evolution of an electric field passing through a Kerr-type medium. The first term on the right side gives us the diffraction information. In the second term, the refractive index modulation acts as the potential and the last one corresponds to the photon-photon interaction. The last term is the linear absorbtion term.

1.2.2 Gross Pitaevskii Equation

The NLSE is formally analogous to the 2D Gross Pitaevskii equation (GPE) except the absorption term. The GPE describes the evolution of the wave function $\Psi(r,t)$ of the weak interaction of the atomic Bose-Einstein condensates in the mean field approximation:

$$i\hbar\frac{\partial\Psi(\mathbf{r},t)}{\partial t} = \left(-\frac{\hbar^2}{2m}\nabla^2 + \mathcal{V}(\mathbf{r}) + g|\Psi(\mathbf{r},t)|^2\right)\Psi(\mathbf{r},t)\ , \tag{1.11}$$

where the $\hbar$ is the Plank constant, m is the boson mass, $\mathcal{V}(\mathbf{r})$ is the external potential (trapping potential, obstacle potential, etc.) and $g = \dfrac{4\pi\hbar^2 a}{m}$ denotes the strength of the interaction characterized by the s-wave scattering length a is the coupling parameter. If the coupling g is positive indicates that the condensate is in a stable state. Conversely, the system is in an unstable state. The coherence length is the GP model's only characteristic length scale. It is defined as follows: $\xi = \dfrac{\hbar}{\sqrt{2mg}|\Psi|}$, estimates the vortex core size. This GPE offers a main theoretical tool for investigating nonuniform dilute Bose gases at low temperatures derived independently by Gross and Pitaevskii [6].

1.2.3 Analogy between the NLSE and GPE

It is worth noting that the NLSE and GPE are similar mathematically. Now, we will comprehensively analyze and compare each term of the Nonlinear Schrödinger equation 1.10 and Gross Pitaevskii equation 1.11.

1. $\Psi(\boldsymbol{r},t) \leftrightarrow \mathcal{E}(\mathbf{r}_\perp, z)$

   The NLSE is a spatial derivative that describes the evolution of the electric field E along the z direction instead of the temporal derivative in GPE. So we can say that the axis coordinate z in the NLSE can be treated as the effective evolution time $\tau = n_0 z/c$ in the GPE through the following space-time mapping: $z \leftrightarrow \tau$. This is a key point that means that every transverse plane of the laser beam in the nonlinear medium can be considered as the evolution of the 2D Bose gas of photons after the corresponding effective evolution time τ. Figure 1.1 graphically illustrates this analogy. More precisely, this space-time mapping allows us to get information on the system's state after an effective time by means of imaging the field at the relevant output plane of the medium. This is the reason why we refer this system to the 2D + 1 geometry. 2D is the transverse plane $r_\perp = (x, y)$ and 1 stand for the time dimension.

2. $\hbar/m \leftrightarrow 1/k_0$

   Another comment is that the mass in the energy term is replaced by a quantity related

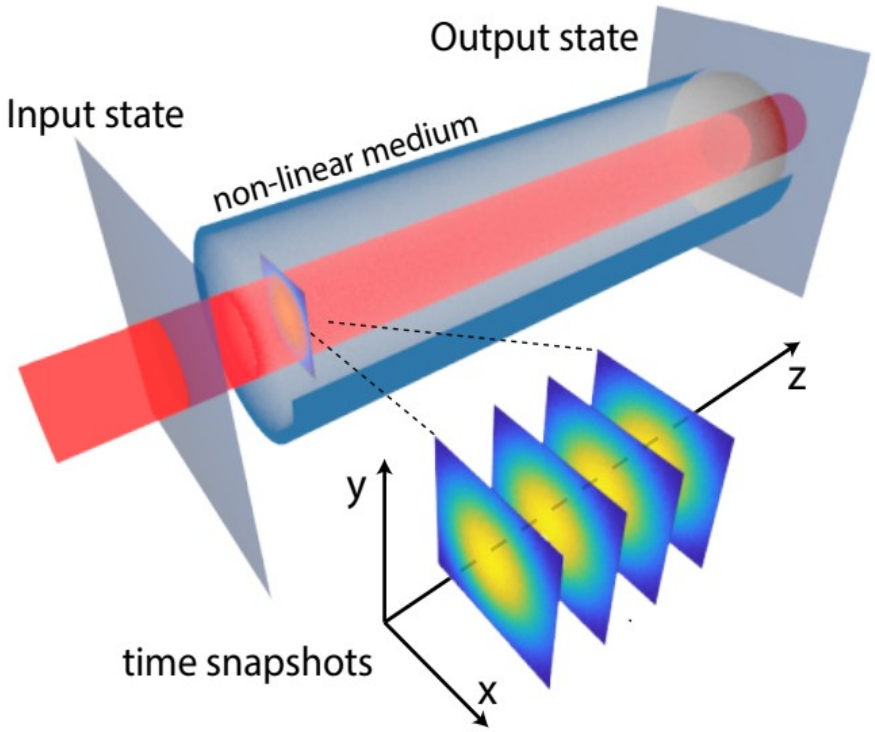

Figure 1.1: Scheme of the propagation of the photon fluid along the optical axis. Each transverse plane in the z-direction is representative of a snapshot of "time evolution".

to the laser wavevector k. So we can derive the effective photon mass by this analogy: $m = \hbar k/c$. This equation is significantly important since it is one of the preconditions that we can consider the electromagnetic field as the fluid of light.

3. $\mathcal{V}(\mathbf{r})/\hbar \leftrightarrow -k_0\delta n/n_0$

   According to the analogy, the external potential act on the photons relies on the refractive index modulation can be rewritten as: $\mathcal{V}(\mathbf{r}) = -\hbar k_0 \delta n$. The attractive (repulsive) potential depends on the sign of the local variations of the linear refractive index δn. So it gives us insight that we can shape the potential by inducing a refractive index modulation with an additional intense laser beam via the optical nonlinearity of the medium. It is worth mentioning that we don't consider this term throughout the text.

4. $g/\hbar \leftrightarrow k_0\chi^{(3)}/2n_0^2$

   By comparing the last term, we can also get the expression for the coupling constant $g = -\hbar\omega n_2$, which characterize the weakly interacting photon gas formed by an electric field inside the Kerr nonlinear medium. We should also be careful that the refractive index n_2 not only controls the strength of the photon-photon interaction but determines whether the interaction is attractive or repulsive (depending on the sign of n_2). For the negative $n_2 < 0$ or the positive $n_2 > 0$ nonlinear refractive index, the medium will have a defocusing or the focusing response corresponding to the repulsive and attractive photon-photon strength, respectively. To make the photon gas system in a stable state, all the experiments throughout this manuscript turn it at the defocusing regime [32]. We also focus on the scenario of a weak nonlinearity, where the observed refractive index modulation is caused by the collective interaction of a large number of photons.

Up to now, it is clear that the photon fluid is an ideal analogue of the BEC with the highly control.

1.2.4 Hydrodynamic analogy

As mentioned above, the comparison between two critical equations tells us that the evolution of light in a nonlinear Kerr medium as a fluid of light along the propagation direction can be regarded as the evolution of an ordinary fluid over time. The photon-photon interaction comes from nonlinear materials. However, there is still a problem that needs to be clarified. Since light under special conditions can be regarded as fluid. How can we establish the connection between electromagnetic fields and hydrodynamics? In other words, how to translate the optics physics quantities to the hydrodynamics quantities. To solve this question, we have to utilize the Madelung transform, which expresses the electric field as the function of density $\rho(\mathbf{r}_\perp, z)$

and the phase $\Phi(\mathbf{r}_\perp, z)$: $\mathcal{E}(\mathbf{r}_\perp, z) = \sqrt{\rho(\mathbf{r}_\perp, z)}e^{i\Phi(\mathbf{r}_\perp, z)}$ [59]. This transformation decompose the NLSE into a set of hydrodynamic equations:

$$\frac{\partial \rho}{\partial z} + \nabla_\perp(\rho v) = 0 \tag{1.12}$$

$$\frac{\partial v}{\partial z} + (v \times \nabla_\perp)v = -\frac{g}{n_0 k_0}\nabla_\perp \rho + \frac{1}{2}\nabla_\perp\left(\frac{1}{\sqrt{\rho}}\nabla_\perp^2\sqrt{\rho}\right) \tag{1.13}$$

These two equations describe the paraxial laser beam in a defocusing Kerr medium as a fluid of density $\rho = |\mathcal{E}|^2$ flows at velocity at $v = \frac{c}{n_0 k_0}\nabla_\perp \phi$ in the transverse plane along the beam propagation plane. In this way, the analogy between photon fluids in propagating geometries becomes clearer: by replacing the role of time in classical fluids with the propagation axis z, light behaves as the fluid that flows at velocity related to the gradient of the phase and its density dependent on the electric field intensity. Moreover, since the $\tau - z$ mapping, the velocity has no unit and corresponds to the angle of the laser. The first equation is the continuity equation, and the second is the well-known Euler equation. The wave character of the system manifests itself through the last term, commonly regarded as the quantum pressure or Bohm potential in the equation 1.13. The quantum pressure can be ignored as long as the density in the transverse plane varies slowly.

We now conclude that with the mapping of $\tau \leftrightarrow z$, we can know the possibility of describing a strong electric field in the nonlinear medium as the fluid of light under the paraxial approximation. With the hydrodynamic equation, it is become clear and straightforward to connect the optics quantities to hydrodynamics quantities. The light intensity corresponds to the fluid density, the spatial gradient of its phase related to the fluid velocity. The hydrodynamic analogy tells us that we can control and manipulate the fluid by shaping the phase of the fluid at the entrance of the cell. Moreover, by mediating the interaction of the photon, we could quickly change the evolution time L/Z_{NL} (where the $Z_{NL} = 1/k_0\Delta n$ is nonlinear length). This means despite always image the same plane of the Rubidium vapor cell, this enables us to see how the fluid changes over time.

1.3 Interaction between light and matter

Now we know that the warm rubidium vapor cell can trigger the interaction between photons when tuning the laser frequency close to the rubidium atom resonance. However, how could we quantify this coupling strength? In the present section, I shall present a brief qualitative description of the nonlinear behavior when a laser propagates in the Kerr medium and the modification of properties of the material system in the presence of the intense laser. We will see in the following that this modification will have a different response to the applied field, which relies on the laser's strength. To characterize this response precisely, we bring the con-

cept of polarization **P**, which plays a key role when we describe the relevant phenomenon of nonlinear optics since it acts as the component of the electromagnetic field.

1.3.1 Interaction between the atom and the light

We can use the Maxwell-Bloch equation, also called the optical Bloch equation, to describe the case of the interaction of the electric field with N two-level atoms consists of ground state $|\psi_g\rangle$ and the excited state $|\psi_e\rangle$. The ω_{eg} is the resonant transition frequency. The wave function of the two-level atoms takes the form of $\psi = c_g\psi_g + c_e\psi_e$. And the Bloch equation is written as follows:

$$\frac{d\hat{\rho}}{dt} = -\frac{i}{\hbar}\left[\hat{H}, \hat{\rho}\right] - \Gamma\hat{\rho} \tag{1.14}$$

where Γ is the spontaneous decay rate (Einstein A coefficient) of the excited states, also called the natural line width of the emitted radiation, which is acquired from inverting the lifetime. $\rho = \begin{pmatrix} \rho_{ee} & \rho_{eg} \\ \rho_{ge} & \rho_{gg} \end{pmatrix} = \begin{pmatrix} c_e c_e^* & c_e c_g^* \\ c_g c_e^* & c_g c_g^* \end{pmatrix}$ denotes atomic density matrix and $\hat{H} = \hat{H}_0 + \hat{V}$ is the Hamiltonian of the system with the unperturbed part $\hat{H}_0 = \hbar\omega_{eg}\,|\psi_e\rangle\,\langle\psi_e|$ and the interaction with light $\hat{V} = -\mathbf{d}\cdot\mathbf{E}$ in the doppler approximation, which means that spatial variation of the electric field at the atomic scale could be negligible. Moreover, we assume that the incident monochromatic field with frequency ω and amplitude $\mathcal{E}_0$, expressed as $\mathbf{E} = \mathcal{E}_0 cos(\omega t)$. It therefore makes sense that interaction between the electric field and the atom can be viewed as a coupling between the electric dipole and the laser electric field.

$$V = -\frac{1}{2}\left(d^*\,|\psi_e\rangle\,\langle\psi_g| + d\,|\psi_g\rangle\,\langle\psi_e|\right)\left[\mathcal{E}_0(e^{i\omega t} + e^{-i\omega t})\right] \tag{1.15}$$

$$= -\frac{\hbar}{2}\left(\Omega^*\,|\psi_e\rangle\,\langle\psi_g| + \Omega\,|\psi_g\rangle\,\langle\psi_e|\right)(e^{i\omega t} + e^{-i\omega t}) \tag{1.16}$$

$\Omega = -\mathcal{E}_0\mu_{eg}/\hbar$ is the Rabi frequency which characterizes the strength of coupling between the atom and the applied field, where μ_{eg} is the dipole moment.
To eliminate the time dependence we define the operator:

$$\hat{U} = exp(-i\hat{H}_0 t/\hbar) = |\psi_g\rangle\,\langle\psi_g| + |\psi_e\rangle\,\langle\psi_e|\,e^{-i\omega t} \tag{1.17}$$

So the interaction term can be written as:

$$V = U^\dagger V U = -\frac{\hbar}{2}\left(\Omega^*\,|\psi_e\rangle\,\langle\psi_g| + \Omega\,|\psi_g\rangle\,\langle\psi_e|\right) \tag{1.18}$$

The matrix density can be written as

$$\rho = U^\dagger \rho U \tag{1.19}$$

Noted that we applied the Rotating Wave Approximation (RWA) that allows us to eliminate the fast-decaying terms. Inserting the above equations 1.18 and 1.19 and rewriting the Bloch equation for slow varying amplitudes $\sigma_{ij}(t)$ of the density matrix elements $\rho_{ij}(t) = \sigma_{ij}(t)e^{-i\omega_{ij}t}$ then determined the following relations:

$$\dot{\rho_{gg}} = i\frac{\Omega}{2}(\sigma_{eg} - \sigma_{ge}) + \Gamma\rho_{ee} \tag{1.20}$$

$$\dot{\rho_{ee}} = -i\frac{\Omega}{2}(\sigma_{eg} - \sigma_{ge}) - \Gamma\rho_{ee} \tag{1.21}$$

$$\dot{\rho_{ge}} = -i\frac{\Omega}{2}(\sigma_{ee} - \sigma_{gg}) - i(\Delta - i\frac{\Gamma}{2})\sigma_{eg} \tag{1.22}$$

where the $\dot{\rho_{ij}}$ is the density element of the density operator. $\Delta = \omega_{eg} - \omega_0$ is the laser detuning from the resonance frequency. The elements ρ_{gg} and ρ_{ee} correspond to the population of the ground state and excited state, respectively. While the $\sigma_{eg} = \sigma^*_{ge}$ correspond the atomic coherence. We can rewrite the equations as:

$$\dot{\rho_{ee}} - \dot{\rho_{gg}} = -i\Omega(\sigma_{eg} - \sigma_{ge}) - \Gamma(\rho_{ee} - \rho_{gg} + 1) \tag{1.23}$$

$$\dot{\sigma_{ge}} = -i(\Delta - i\Gamma - i\frac{\Gamma}{2})\sigma_{eg} - i\frac{\Omega}{2}(\rho_{ee} - \rho_{gg}) \tag{1.24}$$

Take into account the condition that $\rho_{ee}+\rho_{gg} = 1$. And we also assume that $\dot{\rho_{gg}} = \dot{\rho_{ee}} = \dot{\rho_{ge}} = 0$, the solutions could be expressed as:

$$\sigma_{ge} = -\frac{\Omega}{2}\frac{\rho_{ee} - \rho_{gg}}{\Delta - i\Gamma/2} \tag{1.25}$$

$$\rho_{ee} - \rho_{gg} = -\frac{\Delta^2 + \Gamma^2/4}{\Delta^2 + \Gamma^2/4 + \Omega^2/2} \tag{1.26}$$

1.3.2 Atomic polarization

The dielectric medium response to the applied electromagnetic field of laser is the electric polarization **P**. In the isotropic medium, all of the dipoles along the direction of the applied field, the electric polarization **P** could be expressed as:

$$\mathbf{P} = \varepsilon_0\chi\mathbf{E} \tag{1.27}$$

Where the ε_0 is the electric permittivity of the free space, and χ is the electric susceptibility indicating the polarization degree of the dielectric materials in response to the applied field. However, this is valid for the linear case, which means the amplitude of the applied field is extremely small. If the sufficiently strong laser is applied, the situation will become complex and we rewrite the electric polarization as a power series in the field strength, which take the form of:

$$P = \varepsilon_0\left[\chi^{(1)}E + \chi^{(2)}|E|^2 + \chi^{(3)}|E|^3 + ... + \chi^{(n)}|E|^n\right] \tag{1.28}$$

where the $\chi^{(1)}$ is the linear susceptibility and quantity $\chi^{(n)}$ are known as the n-order nonlinear optical susceptibilities which describe the nonlinear response of the medium. For the center symmetric medium, all even terms will vanish. Besides, we neglect all high orders that more than 3-rd terms due to it is too weak to have any effects on the result in our system. Finally we get the formula:

$$P = \varepsilon_0 \chi^{(1)} E + \varepsilon_0 \chi^{(3)} |E|^3 \tag{1.29}$$

The polarization can also be expressed as atomic density matrix:

$$P = N \mu_{eg} \sigma_{eg} \tag{1.30}$$

where N is the atomic density and μ_{eg} is the dipole moment of the transition. Insert the equation 1.25, we can arrive at the polarization of the atomic system:

$$P = -\frac{4N|\mu_{eg}|^2}{\hbar^2 \Gamma^2} \frac{\Delta + i\Gamma/2}{1 + 4\Delta^2/\Gamma^2 + 2\Omega^2/\Gamma^2} \tag{1.31}$$

We write the P as the function of saturation intensity I_{sat}, which is defined as the value of the intensity when the dipole cross section is reduced by half compared to the atom interacting with light in free space at a low-intensity case.

$$\frac{I}{I_{sat}} = 2 \left[\frac{\Omega^2}{\Gamma^2} \right] \tag{1.32}$$

where the laser intensity is given by $I = \frac{1}{2} n_0 \epsilon_0 c E^2$. So we obtain:

$$P = -\frac{4N|\mu_{eg}|^2}{\hbar^2 \Gamma^2} \frac{\Delta + i\Gamma/2}{1 + 4\Delta^2/\Gamma^2 + I/I_{sat}} E \tag{1.33}$$

By performing the Taylor expansion of eq.(1.33) in the case of $I/I_{sat} \ll 1 + 4\Delta^2/\Gamma^2$. The polarization is determined as follows:

$$P \approx -\frac{4N|\mu_{eg}|^2}{\hbar^2 \Gamma^2} \frac{\Delta + i\Gamma/2}{1 + 4\Delta^2/\Gamma^2} \left(1 - \frac{I/I_{sat}}{1 + 4\Delta^2/\Gamma^2} \right) E \tag{1.34}$$

At this moment, we can give the expressions for the total electric susceptibility χ, the linear susceptibility $\chi^{(1)}$ and the 3-rd nonlinear susceptibility $\chi^{(3)}$:

$$\chi = -\frac{4N|\mu_{eg}|^2}{\epsilon_0 \hbar^2 \Gamma^2} \frac{\Delta + i\Gamma/2}{1 + 4\Delta^2/\Gamma^2 + I/I_{sat}} \tag{1.35}$$

$$\chi^{(1)} = \frac{4N|\mu_{eg}|^2}{\epsilon_0 \hbar^2 \Gamma^2} \frac{\Delta + i\Gamma/2}{1 + 4\Delta^2/\Gamma^2} \tag{1.36}$$

$$\chi^{(3)} = \frac{4N|\mu_{eg}|^2}{\epsilon_0 \hbar^2 \Gamma^2 |E|^2} \frac{\Delta + i\Gamma/2}{1 + 4\Delta^2/\Gamma^2} \frac{I/I_{sat}}{1 + 4\Delta^2/\Gamma^2} \tag{1.37}$$

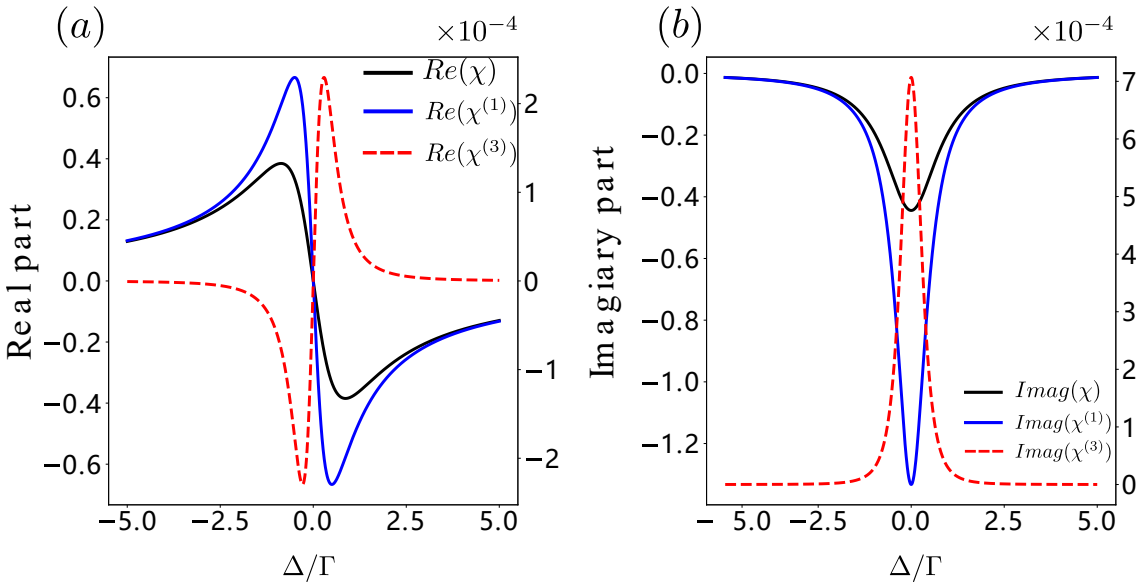

Figure 1.2: Real (a) and imaginary parts (b) of the total (black solid), first order (blue, solid), and third order (red dashed) dielectric susceptibilities. The total susceptibility has been plotted for frequencies $\Omega = \Gamma$. The signs of χ and $\chi^{(3)}$ are opposite since the latter represents a saturation of the optical response. Plots obtained for the D1 line of rubidium 87. Parameters: $T = 423$ K and $N = 8.8 \times 10^{19}$ $atoms/m^3$.

We have plotted the real and imaginary parts of the total electric susceptibility (solid black curve), linear electric susceptibility (solid blue curve) and nonlinear electric susceptibility (red dashed curve) in the figure.1.2. Note that the real part of the electric susceptibility χ is linked to the refractive index of the medium.

$$n_0 = \sqrt{1 + Re(\chi^{(1)})} \tag{1.38}$$

$$n_2 = \frac{3Re(\chi^{(3)})}{n_0^2 \epsilon_0 c} \tag{1.39}$$

And the total refractive index is given by:

$$n = n_0 + n_2 I \tag{1.40}$$

The imaginary part of the electric susceptibility χ is related to the absorption:

$$\alpha = kIm(\chi) \tag{1.41}$$

where the k is the light wavevector in the nonlinear medium. Three comments about these:

- The interaction between the photons is controlled by the nonlinear refractive index, or we say, the 3-rd nonlinear susceptibility $\chi^{(3)}$. It is a rather important parameter in all our experiments since it determines the type of photon-photon interaction and strength.

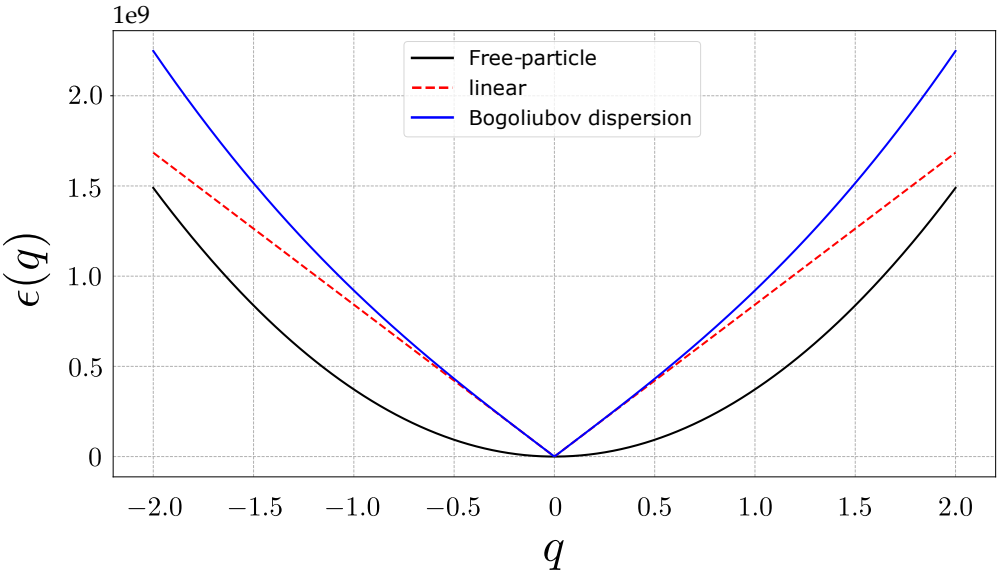

Figure 1.3: Theoretical Bogoliubov dispersion relation (blue solid line) obtained for sound waves and mass particle regimes have been plotted in red dashed line and black solid line.

The sign of the n_2 determines the nature of the interactions: $n_2 > 0$ corresponds to the attractive interaction, and $n_2 < 0$ is the repulsive interaction. And it is noted that in all experiments, we place ourselves in the repulsive regime to have a stable system. From the expression, it is straightforward that the interaction between photons can be modified via two tools: the atomic density N and the detuning Δ. We will see that the atomic density is temperature dependent so we can improve this quantity via increasing temperature detailed in the next section.

- In practice, we always neglect the nonlinear absorption since it is too small. In other words, the absorption of the medium depends on the imaginary part of linear susceptibility $\chi^{(1)}$.

- We expect to have a large photon interaction strength in our experiment. According to the formulation 1.39, it means that a relatively larger nonlinear refractive index is necessary. We can see that the figure 1.2 that the more close the atomic resonance, the more we get a large real part of the susceptibility related to the nonlinear refractive index. In parallel, it is also worth noting that this operation will increase the absorption, preventing the light from being transmitted. So in actual manipulation, we should take into account the trade-off between maximizing the refractive index and a certain fraction of the absorption.

1.4 Bogoliubov dispersion

In general, the equation 1.12 and equation 1.13 can not be solved analytically, so it would be interesting to probe the dispersion relation of the system, which describes the small density

waves propagating on top of a uniform background. The derive process of the Bogoliubov dispersion relation as follows: We decompose the wave function into a mean-field $\psi_0(r,t)$ and plus a small perturbation $\delta\psi(r,t)$,ch take the form as:

$$\Psi(r,t) = [\psi_0(r,t) + \delta\psi(r,t)] \tag{1.42}$$

The unperturbed state condensate wave-function $\psi_0(r,t)$ can be expressed as :

$$\psi_0 = \sqrt{n(r)}e^{-i\mu t/\hbar} \tag{1.43}$$

where the $n(r)$ is the density of the condensate and the μ is the chemical potential. For a uniform system, the μ is governed by $\mu = |\psi_0|^2 g = ng$. The solution of the $\delta\psi(r,t)$ take the form of:

$$\delta\psi(r,t) = [u(r)e^{-i\omega t} - v^*(r)e^{i\omega t}]e^{-i\mu t/\hbar} \tag{1.44}$$

This dispersion relation corresponds to a modified two-branch Bogoliubov. Inserting this into the linearized Gross-Pitaevskii equation, we obtain two coupled equations for $u(r)$ and $v(r)$, known as Brogoliubov equations:

$$[\frac{\hbar^2}{2m}\nabla^2 + gn - \hbar\omega]u(r) - gnv(r) = 0$$
$$[\frac{\hbar^2}{2m}\nabla^2 + gn + \hbar\omega]v(r) - gnu(r) = 0$$

Consider the commutation relation for bosonic creation $\hat{a}^\dagger$ and the annihilation operators $\hat{a}$:

$$[\hat{a}, \hat{a}^\dagger] = 1 \tag{1.45}$$

Define a new pair of operators:

$$\hat{b} = u_q\hat{a} + v_q\hat{a}^\dagger \tag{1.46}$$
$$\hat{b}^\dagger = u_q^*\hat{a}^\dagger + v_q^*\hat{a} \tag{1.47}$$

For the complex number u^* and v^* are the Hermitian conjugate of the u and v. The Bogoliubov transformation is the canonical transformation mapping the operators $\hat{a}$ and $\hat{a}^\dagger$ to $\hat{b}$ and $\hat{b}^\dagger$.

$$[\hat{b}, \hat{b}^\dagger] = (|u_q|^2 - |v_q|^2)[\hat{a}, \hat{a}^\dagger] \tag{1.48}$$

In the case of $|u_q|^2 - |v_q|^2 = 1$, the transformation is invariance. And the form of this condition is suggestive of hyperbolic identity. We can take the $u(r)$ and $v(r)$ as the form of plane wave,

$$u(r) = u_q e^{iqr}, v(r) = v_q e^{iqr} \tag{1.49}$$

And then we insert these two equations into the above equations, and finally, we obtained the called Bogoliubov dispersion:

$$(\hbar\omega)^2 = \left[\frac{\hbar^2 q^2}{2m} + gn\right]^2 - (gn)^2 \tag{1.50}$$

Take the positive energy solution and finally, we arrive at the following:

$$\epsilon(q) = \hbar\omega(q) = \epsilon_0(q)[\epsilon_0(q) + 2gn] \tag{1.51}$$

$\omega(q)$ defined in Eq.1.51 corresponds to the well-known Bogoliubov dispersion relation for the elementary excitations propagating on top of a uniform dilute Bose-Einstein condensate at rest [6]. Here the $\epsilon_0 = \hbar^2 q^2/2m$ is the energy of free particle without interaction. From this we can conclude that in the case of $\epsilon_0 \ll 2gn$, in other words, in the small q, the energy would become:

$$\epsilon_0 = \hbar\sqrt{\frac{gn}{m}}q = \hbar c_s q \tag{1.52}$$

where the $c_s = \sqrt{gn/m}$ is the speed of sound, and the physical meaning is that the spectrum will behave as a linear shape (phonon-like). The linear dispersion relation guarantees superfluidity. While for the larger q, the dispersion becomes quadratic, massive free-particle-like. The energy is plotted in the solid blue curve in Fig.1.3. The red dashed, and solid black curves represent the sound and particle regimes, respectively.

Transposing to the current optical case, for small amplitude modulations moving on a uniform background fluid at rest, the set of hydrodynamic equations can be linearized assuming $\rho = \rho_0 + \delta\rho$ and $v = v_0 + \delta v$. For a plane wave, the dispersion relation describes the response frequency of the fluid of light to a small density fluctuation $\delta\rho$ of wavevector $\mathrm{k}_\perp$ on top of a spatially uniform fluid of light at rest. It has the form:

$$\Omega_B = \sqrt{\frac{k_\perp^4}{4k_0^2} + k_\perp^2 \Delta n} \tag{1.53}$$

The Bogoliubov dispersion relation governs the dynamics of the density fluctuations on top of the photon fluid. Within space-time mapping, Ω_B has units of an inverse length. When the wavelength of the modulation is larger than the healing length: $\xi = \dfrac{1}{k_0}\sqrt{\dfrac{n_0}{|\Delta n|}}$, the Bogoliubov dispersion relation is linear, and density excitation propagates as collective sound waves. This regime is characterized by the speed of sound: $c_s = \sqrt{\dfrac{|\Delta n|}{n_0}}$ which scales as the square root of the fluid density and in dimensional units since the physical meaning of it is propagation angles with respect to the z-axis. When the wavelength of the modulation is smaller than the healing length, the dispersion relation becomes parabolic. Excitations have then been a particle-like behavior: they propagate in the transverse plane as "massive" free particles. They

may be interpreted physically as a particle being excited out of the Bose-condensed cloud into the high-momentum state of wavevector $k_\perp$, where it travels at high speed through the fluid. It is worth noting that, as a consequence of the space–time $t \leftrightarrow z$ mapping underlying the Schrödinger equation 1.10, frequencies $\Omega_B(k_\perp)$ are measured in inverse lengths and speeds like v, c_s and $v_{gr} = \nabla_k \Omega_B(k_\perp)$ are measured in adimensional units, as they have the physical meaning of propagation angles with respect to the z-axis.

1.4.1 Landau's criterion of superfluidity

Superfluidity is the remarkable property of flow without friction. It is characterized by the absence of excitations when the fluid hits a localized static obstacle at flow speeds v_{flow} below some critical velocity v_c. The transformation laws of energy and momentum under Galilean transformations play a major role in Landau's theory of superfluids. Let E and $\mathbf{P}$ represent the fluid's energy and momentum in a reference system K, respectively. The energy and momentum of the system K', which is moving with velocity $\mathbf{V}$ relative to K, are given by [6]:

$$E' = E - \mathbf{P} \cdot \mathbf{V} = \frac{1}{2} M V^2, \mathbf{P}' = \mathbf{P} - M\mathbf{V} \tag{1.54}$$

where M is the total mass of the fluid. Consider a homogeneous fluid at zero temperature flowing at constant velocity through a capillary $\mathbf{v}$. If the fluid is viscous, the motion will cause energy dissipation, resulting in heating and a decrease in kinetic energy. In the following, we will focus on dissipative processes resulting from the generation of elementary excitations. Let us describe the process in the reference frame moving with the fluid. Suppose a single excitation with momentum $\mathbf{p}$ emerges in the fluid. In that case, the total energy is $E_0 + \varepsilon(p)$, where E_0 and $\varepsilon(p)$ are the energy of the ground state and the excitation, respectively. And $\mathbf{p}$ is the momentum carried by the fluid. Let us now go to the reference system where the capillary is at rest. In this frame, which moves with respect to the fluid with velocity $-\mathbf{v}$, the energy E' and momentum P' are given, according to Eq. 1.54, by:

$$E' = E_0 + \varepsilon(\mathbf{p}) + \mathbf{p} \cdot \mathbf{v} + \frac{1}{2} M v^2, \mathbf{P}' = \mathbf{p} - M\mathbf{v} \tag{1.55}$$

Equation 1.55 demonstrates that the values $\varepsilon(\mathbf{p}) + \mathbf{p} \cdot \mathbf{v}$ and $\mathbf{p}$ represent the change in energy and momentum caused by the emergence of the excitation. As a result, we may deduce that $\varepsilon(\mathbf{p}) + \mathbf{p} \cdot \mathbf{v}$ represents the energy of an elementary excitation in the frame when the capillary is at rest. The critical issue here is that the process of spontaneous excitation production can occur only if it is energetically 'profitable', that is if the excitation energy is negative:

$$\varepsilon(\mathbf{p}) + \mathbf{p} \cdot \mathbf{v} < 0 \tag{1.56}$$

If $v > \varepsilon(\mathbf{p})/p$, the sample can transfer the momentum $\mathbf{p}$ to the capillary. In this case, the flow of the fluid is unstable, and its kinetic energy will be transformed into heat. If the velocity is smaller than the value

$$v_c = min\frac{\varepsilon(\mathbf{p})}{p} \tag{1.57}$$

where the minimum is calculated over all the values of $\mathbf{p}$, then the condition 1.56 is never satisfied, and no excitation will spontaneously grow in the fluid. Landau's criterion for superfluidity can then be written in the form

$$v < v_c \tag{1.58}$$

The Landau criterion for superfluidity states that below some critical flow velocity v_c, the background fluid can no longer transfer kinetic energy by exciting density fluctuation. In other words, there will be a persistent flow without friction, and the liquid will exhibit superfluidity.

By looking at the Bogoliubov excitation spectrum 1.50, one easily concludes that the weakly interacting Bose gas fulfills the Landau criterion for superfluidity and that the speed of sound gives the critical velocity. We can note that for a parabolic dispersion of the elementary excitations $\varepsilon(p) \propto p^2$, the density waves are created as soon as an obstacle is dropped into the flow for arbitrary small fluid, and the critical velocity is 0. On the other hand, a linear dispersion $\varepsilon(p) \propto p$ will allow for superfluidity. Here, we should note that Landau's argument is only valid for weak perturbations that do not significantly alter the condensate density and speed [60]. Otherwise, the dissipation of the superfluid will not occur in the form of phonon excitation but at the expense of creating the solitons (high velocity) and vortices (low velocity) even if the velocity below the critical velocity [61, 21].

Chapter 2

Rubidium structure and properties

In this chapter, I will describe some of the physical effects we must consider when light propagates through a nonlinear medium and the measurement of some critical experimental parameters. I first introduce the rubidium level structure with a two-level description, which mainly helps introduce the basic concepts and understand why we chose Rubidium: hot alkaline vapors provide strong nonlinearity under a near-resonance excitation. We also describe the atomic density's dependence on temperature. Then I state the Doppler broadening result from the inhomogeneous atom velocity distribution and the optical depth, which is the natural logarithm of the ratio of incident to transmitted radiant power through a medium. The measurements were performed to access the vapor temperature T. Finally, the most critical measurement of the nonlinear refractive index n_2 is presented.

2.1 Rubidium Structure

The rubidium vapor cell contains two isotopes, ^{85}Rb and ^{87}Rb in their natural abundances of 72.17% and 27.83%, respectively [62, 63]. It is widely used in atomic physics and quantum optics experiments because its resonance is close to a common laser source. Moreover, it is relatively flexible to control them with specific tunable parameters. With these advantages, there is no doubt that rubidium is the best candidate for quantum optics experiments. We work with Rubidium as the ingredient since it has been developed for many years. And the cell filled with high-quality alkaline vapors is easy to handle. In addition, we can design it into different shapes according to various experimental purposes. In the beginning, I would like to present the fine and hyperfine structure of the rubidium. We take the example of the ^{85}Rb, which has two D lines.
The D1 line: $5^2S_{1/2}$ to $5^2P_{1/2}$ transition.
The D2 line: $5^2S_{1/2}$ to $5^2P_{3/2}$ transition.

Among these two transitions, the D2 transition is used extensively in the quantum and optics experiments since its cycling transition is important for the cooling and trapping ^{85}Rb. The $5^2S_{1/2} \rightarrow 5^2P_{3/2}$ and $5^2S_{1/2} \rightarrow 5^2P_{1/2}$ transitions are the components of a fine-structure doublet, and each of these transitions has a hyperfine structure. The fine structure is a result of the coupling between the orbital angular momentum $\mathbf{L}$ of the outer electron and its spin angular momentum $\mathbf{S}$. The total electron angular momentum is then given by:

$$\mathbf{J} = \mathbf{L} + \mathbf{S} \tag{2.1}$$

And the values of the $\mathbf{J}$ just can taken in this range: $|L - S| \leq J \leq L+S$. For the ground state of ^{85}Rb, $L = 0$ and $S = 1/2$, so $J = 1/2$. For the excited state of ^{85}Rb, $L = 1$ and $S = 3/2$, so the J take the value of $J = 1/2$ or $J = 3/2$.
The hyperfine structure results from the coupling between the $\mathbf{J}$ and the total nuclear angular moment $\mathbf{I}$. As a result, the total atomic angular moment is written as:

$$\mathbf{F} = \mathbf{J} + \mathbf{I} \tag{2.2}$$

The magnitude of the F take the value of $|J - I| \leq F \leq J + I$.
For the ground state of ^{85}Rb, the $J = 1/2$ and the $I = 5/2$, so the value of the $F = 2$ or $F = 3$. For the excited of the ^{85}Rb D2 line, F takes the values of $F = 1, 2, 3, 4$. And the excited of the ^{85}Rb D1 line, F take the values of $F = 2, 3$. And the relevant ^{85}Rb transition hyperfine structure showed in fig.2.1(a).

Two level atom

It is a little sophisticated for the hyperfine structure of the Rubidium. When we deal with the problem involving the interaction between atoms and light, we can use a two-level atom approx-

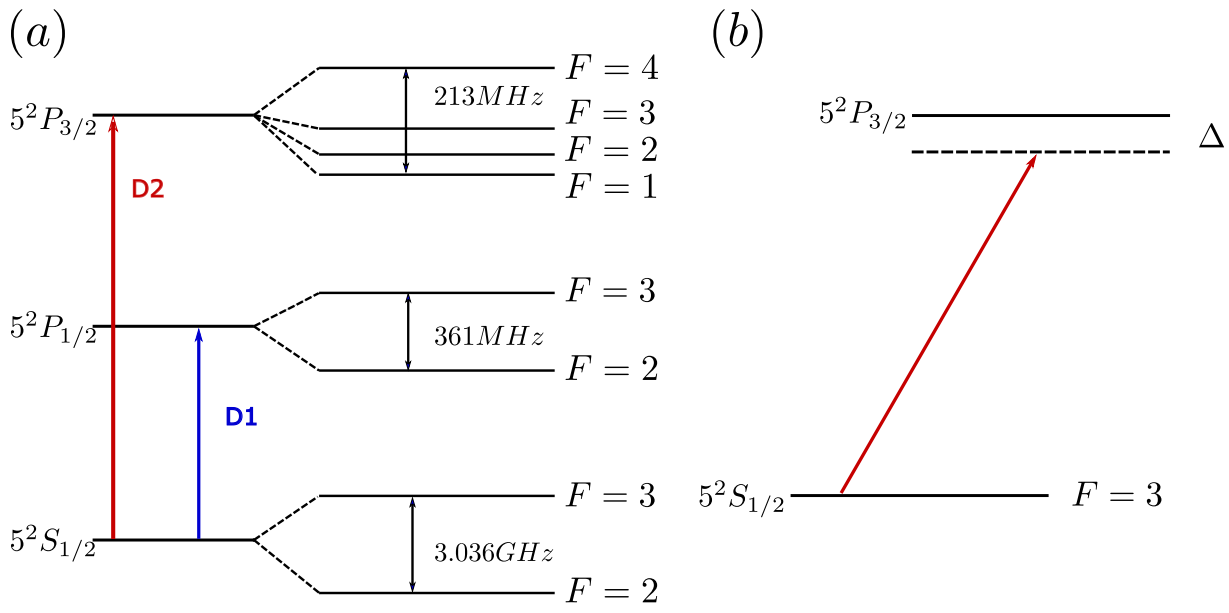

Figure 2.1: Rb 85 hyperfine structure and Two level structure

imation under certain conditions. As shown in the figure.2.1(b), we only consider $5S_{1/2}, F = 3$ and $5P_{3/2}$ level to simply this system to the two-level structure in most problems. As mentioned before, when a sufficiently strong beam passes through a Kerr medium, the laser electric field's evolution can be considered a fluid of light. And we aim to study the hydrodynamic behavior of the quantum fluid of light. Before introducing this, I would like to present some essential tools to characterize the medium's properties.

2.2 Physics properties

2.2.1 Atomic density

In the Rubidium vapor cell, the pressure for the fluid rubidium depends on the temperature T given by [64]:

$$log_{10}p = 15.88253 - \frac{4529.635}{T} + 0.00058663 \times T - 2.99138 \times log_{10}T \tag{2.3}$$

where p is the pressure in Torr and the T corresponds to the temperature in K. Now we can calculate the atomic number density in the rubidium cell depending on the vapor pressure, namely, the ideal gas law:

$$N = \frac{133.323 \times p}{k_B T} \tag{2.4}$$

The factor of 133.323 converts the vapor pressure from Torr to Pa. The k_B is the Boltzmann constant. Since there are two isotopes present in the cell, the number densities need to be calculated separately according to their abundance. We plot the vapor pressure and the atomic

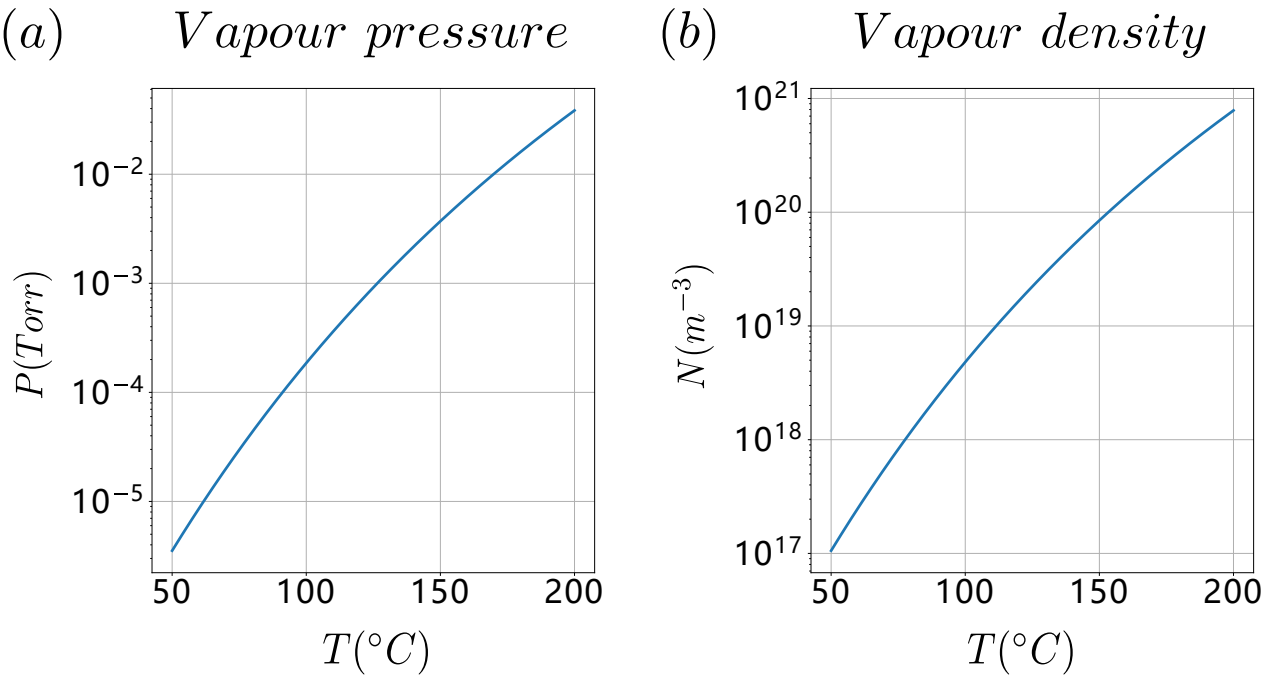

Figure 2.2: Pressure and the density of the atoms in the vapour cell as a function of the temperature from $T = 50°C$ to $T = 200°C$.

density as a function of temperature in figure 2.2(a) and figure 2.4(b) from $50°C$ to $200°C$. As we have discussed before, atomic density is crucial to mediate the nonlinearity. So to improve the interaction between the photons, we can increase the atom density by increasing the temperature of the medium. At room temperature, the vapor pressure of the Rubidium cell is $p = 1.87 \times 10^{-7}$ torr and the corresponding atomic density is $N = 6.1 \times 10^{15}\ m^{-3}$. The vapor pressure of the Rubidium cell is $p = 7.2 \times 10^{-4}$ torr and the corresponding atomic density is $N = 1.76 \times 10^{19}\ m^{-3}$ in the case of the Rubidium vapor cell is heated at $T = 120°C$.

2.2.2 Doppler broadening

When the laser field enters the nonlinear medium, the atoms will move in any arbitrary direction with different velocities. The atoms propagating along the beam will experience photons at the frequency $\nu = (1 + v/c)\nu_0$, also known as blue detuned (at a higher frequency), whereas atoms traveling to the direction of the beam will experience photons at the frequency $\nu = (1 - v/c)\nu_0$, or red detuned (lower frequency). Different velocities give rise to different Doppler shifts. This cumulative effect leads to the Doppler broadening of the spectral line and will result in a spectrum with broad dips and a gaussian profile rather than narrow peaks at the transition frequencies. This effect is more apparent in the Rubidium vapor cell at a high temperature. A particular case results from the increase of the temperature of the cell. Since the thermal average velocity of the atoms along the axis of the probe beam is governed by the Maxwell-Boltzmann distribution $u = \sqrt{2k_BT/m}$. Where the T is the temperature of the vapor cell

and the k_B is the Boltzmann constant and the m is the atomic mass. In warm atomic vapor, the Doppler broadening effect is significant to understand the dynamics of the system. As the Doppler broadening could be greater than the linewidth Γ. For an atom of a mass m at the temperature T, the Doppler linewidth Γ_D takes the form of:

$$\Gamma_D = \sqrt{\frac{k_B T}{m\lambda^2}} \tag{2.5}$$

At $150°C$, the Doppler linewidth $\Gamma_D \approx 265$ MHz for the Rb D_2 line, compared to the $\Gamma \approx 6$ MHz.

2.2.3 Optical depth

The Beer-Lambert law describes how an atomic vapor with uniform density will absorb a monochromatic laser field traveling in the z-direction. It can be expresed as:

$$I(z) = I_0 exp(-\alpha L) \tag{2.6}$$

where $I(z)$ is the intensity at the position z, and the I_0 is the initial intensity at the entrance of the medium. The α is the linear absorption coefficient proportional to the atom density and depends on the frequency of the incident light as well as the temperature of the medium. It takes the form of the following:

$$\alpha = N\sigma_0 \tag{2.7}$$

where the σ_0 is the resonant cross-section, and N is the atomic number density. Noted that the Beer-Lambert law only valid when the absorption α is independent of the initial intensity. To achieve this, we must make the intensity of incoming field weak enough. In this way, the absorption α is the only function of the temperature. On the one hand, the atomic density is a function according to eq.2.4. On the other hand, the atomic cross-section is proportional to the square root of the temperature.

In reality, what attracts our attention is the situation when we add a detuning between the laser field frequency and the atomic transition. In this case, we have:

$$\sigma(\Delta) = \frac{\sigma_0}{1 + 4(\Delta/\Gamma)^2 + I/I_{sat}} \tag{2.8}$$

With this formula, we can estimate the absorption coefficient of the medium. The optical depth OD is the natural logarithm of the ratio of the transmitted radiant power through the media materials to the incident one. According to this definition, we can arrive at the expression of optical depth:

$$OD = -ln\left(\frac{I(z)}{I_0}\right) \tag{2.9}$$

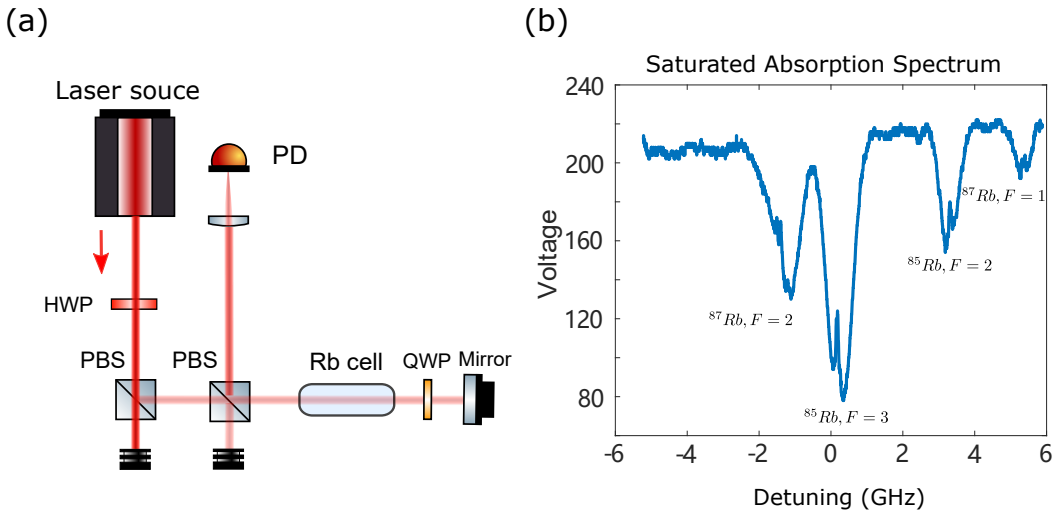

Figure 2.3: (a) Saturated absorption spectrum setup. The laser beam traveling in the right direction is called the pump beam. The second weak reflected by the mirror overlapping laser beam propagating in the opposite direction is called the probe beam. The probe beam is sent to a photodetector (PD) to measure the intensity. (b)Typical absorption spectrum for a rubidium vapor cell. The frequency difference between two ground state $F = 2$ and $F = 3$ for ^{85}Rb is 3.035 GHz, 6.8 GHz for ^{87}Rb between $F = 2$ and $F = 1$.

And in our case, it is equal to the product of the α and the length of the medium L. So if the $OD = 1$, only $e^{-1} = 0.377$ energy passes through the medium without being extinct. For the hot rubidium vapor and the laser close to resonance, the OD can arrive at the order of 10^3. The benefit of using optical depth is that we use the dimensionless quantity to instead of real physical distance.

2.2.4 Saturated Absorption Spectroscopy and frequency locking

The frequency stability of light sources is critical in quantum optics for the majority of experiments to be successful. For example, the generation of quantum entanglement and the areas that use it, such as quantum information or quantum metrology. This point is especially important when it involves light-matter interaction. Meanwhile, precise atomic spectroscopy is one of the most important scientific applications of lasers. Not only spectroscopy is used to comprehend the structure of atoms better, but it is also utilized to create standards in metrology. The second, for example, is determined by atomic clocks using the hyperfine transition frequency in atomic cesium. At the same time, the meter is defined from the wavelength of lasers locked to atomic reference lines.

Saturated absorption spectroscopy is a straightforward and widely used method for deter-

mining narrow-line atomic spectral characteristics. The experimental setup is illustrated in Figure.2.3(a). A powerful pump beam comes from the laser resource passes through the rubidium vapor cell and is reflected on the mirror. There will be a weak probe beam propagating the atomic vapor cell for the second time in opposite directions. And a quarter-wave plate (QWP) alters the polarization state of light and directs the probe beam to the photodetector (PD), which measures the intensity of the probe beam while the laser frequency is scanned. When the probe frequency ν corresponds with the atomic resonance ν_0, atoms will absorb light jump from the ground state $|g\rangle$ to the excited state $|e\rangle$, which results in probe beam absorption around the atomic resonance.

Fig.2.3(b) shows the Saturated Absorption Spectrum (SAS) of the rubidium atom. And the peaks show hyperfine transitions between the ground states to the hyperfine states as well as crossover transitions. Because the Rb cell contains the two most common isotopes, we can see four peaks correspond to ^{85}Rb ($F = 2, F = 3$) and ^{87}Rb ($F = 2, F = 3$). The frequency difference between the 1st and the 4th peaks is the ground state hyperfine splitting in Rb^{87} ($\approx 6.8\ GHz$). The frequency difference between the 2nd and the 3rd peaks is the ground state hyperfine splitting in Rb^{87} ($\approx 3.0\ GHz$). We can find there appears an extra spike at the atomic resonance frequency. This spike arises for the following reasons: If the laser frequency is $\nu_0 - \Delta\nu$, the probe beam is absorbed exclusively by atoms traveling toward the probe beam with longitudinal velocity $v \approx c\Delta\nu/\nu_0$. These atoms see the probe beam blueshifted into resonance. Other atoms do not contribute to probe absorption because they are not in resonance with the probe beam. The pump beam is in the opposite direction, so these atoms feel redshift further away from resonance and are unaffected by it. Situation changes if $\nu = \nu_0$. Since the pump and probe beams counter-propagate inside the rubidium cell. The only atoms that can resonate with both lasers simultaneously are those with a zero velocity $v = 0$ projection on the optical axis. The pump beam is strong enough to maintain a large percentage of the atoms in the excited state without the capacity to absorb the probe beam. In that case, the absorption of the probe beam is reduced by the saturation induced by the pump. As a result, at $\nu = \nu_0$, the probe absorption becomes smaller. The reason why people named it saturated absorption spectroscopy is that the pump beam completely saturates the atoms.

Knowing the frequency of the laser is especially important for exploring the hydrodynamic properties of fluid of light. We usually use the following method to determine the detuning of our laser, so as to lock the laser at the frequency we want. When a voltage within a certain range scans the frequency of the laser, we can obtain the saturation absorption spectrum of the Rb atom. And these two waveform can be shown in oscilloscope. Research on the transitions of atoms is well-determined. By calculating the frequency difference between two absorption peaks and the corresponding range of voltage variation between these two frequencies, we can know the voltage corresponding to each frequency. If we assume that the frequency varies linearly with the scanning voltage. The laser frequency is controlled and locked by calculating the corresponding voltage.

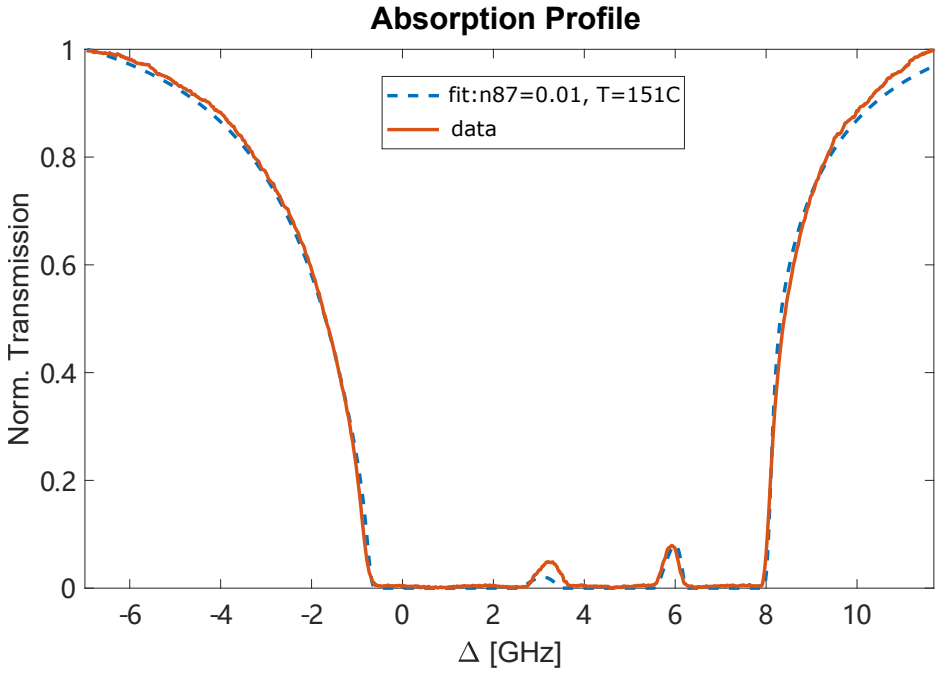

Figure 2.4: Transmission of the laser beam through the rubidium vapor cell as a function of the detuning Δ between the laser and the atomic resonance with respect to the ^{85}Rb $D2$ transition of $5S_{1/2}(F = 2) - 5P_{3/2}(F = 1,\ 2,\ 3)$. According to the transmission profile fit to the theory value allows us to deduce the temperature of the gas $T = 151°C$.

2.3 Rubidium cell temperature measurement

As we discussed before, the temperature of the vapor cell is a key parameter because it is capable of tuning the interaction between the photons. So it is necessary to know its precise value. However, the thermocouple can not characterize the actual temperature of the medium as the low accuracy. To extract atomic gas temperature, we measure the transmission of a weak laser beam after propagation through the vapor as a function of the laser detuning. Specifically, we utilize a sufficiently weak probe beam passing through the hot rubidium vapor. The laser frequency is scanned around 10 GHz. The transmission can be calculated at different detunings by measuring the power ratio of the laser before and after the medium. We always realize it by directing the incoming and transmitted light to the photodetector (PD). And the photodetector connected to the oscilloscope (OS) to show the waveform. The frequency reference is obtained from the saturated absorption spectrum of figures 2.3(b) with the setup 2.3(a). Since the energy levels of rubidium atoms and the frequency corresponding to each peak have been well understood. We can fit the experimental transmission data with a numerical simulation taking into account atomic lines of both isotopes, rubidium vapor pressure as a function of the temperature and the Doppler broadening. The fitting curve gives us information about the temperature T and the isotopic fraction in the vapor cell. It is noted that the choice of the

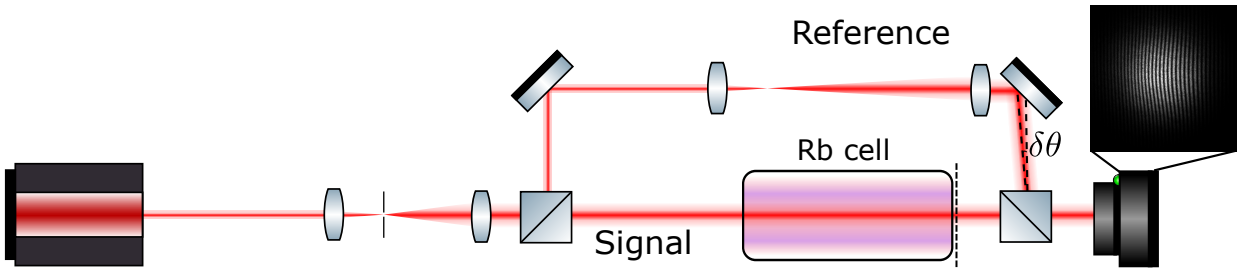

Figure 2.5: Experimental setup used to measure the nonlinear refractive index.

power of the probe beam is a trade-off between two competing effects. On the one hand, a weak probe can ensure enough absorption. On the other hand, a higher probe beam power gives us a good signal-noise ratio.

Our result is shown in figure.2.4. The blue curve shows the transmission spectrum for rubidium vapor at 7.5 cm long at $150°C$. And the orange one shows the predicted theoretical line. Intuitively, the experiment curve has a good agreement with the theory. We can also learn that the percentage of Rb 87 is 1%.

2.4 Nonlinear refractive index measurement

As we have discussed before, when the fluid of light propagates in a nonlinear medium, the interaction between photons depends on the nonlinear refractive index n_2. This quantity plays, therefore, an essential role in helping us to mediate photon fluid physics. But how characterize this parameter? It has been reported that using z-scan [65, 66] and the ring patterns in the far fields [31, 67] to measure the nonlinear refractive index. However, these two methods all have their limitations. All these methods require the Gaussian beam to keep the intensity profile during propagation process. It is obviously not suitable for light passing through a defocusing Kerr nonlinear medium, the nonlinear medium behaves as a negative lens so that the light diverges. So we turn our attention to considering a Gaussian beam propagating in the medium. It will give rise to a nonlinear refractive index variation since the beam's intensity at the center is stronger than its edge, directly leading to an accumulation of the phase. This self-induced phase modulation acts on the beam and behaves as a lens, focusing or defocusing the laser beam depending on the attractive or repulsive photon interactions. By measuring this nonlinear phase shift as a function of intensity, we can thus calculate the nonlinear refractive index n_2.

Our team proposed a different way based on the wavefront measurement using interferometric techniques [33]. The technique rely on measuring the phase difference between the reference beam and a beam that interacted with the nonlinear medium. The core idea is to place the non-linear medium in one arm of a Mach-Zehnder interferogram and use phase retrieval to re-

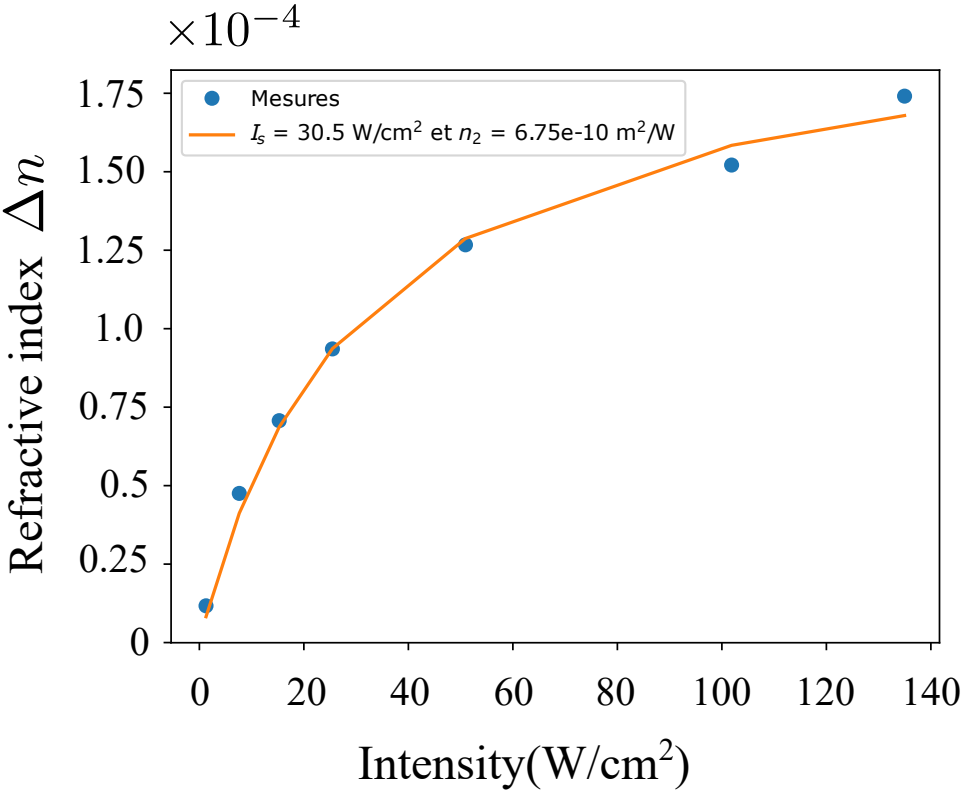

Figure 2.6: Refractive index as a function of intensity.

construct the accumulated phase from the interferogram. The experimental configuration used to measure the refractive index based on the Mach-Zehnder interferometer is shown in fig.2.5. A laser source is split into two arms and recombined with an angle θ to modulate the signal through the interferences. The image plane of the camera is shown by the dashed line after the cell. From the images on the camera, we can see two interesting phenomena: an enlargement of the beam size with the increase of the power. It is caused by the defocusing effect arising from the diffraction of the beam. Another thing is that the interference fringes become increasingly curved with the increase of the power resulting from the nonlinear phase accumulation of the laser in the nonlinear medium. We should be careful that the reference beam needs to be collimated, and the probe beam should be small enough in the practical experimental implementation. We have talked before that the nonlinear refractive index is $\Delta = n_2 I$. Note that this equation is only valid at low power. When we take account into the saturation intensity [68], the nonlinear refractive index can be expressed as follows:

$$\Delta n = n_2 I = n_2 + \frac{I}{1 + \frac{I}{I_s}} \tag{2.10}$$

The intensity detected on the camera as a function of $\mathbf{r} = (x, y)$ is given by:

$$\begin{aligned} I_{cam}(\mathbf{r}) &\propto |\mathcal{E}(r, L) + \mathcal{E}_r(r, L)e^{i\mathbf{k}_r\mathbf{r}}|^2 \\ &= I(\mathbf{r}, L) + I_r(\mathbf{r}, L) + 2\sqrt{I(\mathbf{r}, L)I_r(\mathbf{r}, L)}cos(\mathbf{k}_r\mathbf{r} + \varphi(\mathbf{r}) + \phi_0) \end{aligned} \tag{2.11}$$

In this equation, $\mathbf{k}_r = k_0\theta$ accounts for the relative tilt, I is the intensity of the beams, $\varphi(\mathbf{r})$ is the signal beam's phase, and ϕ_0 is a constant stemming from the reference beam's phase. And the accumulated nonlinear phase linked to the nonlinear refractive index Δn can be expressed as:

$$\psi_{NL}(r) = k_0 L \Delta n = k_0 L n_2 \frac{1}{L} \int_0^L I(z, r) dz \tag{2.12}$$

Where L is the length of the cell. According to the Beer-Lambert law eq. 2.6, taking the linear absorption into account, we arrive at the following form:

$$\psi_{NL}(r) = k_0 L n_2 I_0 \frac{1 - e^{-\alpha L}}{\alpha L} \tag{2.13}$$

Compared to the z-scan or the ring pattern methods, it is easier and more flexible to implement. More details of this method can be found in [33]. The nonlinear refractive index as a function of power is shown in the figure.2.6. The blue dots are the experimental data, the orange curve is the fitting curve according to the theory. We measured Δn and extracted the nonlinear coefficient n_2 and the saturation I_s. From the curve we can see that the $n_2 = 6.75 \times 10^{-2}\ m^2/W$ and the absorption intensity is $I_s = 30.5\ W/cm^2$.

Chapter 3

Useful experimental tools

In this chapter, I would like to introduce the experimental tools used to produce and characterize such paraxial fluids of light. Understanding their working principles is beneficial to experiment. I first briefly present how the laser sources work. Then, I describe the Spatial Light Modulator (SLM), used to modulate a particular phase of the light field through liquid crystal molecules to characterize the photon fluid's properties. Next, I focus on the acousto-optic modulator (AOM), which uses the acousto-optic effect to diffract and shift the frequency of light using sound waves. Finally, I would like to show some technical details about the glass cells containing rubidium vapor and the homemade heating system designed to control its temperature.

3.1 Laser source

A laser is a device that emits light through an optical amplification process achieved by the excited emission of electromagnetic radiation. The main difference between it and ordinary light sources, like the light from the incandescent lamp, lies in its spatial and temporal coherence. Spatial coherence guarantees that the laser can travel long distances without diffraction, thus focusing on a small spot and increasing the power of the light. Temporal coherence ensures that the output light has a narrow spectral range, thereby making the light monochromatic.

Generally speaking, the number of atoms in the lower energy levels is greater than the number in the higher energy levels. At this stage, the system being in thermal equilibrium, the number of photons absorbed by the atomic system per unit of time is greater than the number of photons produced by the stimulated emission. The stimulated absorption of the atomic system plays a dominant role. To obtain laser light, the number of atoms in the excited state must be greater than the number of atoms in the ground state. This process can be achieved by the atoms absorbing the energy of the pump source, which keeps the particle number inversion. For example, the kinetic energy of the electrons excites the laser material through a gas discharge, which breaks the thermal equilibrium of the system and thus puts it in a non-thermal equilibrium state. When the number of atoms excited by radiation per unit time exceeds the number of atoms excited by absorption, the light rays are enhanced. The process of achieving a higher number of atoms at the energy level than at the lower energy level is the particle number inversion.

There are three elements to laser generation: pump source, gain medium, and optical resonator.

1. Pump source: The working material absorbs the external energy and excites the electrons from the low to the high energy level, thus providing the possibility to achieve and maintain the particle number inversion. The most common excitation devices are optical excitation, gas discharge excitation, and chemical excitation.

2. Gain medium: It absorbs the energy from the pump source to excite the electrons from a lower energy level to a higher energy level. This results in light amplification using stimulated emission. The characteristics of lasers include low divergence, high power, good monochromaticity, and good coherence. The power of light at a specific wavelength through the gain medium is increased.

3. Optical resonator: It consists of two mirrors parallel to each other, one fully reflective and one partially reflective. The distance between the two mirrors plays a selective role in the output laser. On the one hand, the optical resonator provides optical feedback capability, allowing the excited radiation photons to make several round trips in the cavity to form coherent and continuous oscillations so that the excited light achieves sufficient amplification to escape from the partially reflective mirror. On the other hand, it can

limit the direction and frequency of the oscillating beam in the cavity to ensure that the output light has a certain direction and monochromaticity.

3.2 Spatial Light Modulator

A spatial light modulator is a device that can modulate a certain parameter of the light field through liquid crystal molecules. It works as follows: the spatial light modulators contain several independent units that are spatially arranged in one- or two-dimensional arrays, each of which can independently receive control of an optical or electrical signal and change its optical properties according to this signal. Such as by modulating the amplitude of the light field, modulating the phase through the refractive index, modulating the polarization state through the rotation of the polarization plane, or realizing the incoherent-coherent light conversion, to write certain information into the light wave and achieve light wave modulation. It can easily load information into an optical field and take advantage of the wide bandwidth of light and parallel processing of multiple channels to process the loaded information quickly. It is the core device that constitutes the system of real-time optical information processing, optical interconnection, optical computing, etc.

In our photon fluid configuration, the initial fluid density and its flow velocity can be easily tuned to control the transverse intensity distribution and the spatial phase profile of the incident laser beam at the medium entrance plane by the spatial light modulator (SLM).

3.3 Acousto-optical modulator

When the ultrasonic wave through the medium causes local compression and elongation of the medium and produces elastic strain, the medium appears sparse and dense phenomenon in time and space, equivalent to the phase grating, and results in a corresponding change in the refractive index of the medium. In this case, the diffraction phenomenon will occur when the light passes through, which is called the acoustic-optical effect. Due to the development of laser technology and ultrasound technology, the acousto-optic effect has been widely used.

There are two types of acoustic-optical effects: normal acoustic-optical effects and anomalous acoustic-optical effects. The interaction of sound and light in all homogeneous media does not cause changes in the polarisation state of the incident light, resulting in normal acoustic-optical effects. Sound-light interaction in all anisotropic media can induce changes in the polarisation state of the incoming light, resulting in anomalous acoustic-optical effects. The anomalous

Figure 3.1: Spatial light modulator produced by HOLOEYE company.

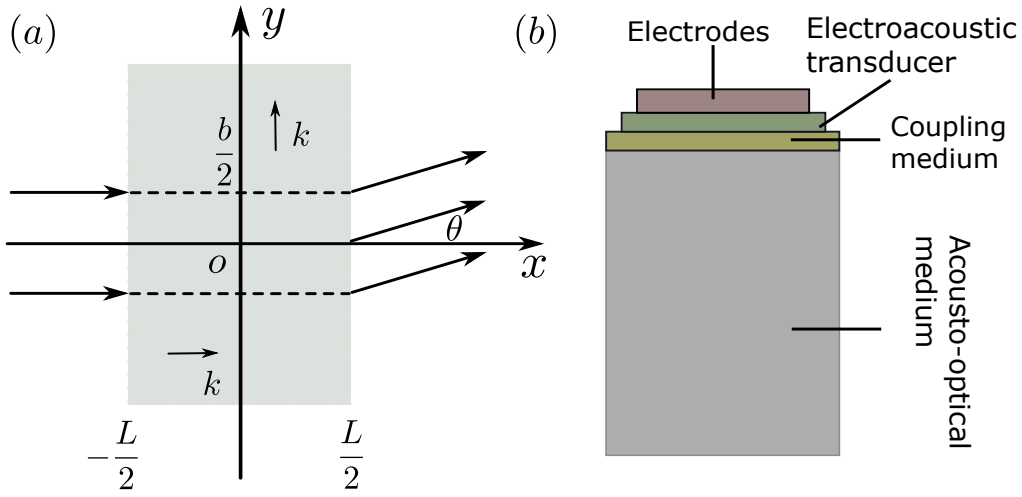

Figure 3.2: (a) Acousto effect diffraction (b) Schematic diagram of the internal structure of the acousto-optic modulator

acoustic-optical effect is the foundation for developing high-performance acoustic-optical deflectors and tunable filters. The Raman-Nass optical grating theory can account for normal acoustic-optical phenomena but cannot account for abnormal acoustic-optic events.

In an acousto-optic medium, an ultrasonic traveling wave is a plane longitudinal wave moving in the y direction with an angular frequency of ω_s, a wavelength of λ_s, and a wave vector of $\mathbf{k}_s$. In the medium, incident light is a plane wave moving in the x direction with an angular frequency ω, the wavelength of λ, and wavevector $\mathbf{k}$. The elastic strain within the medium propagates with the sound wave as a traveling wave. Because the speed of light is approximately 10^5 times that of sound, the change in the period of the medium in space throughout the light wave's passage may be regarded as fixed. The change in the refractive index of the medium due to the strain is determined by the following equation:

$$\Delta(1/n^2) = PS \tag{3.1}$$

where n is the refractive index of the medium, S is the strain and P is the coefficient of photoelasticity. Typically, P and S are second-order tensors. When sound waves propagate in an isotropic medium, P and S can be treated as scalars and, as mentioned earlier, the strain also propagates as a traveling wave so that it can be written as:

$$S = S_0 sin(\omega_s t - k_s y) \tag{3.2}$$

When the strain is small, the refractive index as a function of y and t can be written as:

$$n(y,t) = n_0 + \Delta n sin(\omega_s t - k_s y) \tag{3.3}$$

Where n_0 is the refractive index of the medium in the absence of ultrasound, Δn is the amplitude of the change in the refractive index of the acoustic wave, which can be found by 3.1 equation:

$$\Delta n = -\frac{1}{2} n^3 P S_0 \tag{3.4}$$

If the beam is incident vertically ($\mathbf{k} \perp \mathbf{k}_s$) and passes through a medium of thickness L, the phase difference between the front and rear points is:

$$\Delta\Phi = k_0 \Delta n(y,t) L = k_0 n_0 L + k_0 \Delta n sin(\omega_s t - k_s y) L \tag{3.5}$$

Here we define $\Delta\Phi_0 = k_0 n_0 L$ as the phase difference between the front and rear points of the light wave in the absence of ultrasound, k_0 is the magnitude of the wave vector of incident light in a vacuum. The second term $\delta\Phi_0 = k_0 \Delta n L$ is the phase modulation caused by the ultrasound. Assume that the optical vibration on the incident plane $x = -\frac{L}{2}$ is $E_i = Ae^{it}$, where A is a constant or a complex number. Considering the change of phase and modulation of the points on the incident plane $x = \frac{L}{2}$, the result of the superposition of diffracted light at a point far

from the incident plane in the xy plane is:

$$E = Ce^{i\omega t}\int_{-b/2}^{b/2} e^{i\delta\Phi sin(k_s y-\omega_s t)}e^{ik_0 y sin\theta}dy \tag{3.6}$$

where b is the beam width, θ is the diffraction angle and C is a constant. Using a constant equation related to the Bessel function $e^{iasin\theta} = \sum_{-\infty}^{\infty} J_m(a)e^{im\theta}$, where $J_m(a)$ is a type I Bessel function. Expanding and integrating equation 3.6 gives:

$$E = Cb\sum_{-\infty}^{\infty} J_m(\delta\Phi)e^{i(\omega-\omega_s)t}\frac{sin[b(mk_s - k_0 sin\theta)/2]}{b(mk_s - k_0 sin\theta)/2} \tag{3.7}$$

Since the function $sin(\theta)/\theta$ takes the maximum in the case of $\theta = 0$.So the maximum diffraction angle $\theta_m$is given by:

$$sin(\theta_m) = m\frac{k_s}{k_0} = m\frac{\lambda_0}{\lambda_s} \tag{3.8}$$

where the λ_0 is the light wavelength in the vacuum, λ_s is the ultrasound wavelength in the medium. Compared with the general grating equation, it can be seen that the ultrasonic wavelength in a medium with strain is equivalent to the d of the spacing between the slits of a normal grating. From equation 3.8, the frequency ω_m of the m-th level of diffracted light is

$$\omega_m = \omega - m\omega_s \tag{3.9}$$

It is clear that diffracted light is still monochromatic but with frequency shifted. When the distance of the acousto-optic action satisfies $L > 2\lambda_s^2/\lambda$ and the beam is incident obliquely at an angle with respect to the ultrasonic wavefront. In the ideal case, only level 1st or -1st diffraction occurs in addition to level 0. This is shown in Figure 2. This diffraction is very similar to the Bragg diffraction of X-rays by crystals and is therefore called Bragg diffraction. The angle of incidence of the beam that produces this diffraction is called the Bragg angle. At this point, the medium in which the ultrasonic waves are present acts as a volume grating. It can be shown that the Bragg angle satisfies the following:

$$sini_B = \frac{\lambda}{\lambda_s} \tag{3.10}$$

Because the Bragg angle is generally small, the angle of deflection of the diffracted light with respect to the incident light is written as:

$$\Phi = 2i_B \approx \frac{\lambda}{\Lambda_s} = \frac{\lambda_0}{nv_s}f_s \tag{3.11}$$

where v_s is the wave speed of ultrasound, f_s is the frequency of ultrasound. Under Bragg diffraction conditions, the efficiency of the first level of diffracted light is

$$\eta = sin^2 \left[\frac{\pi}{\lambda_0} \sqrt{\frac{MLP_s}{2H}} \right] \tag{3.12}$$

where P_s is the ultrasonic power, L and H are the length and width of the ultrasonic transducer, respectively. M is a constant reflecting the nature of the acousto-optic medium itself. From equations 3.11 and 3.12, it can be seen that by varying the frequency and power of the ultrasonic waves, control of the laser beam direction and modulation of the intensity can be achieved respectively, which is the basis of the acousto-optic deflector and acousto-optic modulator. The driving power supply is used to generate the modulating signal applied to the electrodes at both ends of the transducer, which uses the inverse voltage effect of certain piezoelectric crystals or piezoelectric semiconductors to generate mechanical waves under the action of the applied electric field. When a beam of light through the changing mechanical wave field, light and mechanical waves interact in the dielectric region. The outgoing light has time-varying levels of diffracted light. And the use of diffracted light intensity with the mechanical wave intensity changes the nature of the light intensity modulator. The opposite of the general mechanical wave source prevents an absorption device for the absorption of mechanical waves that have passed through the medium. Grating is an essential optical element. A grating is broadly defined as an optical element that allows the amplitude or phase (or both) of incident light to be spatially modulated periodically. Gratings that can only subject light to amplitude modulation or phase modulation are called amplitude gratings and phase gratings, respectively. Gratings can be divided by mode of operation into transmission gratings (where the transmitted light is modulated) and reflection gratings (where the reflected light is modulated.) The number of marks per unit length of the grating is mainly determined by the wavelength range of the light being divided (the distance between the two marks should be similar to the order of magnitude of the wavelength), the more marks per unit length, the greater the dispersion. The number of marks determines the resolving power of the grating. By grating, we mean a diffraction grating that uses the diffraction effect to modulate light.

3.4 Vapour cell

The Rb atomic cell is the non-linear medium for our system to create the fluid of light. It plays an important role in enhancing the coupling between photons and photons. The cells can be filled with a mixture of Rb85 and Rb87 vapor in different proportions depending on the specific experimental purpose. As previously described, the length of the rubidium vapor cell is proportional to the evolution time of the photon fluid. This means that we can observe the hydrodynamics of the photon at different times by changing the length of the cell provided that

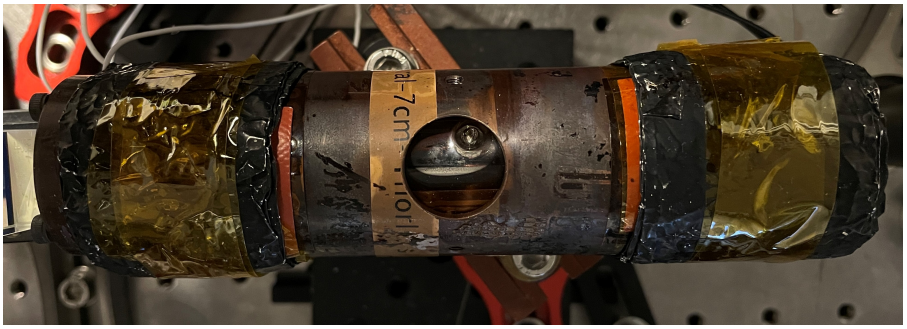

Figure 3.3: Rubidium vapor cell heating system. A 5 cm Rubidium atomic cell is wrapped in several aluminum foil layers to stabilize the temperature and provide better heating efficiency. Finally, the wrapped atomic cell is placed in the copper cylinder

other parameters (Rb cell temperature, laser detuning, optical power) are the same. However, it noted that the vapor cell could not provide a strong enough nonlinear effect if it is too short. On the other hand, if the vapor cell is too long, a part of the light will be absorbed by the rubidium atoms. Therefore, choosing the right length of the atomic cell is one of the critical factors for good experimental results. Cells' diameters are typically 1 inch in our lab, but the shape of the cell can be customized to meet specific experimental requirements. The input and output windows of the cell are coated with Anti-Reflection (AR) matter, giving a transmission of approximately 98.3% on a single window. The vapor pressure of the cell is approximately 1.86×10^{-7} torr at room temperature. We need to heat the cell to increase the vapor density of the rubidium atoms. The Kapton heaters are attached to the Rb cell, and several layers of aluminum are wrapped around the cell with insulating Kapton tape. The thermistor forms a closed loop with the AC transformer to stabilize the cell at the temperature required for our experiments. The covered cell is placed in the copper cylinder to keep the temperature of the cell at a relevantly stable degree. And it has been demonstrated that this heating system is capable of stabilizing the cell temperature at $\pm 1^{\circ}C$ during the experiments. For our experiments, we need to heat the rubidium cell to about $150^{\circ}C$, where the vapor pressure is about 4×10^{-3} torr and the atomic density is $8.9 \times 10^{19}\ m^{-3}$.

The temperature record of the cell can be realized with the thermocouple. It offers an easy, convenient and fast way to estimate the rubidium vapor cell's temperature roughly. However, it is essential that an absolute temperature is needed to calculate several relevant parameters, such as the atomic density and atoms' average speed. We can fit the transmission spectrum with the theory to extract the temperature in this case.

Chapter 4

Short Bragg pulse spectroscopy for a paraxial fluids of light

We implement Bragg-like spectroscopy in a paraxial fluid of light by imprinting analogues of short Bragg pulses on the photon fluid using wavefront shaping with a spatial light modulator. We report a measurement of the static structure factor, $S(k)$, that characterizes the density-density correlations of the elementary excitations. And we find a quantitative agreement with the prediction of the Feynman relation revealing the presence of pair-correlated particles in the fluid indirectly. We also study the dynamics of small amplitude density modulations traveling onto the paraxial fluid of light. The results demonstrate that we improved the resolution over previous methods and obtained the dispersion relation, including a linear phononic regime for weakly interacting photons and low sound velocity. The result of this section has been published in: "Measurement of the static structure factor in a paraxial fluid of light using Bragg-like spectroscopy", Phys.Rev.Lett.127, 023401 (2021) [34].

This chapter is organized as follows. I first introduce the short Bragg pulse technique, which inspired our approach. Then I present the measurement of the Bogoliubov dispersion relation of photon fluid based on the integral group velocity. We describe numerically and experimentally the optical implementation of Bragg spectroscopy and present a measurement of the static structure factor in agreement with the Feynman relation for a homogeneous Bose gas [11]. Finally, we measure the dispersion relation and evaluate the maximum resolution of our technique. In addition, we show that our method allows for an improvement of the resolution for dispersion measurements.

4.1 Bragg pulse spectroscopy

An essential characterization tool for an atomic BEC is Bragg spectroscopy [70]. The original implementation was based on the two-photon Bragg scattering and allowed for accurate measurement of the momentum distribution. It has been reported that the measurement of the dispersion relation, which describes how each frequency component of wave packet evolves [71] and the dynamic structure factor, the Fourier transform of the density-density correlation, which is significantly important to describe the many-body system with this technique in atomic BEC [11].

Bragg spectroscopy in atomic BEC relies on counting the number of scattered atoms as a function of the frequency difference between two Bragg beams [72]. The basic principle is as follows, the two far-off-resonant laser beams used for the Bragg spectroscopy are detuned from each other by a frequency $\Delta\nu$ and have in-plane wavevectors $\mathbf{k_1}$ and $\mathbf{k_2}$. This will result in the recoil momentum $\hbar\mathbf{k_r} = \hbar(\mathbf{k_1} - \mathbf{k_2})$ and the diffracted atoms leave the trap. Measuring the number of the diffracted atoms, N_{diff}, as a function of $\Delta\nu$ gives the line integrated distribution parallel to $\mathbf{k_r}$.

A variant of this configuration [69] has been presented in Fig.4.1 and relies on short Bragg pulses at two symmetrically far detuned laser beam impinging the condensate with an angle of θ for a short time τ, as shown in the Fig. 4.1(a). It is possible that the condensate absorbs a photon from one of the beams and then emits a photon to another since the photon has a significant energy uncertainty $\hbar\delta\omega$. This process will create left-moving and right-moving phonons with energy $\hbar\omega_k$. And the wavenumber k of phonon relies on the relative angle θ between two far-detuned beams. The phonons with the same amplitude and frequency but moving in opposite directions give rise to the standing wave with a given wavenumber k. After the short Bragg pulse, the phonon freely propagates in the condensates. We can also see phase-contrast of standing waves at different periods from Fig.4.1(b), (c), (d). The density perturbation after time t is:

$$\delta n(t) = |\psi(t)|^2 - |\psi(0)|^2 \tag{4.1}$$

The author measured the spatial Fourier transform ρ_k of $\delta n(t)$, where the ρ_k can be written as: $\rho_k = (\frac{U\tau}{\hbar})NS_0(k)sin(\omega_k t)$. The U is the amplitude of the sinusoidal potential resulting from the interference between the two laser beams, and N is the number of the condensate. The asterisk in Fig.4.1(e) indicates the k value corresponding to the standing wave. They extracted the Bogoliubov relation from the zero-crossings (in time) of ρ_k as shown in Fig.4.1(g) and repeating the experiment for many values of k. The static structure factor $S_0(k)$ is extracted from the amplitude of the ρ_k by parabolic fit.

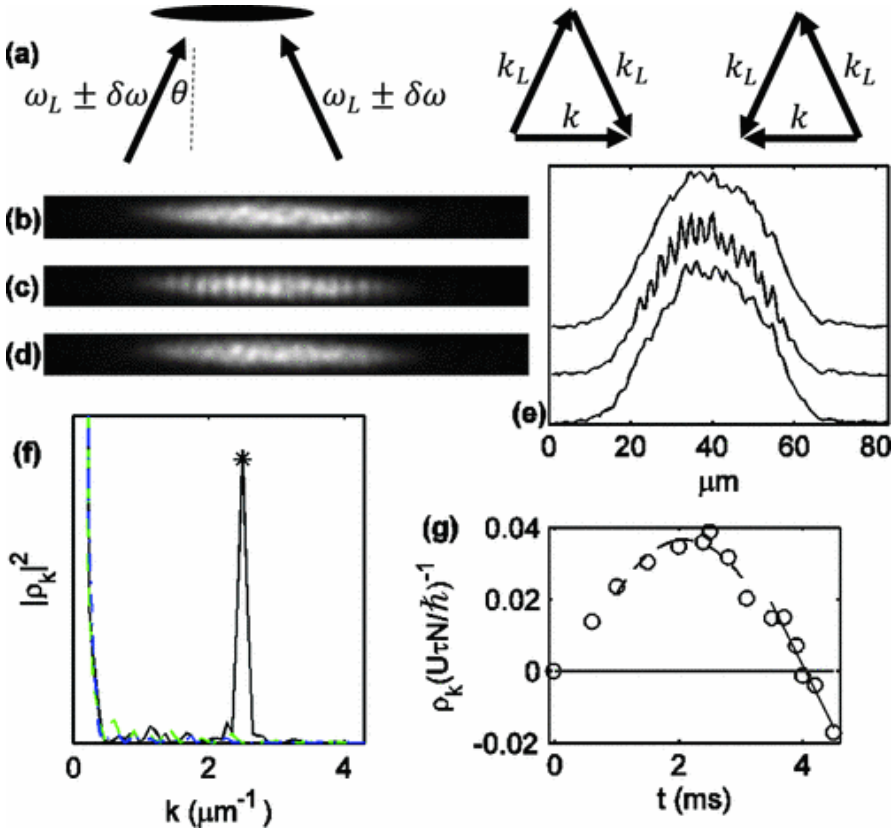

Figure 4.1: Figure extracted from [69]. Creating a phonon standing wave by short Bragg pulses. The larger condensate is shown. (a) Two far-detuned laser beams, with frequency ω_L and wave number k_L, impinge on the condensate. Absorption from the left (right) beam and emission into the right (left) beam results in the production of a right-moving (left-moving) phonon with wave number k. The combination of the left- and right-moving phonons results in a standing wave. (b)–(d) Phase-contrast images of the in situ condensate, for a short 22 μsec Bragg pulse with $k = 2.47\ \mu m^{-1}$, where (b) shows the time just before the pulse, (c) shows the first antinode of the standing wave, at 250 μsec and (d) shows the second node, at 510 μsec. (e) Integrated profiles of the images. The top, middle, and bottom curves correspond to (b), (c), and (d), respectively. The top and middle curves have been shifted vertically for clarity. (f) The magnitude squared of the Fourier transform of the profiles. The blue dash-dotted, black solid, and green dashed curves correspond before the pulse, the antinode, and the node, respectively. The asterisk indicates the k value corresponding to the standing wave. (g) The time dependence of the Fourier transform of the standing wave, for $k = 0.35\ \mu m^{-1}$. The linear fit at the zero crossing determines ω_k (solid line). The parabolic fit at the maximum determines $S_0(k)$ (dashed curve).

4.2 Measure the dispersion with the group velocity

Before we discuss the Bogoliubov dispersion relation measurement unitize the Bragg spectroscopy technique, we first review another important work that measures the excitations spectrum in a light fluid based on a group velocity measurement [36]. The experimental setup is shown in the figure.4.2. A polariton beam splitter (PBS) splits the light with a wavelength 780 nm coming from the Ti-Sapphire laser source into two paths. One is the pump beam (red line), and another is the probe beam (orange line). The stronger pump beam is tuned close to the atom resonance and spatially elongated along the y-axis using two cylindrical lenses and is sent into the rubidium atomic cell as our photon fluid. The lower power probe beam elongated along the x-axis creates a density perturbation with respect to the fluid at an angle θ. At the entrance of the medium, as the quench effect produces two wave packets with wavenumber $k_\perp = \pm k_{pr} sin(\theta)$, where the k_{pr} is the wavevector of the probe beam. The velocity of the two wave packets can be adjusted by the angle θ between the pump and probe beam. Two wave packets with the same velocity but in opposite directions propagate in a nonlinear medium. The group velocity v_g of the wave packets can be determined by measuring their distance at the end of the cell in the transverse plane. And the result shows that the wave packet distance of the two wavevectors is a constant when tuning the incidence angle θ within a certain range $k_\perp < k_\xi$, where ξ is the healing length and $k_\xi = 2\pi/\xi$. It means the velocity of the wave packet, namely, the speed of sound $c_s = c\sqrt{\Delta n}$ independent on the k_x in the transverse plane in this range. This interesting phenomenon tells us that when changing the angle θ between the probe beam and the pump beam within this range, the probe beam emerges at the same position at the end of the cell. Even if the $\theta = 0$, it still produces a pair of counter-propagating wave packets moving along the x-axis at c_s. This finding is different from the classical Snell's law, which describes the relationship between the incidence angle and the refractive angle when light passes through the boundary of two media. And this difference comes from the sound-like behavior of the Bogoliubov dispersion relation at low wave vectors. However, a different phenomenon will occur when beyond this value $k_\perp > k_\xi$, the distance of two wave packets starts to increase linearly with increasing wavenumber. The excitations behave as single particles along the x-axis in the transverse plane. So we can derive the group velocity according to the distance between two wave packets $D = 2Lv_g$ from the end of the cell, where L is the length of the rubidium cell. The dispersion relation can be obtained by integrating the group velocity over the momentum according to the definition of the group velocity $v_g = \dfrac{\partial\Omega}{\partial k_\perp}$. The dispersion relations measured by this method are in high agreement with the theoretical predictions of Bogoliubov dispersion described in chapter 2. As long as the $k_\perp \ll k_\xi$, the excitations behave as collective phonons and move at sound velocity c_s in the transverse plane. Reversely, $k_\perp \gg k_\xi$ the excitations behave as single particle propagating at v_g along the x-axis in the transverse plane.

However, in this experiment, the weak nonlinearity corresponds to the lower speed of sound, which will lead to the two wave packets propagating too slowly to separate very clearly, causing

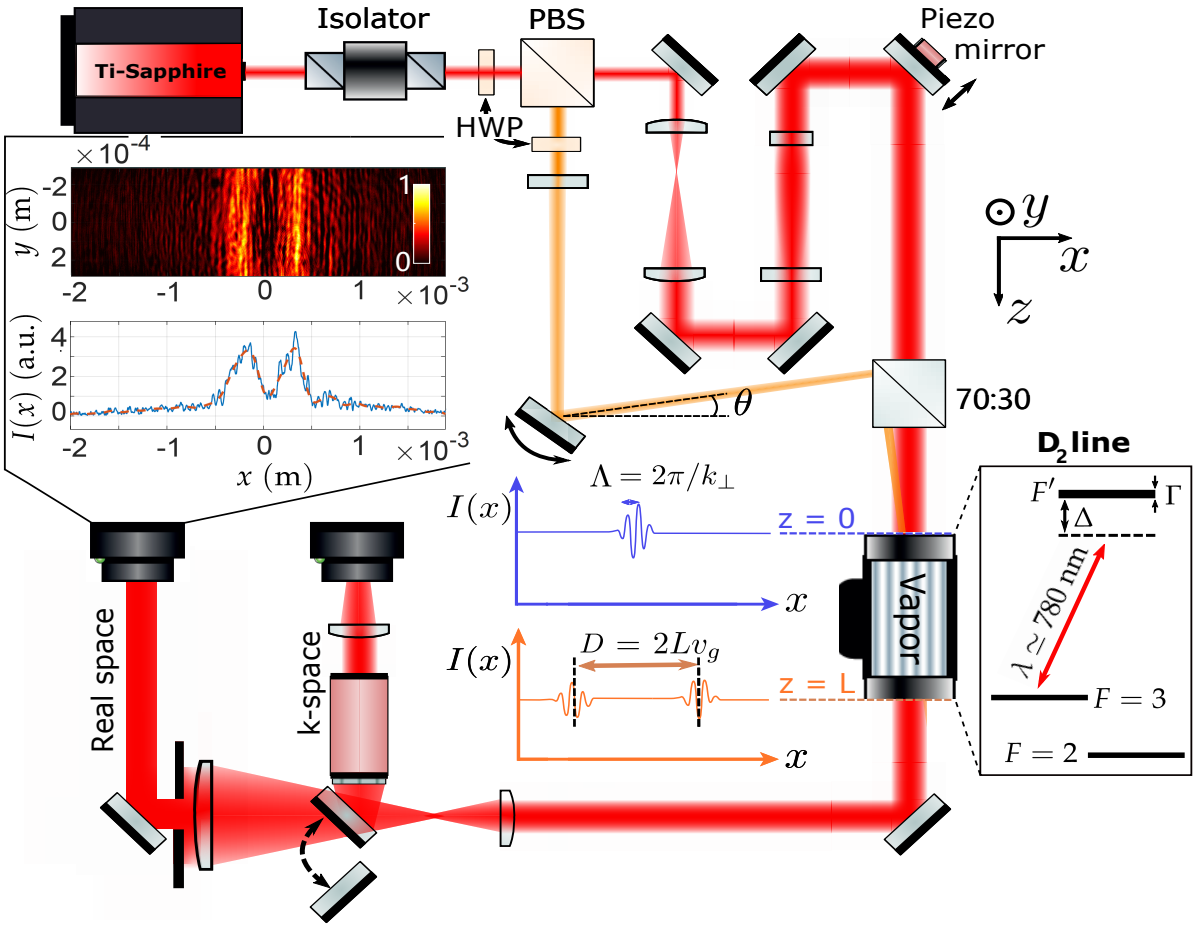

Figure 4.2: Experimental setup: polarized beam splitter (PBS) and half-wave plate (HWP). θ is the angle between the probe (orange beam) and the optical axis defined by the pump (red beam). The probe interferes with the pump and slightly modulates its intensity. (Blue inset) Integrated intensity profile at the input of the medium ($z = 0$). The wavelength Λ of the density modulation is given by $2\pi/k_{perp}$, where $k_\perp = k_0 sin(\theta)$. (Orange inset) Integrated intensity profile at the output of the medium ($z = L$). The distance D between the two wave packets gives access to the group velocity of the elementary excitations in the transverse plane. The output plane is imaged on a CMOS camera. (Inset, top left) Background-subtracted image obtained for $\theta \approx 0$ rad and associated integrated envelope profile (blue: original; red dotted: high frequency filtered).

difficulty in deriving the dispersion relation.

Analogy to the 4-wave mixing process

In reality, this experiment is a degenerate four-wave mixing process in which two pump photons are turned into a probe photon and a conjugate photon. However, in the fluid community, they are more commonly referred to as Bogoliubov excitation modes in a nonlinear medium propagating along $+k_x$ and $-k_x$, where k_x is the wave number in the transverse direction. It is worth noting that in the four-wave mixing process, if the probe beam and the pump beam overlap, the resultant conjugate light also overlap. However, two Bogoliubov modes were still formed in a language of the fluid community.

4.3 Bragg-like Spectroscopy in the paraxial the fluid of light

While the dispersion relation has been recently obtained by measuring the group velocity of two counter-propagating wave packets. A measurement of the static structure factor that characterizes the density-density correlations of the elementary excitations has not yet been reported for a fluid of light.

We want to implement an optical analogue of Bragg spectroscopy to measure the static structure factor in a paraxial fluid of light. We show that short Bragg pulses used for the phase imprinting technique in an atomic BEC [69] can be achieved in a photon fluid using wavefront shaping with a spatial light modulator.

In the atomic BEC experiment, the author creates the phase modulation by applying the sinusoidal potential in the condensate. To realize the production of counter-propagating phonons in the photon fluid, we imprint a phase modulation on the beam with a given wavelength and a given depth with a spatial light modulator (SLM) and image it on the input plane of the nonlinear medium. This is in fact a general strength of paraxial fluids of light, since any phase modulation (analogous to any short external potential) can be applied to the initial state of our system. It will give rise to two opposite direction phonons generation with wavevector $+k_x$ and $-k_x$ at the input plane. These two phonons with the same characteristics as in short Bragg pulse spectroscopy. Two counter-propagation phonons freely move in the nonlinear medium. Sometimes they are out of phase, and sometimes they are in phase.

On the other hand, instead of probing the intensity perturbation as a function of the time. We only have access to a fixed time ($t = nL/c$, where L is the length of the nonlinear medium), and study the intensity perturbation as a function of the k_x. The state at a fixed effective time corresponds to the end of the cell, which we can image onto a camera using a set of lenses.

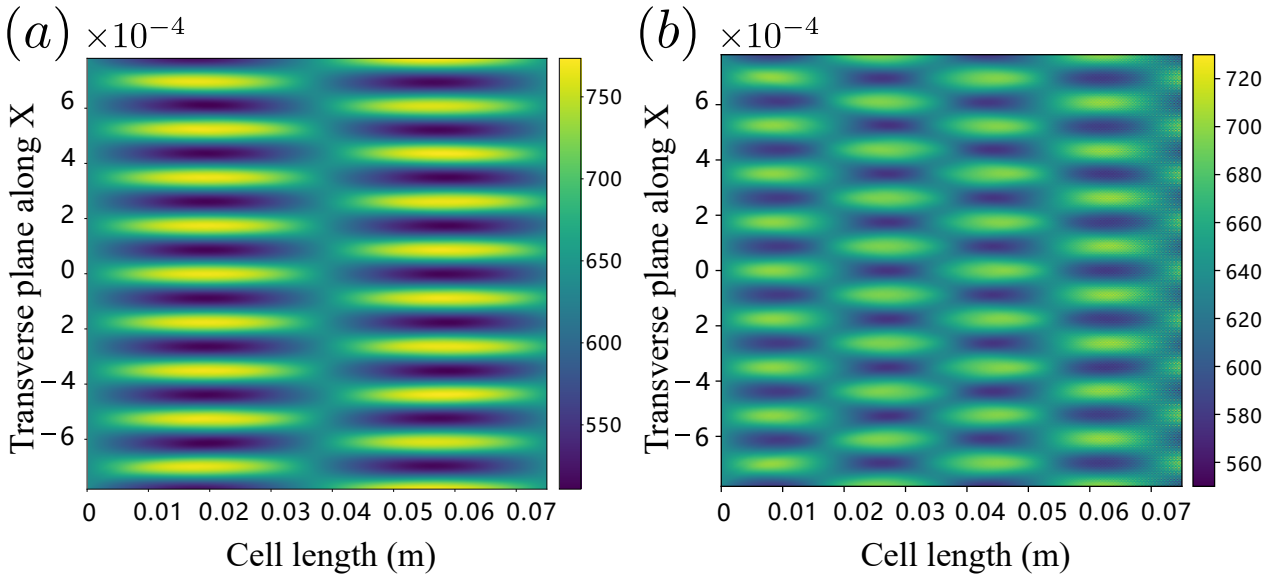

Figure 4.3: Simulated density modulation for the medium of 7.5 cm and a transverse wave vector of $k_x = 3.6 \times 10^4\ mm^{-1}$ and phase modulation parameter $\alpha = 0.1$, with different refractive index (a) $\Delta n = 0$ and (b) $\Delta n = 1.87 \times 10^{-5}$.

Using only a measurement at the fixed effective time, we show in the following that we can obtain the dispersion relation from the minima of δn, and the zero temperature static structure factor from the maxima of δn.

4.3.1 Numerical simulation

Before implementing the experiment, we begin with the numeric simulation. We have discussed in chapter 1 that the NLSE describes how an electric field close to the atom resonance propagates in the nonlinear medium. However, it is not enough to understand the electric field's state at a given position in the nonlinear medium. Thus, we must solve the NLSE. The splitting step Fourier method is commonly used to deal with the nonlinear problem.

When a laser field passes through the nonlinear medium, the electric field in the presence of the modulation can be expressed as:

$$E(x, z) = \mathcal{E}_0 e^{i(k_0 z + \alpha cos(k_x x))} \tag{4.2}$$

where the $\mathcal{E}_0$ is the amplitude of the electric field, k_0 is the wave vector, k_x is the wave number in the transverse direction and α gives the depth of the modulation.

The numerical simulation pattern of plane waves counter-propagating in the transverse plane with opposite wave vectors $+k_x$ and $-k_x$ and oscillating in z at the angular frequency $\Omega_B(k_x)$ as represented in Figs.4.3(a) and 4.3(b). Here we set the parameters as following: laser wavelength $\lambda = 780\ nm$, length of the rubidium cell $L = 7.5\ cm$, the intensity of the pump beam $I_{pump} = 2.0 \times 10^5\ W/m^2$ and wave vector $k_x = 3.6 \times 10^4\ m^{-1}$. Figure 4.3(a) presents the simulated pattern in the non-interacting case $\Delta n = 0$, which means a large detuning or a small fluid power. While Figure 4.3.(b) includes repulsive interactions and the nonlinear refractive index given by $\Delta n = 2 \times 10^{-5}$, corresponding to the near resonance or a large fluid power. In these two cases, we set the phase modulation depth $\alpha = 0.05$. Here, we surprisingly find that the interference fringes along the z period become smaller in the nonlinear case compared to the linear one. The reason causes this difference is that the free particle dispersion relationship starts to turn to the Bogoliubov dispersion. It is well demonstrated that when the strong laser beam close to resonance passes through a nonlinear medium, causing a change in the refractive index coefficient. Or we say that an effective interaction exists between photon and photon.

Next, we investigate the effect of the phase modulation parameter α on the result. All other stimulated parameters are same as Figure.4.3 except for the different modulator parameter for $\alpha = 0.01$, $\alpha = 0.05$, $\alpha = 0.1$ and $\alpha = 1$. The result is shown in figure.4.4. Note that the phase modulation parameter should be within a certain reasonable range. Strictly speaking, the phase modulation parameter α should be sufficiently small without changing the characteristics of the photon fluids. Otherwise, if the phase modulation parameter is too large, the interference diagram will be deformed, as in fig. 4.4(d).

However, the next problem we encounter is how to extract the information from the density pattern. In other words, how to connect the density pattern with the dispersion relation $\Omega(k_x)$ and the structure factor $S_0(k)$. As we have seen from the previous introduction, it is impossible to observe the time evolution in our paraxial fluid of light due to fact the fixed length of our atomic cell medium. We can only determine the density perturbation at a fixed time $\tau = L/c$, corresponding to the exit plane of the nonlinear medium. However, we can calculate the interference contrast as a function k_x at the exit plane of the nonlinear medium to extract the static structure factor $S(k_x)$ and the dispersion relation $\Omega_B(k_x)$. And the contrast at the end of the medium is defined as:

$$C = \frac{n_{max} - n_{min}}{n_{max} + n_{min}} \tag{4.3}$$

The structure factor is the spatial noise spectrum (normalized to 1 for a coherent state). It is defined by:

$$S(k_x) = \frac{\langle \rho_{k_x}^2 \rangle - \langle \rho_{k_x} \rangle^2}{N} \tag{4.4}$$

where ρ_{k_x} is the spatial Fourier transform of δn and N the total number of photons. The out plane of the vapor cell is imaged on the camera to study the fringe. The density perturbation is given by:

$$\delta n(z) = U S_0(k_x) cos(\mathrm{k} \cdot \mathrm{r}) sin(\Omega_B z) \tag{4.5}$$

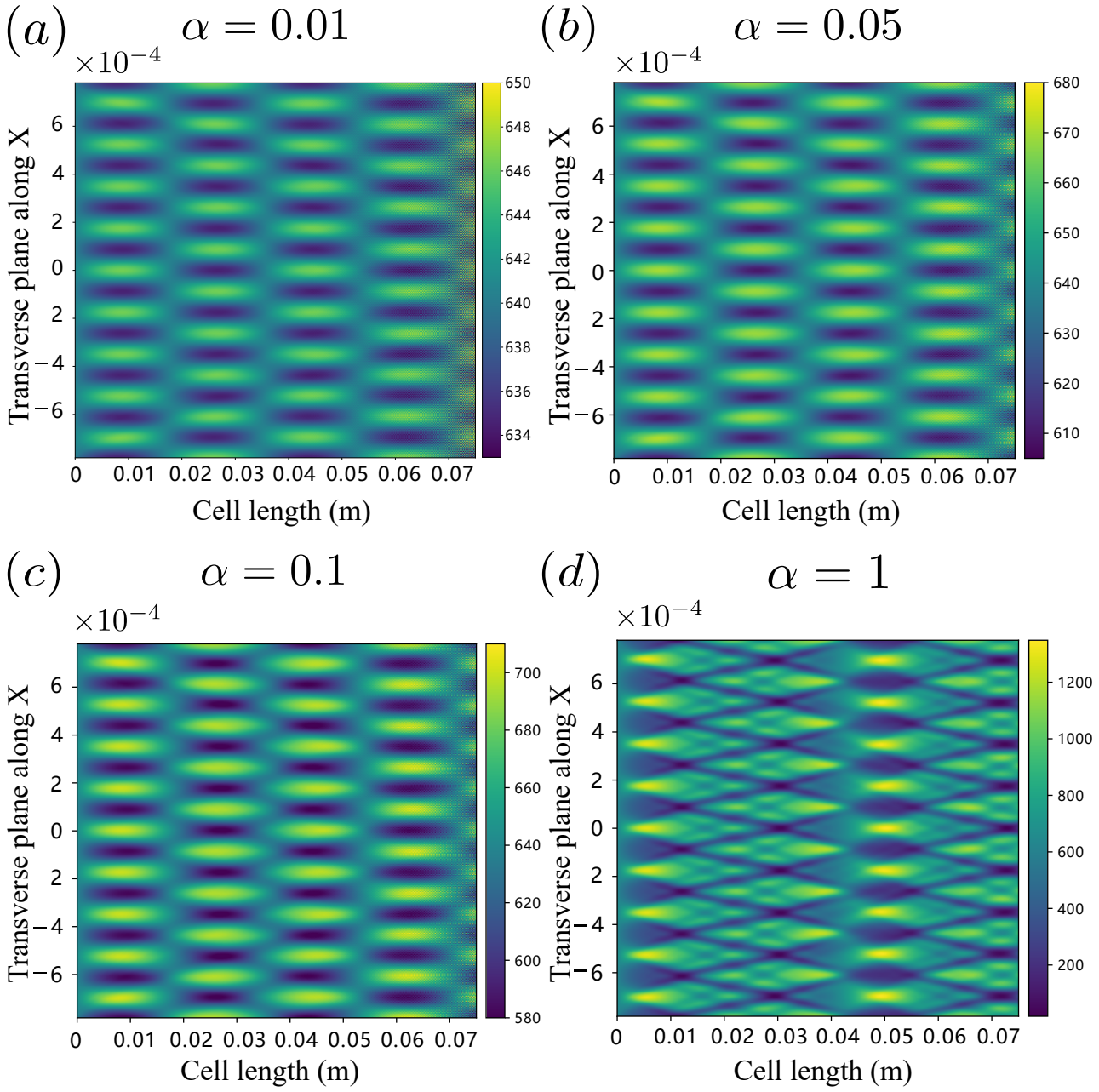

Figure 4.4: The simulated density modulation pattern for medium of 7.5 cm and a transverse wave vector of $k_x = 3.6 \times 10^4\ m^{-1}$ and $\Delta n = 1.87 \times 10^{-5}$ for different modulation parameter (a) $\alpha = 0.01$, (b) $\alpha = 0.05$ (c) $\alpha = 0.1$ and (d) $\alpha = 1$.

Using the definition of the contrast C in the transverse plane given above, we obtain the following:

$$C(k_x) = |US_0(k)sin(\Omega_B z)| \tag{4.6}$$

In Eq. 4.6, it is clear that we can isolate $US_0(k_x)$ using the maximum contrast values. To further remove the U dependence, we measure $US_0(k_x)$ for the non-interacting case. In this regime, it is known that $S_0(k_x)$ is equal to 1 at all k_x since the beam here is a spatially coherent state [6] and therefore U is equal to the contrast maxima. Then we can also obtain the dispersion from the minima of contrast. We determine the k_x from the contrast minimum value. At this moment, the dispersion relation Ω_B should meet the condition:

$$\Omega_B(k_x)L = p\pi \tag{4.7}$$

This equation has a profound and essential physics point. It means that we can plot the dispersion relation by reporting the k_x positions of the contrast minima and assigning them a frequency $p\pi/L$, where $p = 1,\ 2,\ 3$ .... Specifically, we can know the dispersion relation $\Omega_{B1} = \pi/L$ for corresponding to the first minimum k_{x1}. And for the second contrast minimum, the dispersion relation $\Omega_{B2} = 2\pi/L$ for corresponding k_{x2} and so on. With this method, we can get a set of the value of k_x and the Ω_B, so that we can plot the Ω_B as a function of the k_x and then compare with the theory.

For a fixed depth phase modulation $\phi = 0.1cos(k_x x)$ with a given wave vector value k_x, we can calculate the contrast at the end of the medium at this k_x. So we can plot the contrast as a function of k_x. According to the formula Eq.4.6, we can extract the dispersion relation from the minimum value of the contrast and the static structure factor from the maximum contrast value. From this set of k_x and Ω_B values, we are able to plot the dispersion relation in Fig.4.5 and find it has a good agreement with the theory. The orange 'x' label the minimum of the contrast at the end of the cell, and the orange dots stand for the data points we extracted from the minimum of the contrast. The blue curve is the theoretical Bogoliubov dispersion curve. From this figure, we can get when $k_x\xi < 1$, the dispersion relation increase linearly with the $k_x\xi < 1$, which predicts the phonon regime. While $k_x\xi > 1$. the dispersion relation becomes parabolic. We also extract the maximum value from the contrast and plot the structure factor $S_0(k_x)$ as a function of the $k_x\xi$. In the figure.4.6, the blue dots are the maximum points extracted from the contrast, the orange curve is plotted according to the Feynmann relation. We can see they are highly in agreement with each other. We found that the static structure factor is significantly reduced at long wavelengths compared to free particles, revealing the presence of nontrivial pair correlations indirectly in a paraxial fluid of light [71].

4.3.2 Experimental configuration and result

Our experimental setup is shown in the figure.4.7. A 780 nm quasi-parallel Gaussian beam coming from a tunable diode laser Toptica DL Pro laser source is elongated along the x-axis

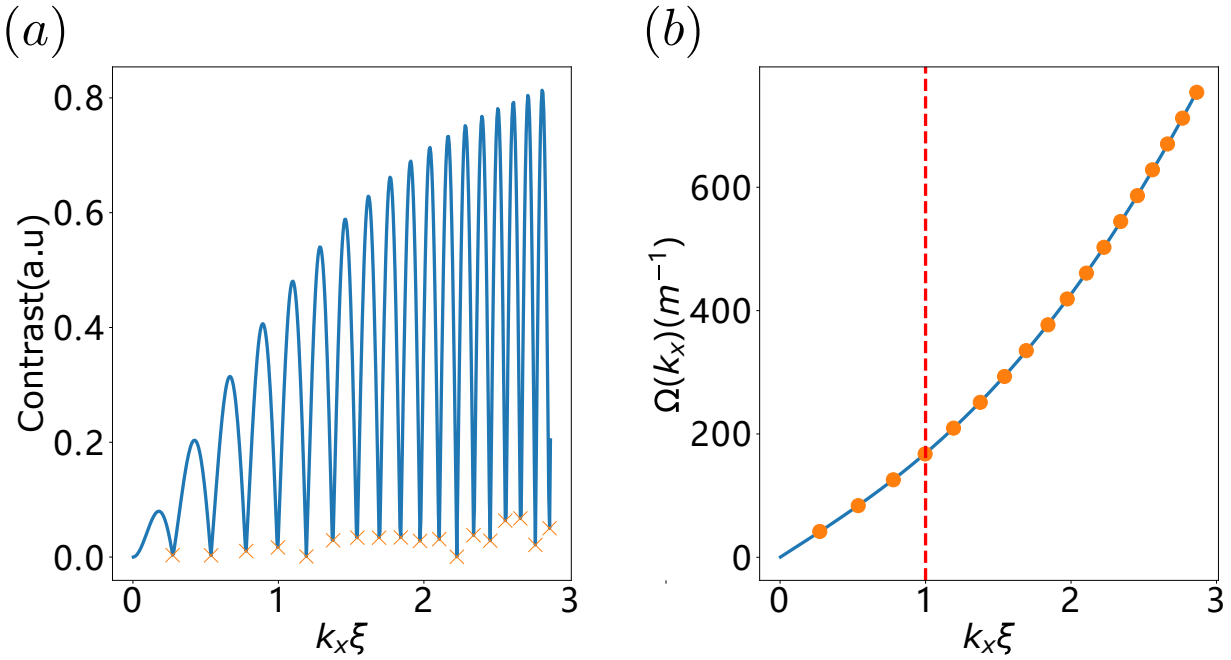

Figure 4.5: Numerically calculate the contrast at the end of the medium as the function of the product of wave vector k_x in the transverse plane times the healing length ξ. The orange 'x' label the minimum contrast. According to these dots, we plot the dispersion relation Ω_B as a function of the wave vector k_x in the transverse plane times the healing length ξ. The red vertical line represents the $k_x\xi = 1$. The numerical simulation shows that the dispersion is linear when $k_x\xi < 1$. However, when $k_x\xi > 1$, the dispersion relation behaves as parabolic. Parameters: $\lambda = 780\ nm$, $\Delta n = 1.875 \times 10^{-5}$, $T = 142°C$, $\xi = 2.87 \times 10^{-5}\ m^{-1}$.

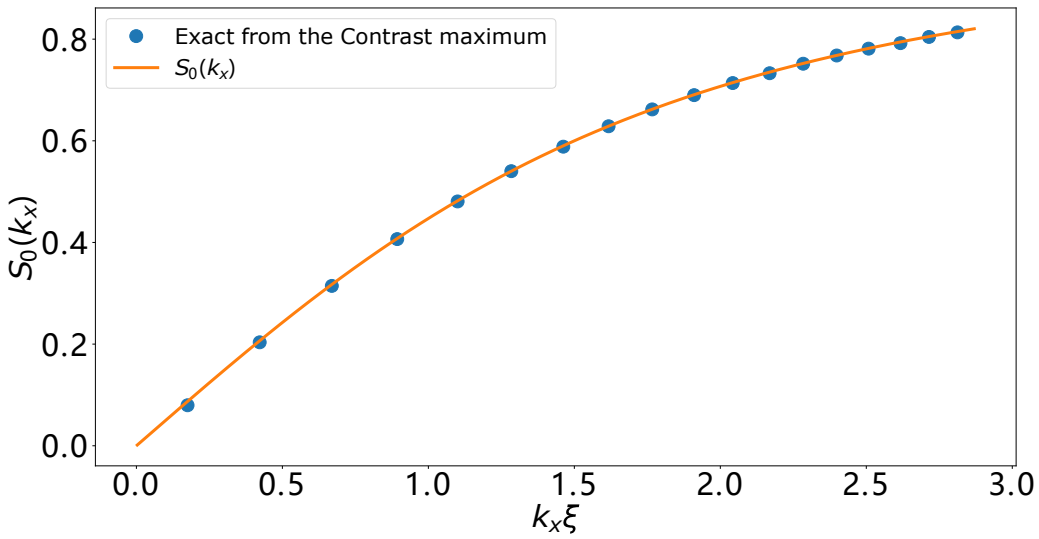

Figure 4.6: The blue dots are extracted from the maximum contrast at the medium's output plane. The orange curve is plotted according to the relation.

with a pair of cylindrical lenses. We can finely adjust the frequency detuning Δ with respect to the $F = 2$ to $F' = 2$ D_2 line of ^{87}Rb. The beam was then sent to the spatial light modulator (SLM), and the beam's length could cover the spatial light modulator screen. The spatial light modulator modulated the phase of the input light via imprinting a sinusoidal phase of wave vector k_x. It noted that in our case, we limited the modulation depth to 0.1 to remain within the Bogoliubov perturbative approximation so that intensity modulation does not locally modify the nonlinear index Δn. For a given k_x, the phase applied on the SLM is $\phi(x) = 0.1cos(k_x x)$, which leads to the generation of phonons with opposite propagation directions with wavevector $+k_x$ and $-k_x$. And the wave vector can be changed by a phase hologram loaded on the spatial light modulator. Since the spatial light modulator is likely to reflect part of the light, we use a filter in the Fourier plane to keep only the modulated first-order beam. Then we use a polarization beam splitter (PBS) to split the light into two paths, one of which is imaged on the camera to observe the situation in momentum space. The other path is directed to the entrance of the 6.8 cm Rubidium vapor cell with a demagnification factor of three to increase its resolution. The Rubidium vapor cell is filled with a natural mixture of 28% of ^{85}Rb and 72% of ^{87}Rb, and the beam waists at the entrance are $\omega_x = 0.15$ mm and $\omega_y = 1.5$ mm. The two phonons propagate in the transverse plane with wavevector $\pm k_x$ and fringes along the z-direction with Bogoliubov frequency Ω_B. After the rubidium cell, a camera mounted on a translation stage is used to record the interferogram at the exit of the medium. Since we can only access the images at effective fixed times $t = 0$ and $t = n_0 L/c$ for the states corresponding to the input plane ($z = 0$) and the output plane ($z = L$) of the medium. In the experiment, a translation stage can easily be manipulated to get the density image at the entrance and end of the medium.

We probe the density perturbation as a function of the wavevector k_x of the phase modulation at a fixed time instead of studying it as a function of time. At the entrance of the medium, two counter-propagating phonons are destructive interference independent of the value of k_x. At the cell's exit, they may be in phase or out of phase, determined by the initial k_x, which can be varied by the phase diagram on the SLM. Figure 4.8 is the experimental image of the density collected by the camera for the different wave numbers k_x. The figure.4.8 (a) shows the minimum contrast when the wave vector $k_x = 27.8$ mm^{-1} at the transverse plane and maximum contrast when the wave vector $k_x = 43.2$ mm^{-1} at the transverse plane in the non-interacting case. Note that these images are taken with a large modulation depth for illustration. This non-interacting case is obtained experimentally by setting a large detuning ($\Delta = -6$ GHz) from the ^{87}Rb $F = 2$ to $F' = 2$ transition.

We then took 475 images of the cell output with modulations ranging from $k_x = 5$ mm^{-1} to $k_x = 100$ mm^{-1} with a step $dkx = 0.2$ mm^{-1}. To measure the density modulation δn, we normalize the images by a reference taken without phase modulation and then select a central window of the fluid. After integrating the intensity along the y (vertical) axis, we calculate the contrast directly proportional to $\delta n(\tau = L/c)$.

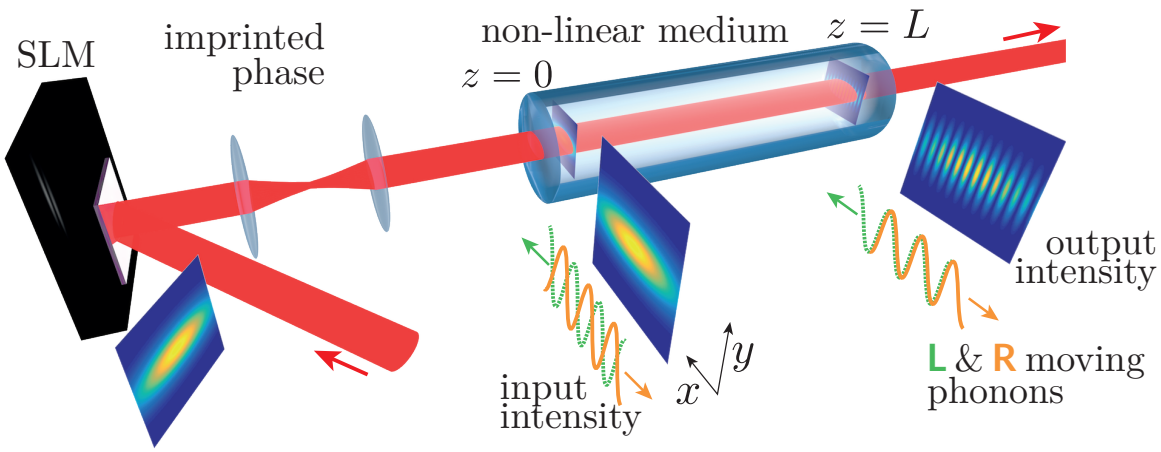

Figure 4.7: Principle of the experiment and simplified experimental setup. A 780 nm laser beam is elongated in the x direction with a pair of the cylinder lens and impinges on a spatial light modulator (SLM displays a vertical grating, which imprints a sinusoidal phase modulation of wave vector k_x. The SLM plane is imaged at the input of the 6.7 cm rubidium vapor cell. This phase modulation creates two counter-propagating left (L) and right (R) phonons at $+k_x$ and $-k_x$ represented in green and orange. Initially, in phase opposition (constant input density), the phonons constructively interfere after some effective time $\tau = z/c$, giving a maximum density contrast. The output plane of the nonlinear medium (a rubidium vapor cell) is imaged on a camera to study the fringe contrast at $z = L$.

To obtain the dispersion relation, we use the contrast measured as a function of k_x and record the successive minimum locations in k_x shown in Fig 4.9(a). The grey curve corresponds to a non-interacting case via setting the frequency far away from the resonance ($\Delta = -6$ GHz). While the red curves determine the interacting case with an input power $P = 90\ mW$, cell temperature $T = 128°C$ with $\Delta = -1.5$ GHz. Since we have created two counter-propagating excitations in the fluid by imposing a phase modulation, minima occur when $\omega(k_x) = p(\pi/L)$, where p is an integer. In Fig.4.9(b), we plot the dispersion relation for the different detuning by reporting the k_x positions of the contrast minima from Fig.4.9(a) and assigning them a frequency $p\pi = L$. We compare it to the parabolic dispersion (in black) obtained with the same method in the non-interacting case by setting the fluid laser far-off resonance. For the non-interacting case, we obtain the fit parameter $\Delta n = 0$. While for the interacting cases, in which we tune the detuning $\Delta = -2.5$ GHz (green curve), $\Delta = -2.0$ GHz (yellow curve) and the $\Delta = -1.5$ GHz (red curve), the fit nonlinear refractive indexes give $\Delta n = 0.5 \times 10^{-5}$, $\Delta n = 0.7 \times 10^{-5}$ and $\Delta n = 1.0 \times 10^{-5}$, respectively. From Fig.4.9(b), we can see that the contrast minima towards a smaller k_x characterize the interaction between the photons. The contrast minima corresponding to k_x moves to a point substantially further away compared to the weak interaction case.

We carry out the same experiment but with different experiment parameters: input power is 90 mW and the cell temperature $T = 106°C$ in the nonlinear case, as shown in the Fig.4.10(a).

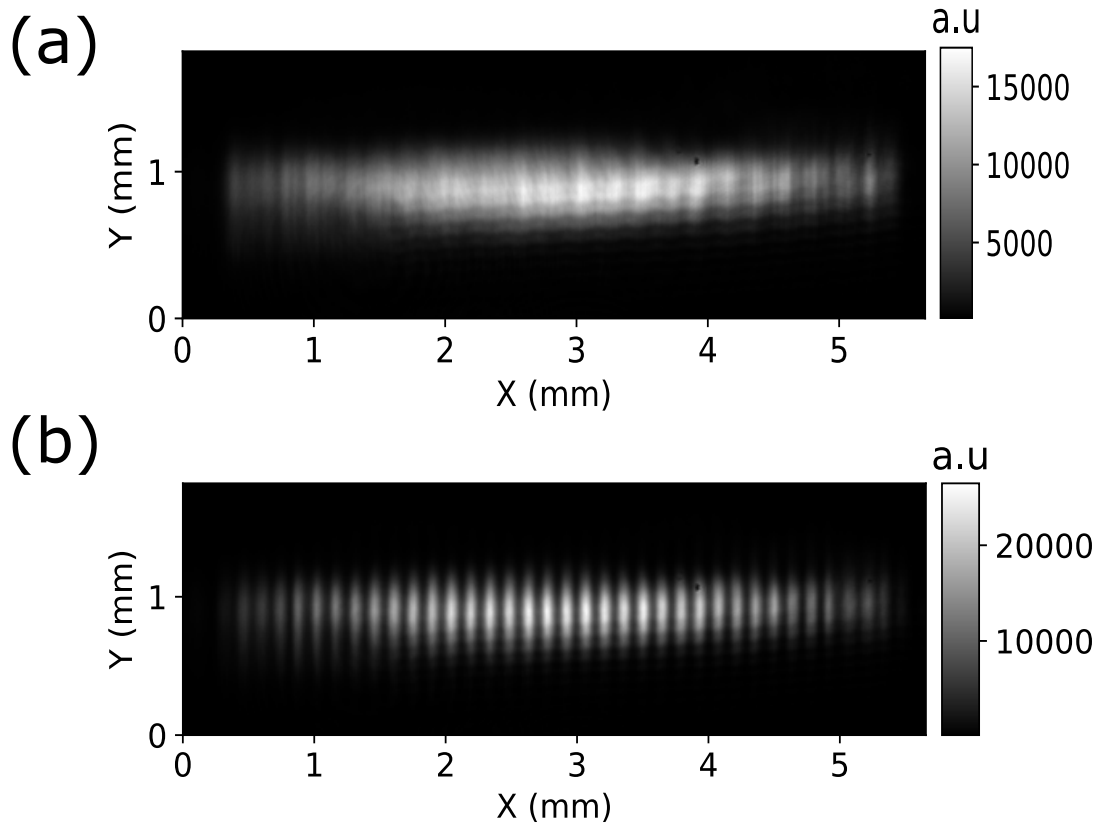

Figure 4.8: Experimental images of the density obtained respectively for $k_x = 27.8\ mm^{-1}$ (minimum of contrast) and $k_x = 43.2\ mm^{-1}$ (maximum of contrast) in the non-interacting case ($\Delta n = 0$). These images are taken with a large modulation depth for illustration.

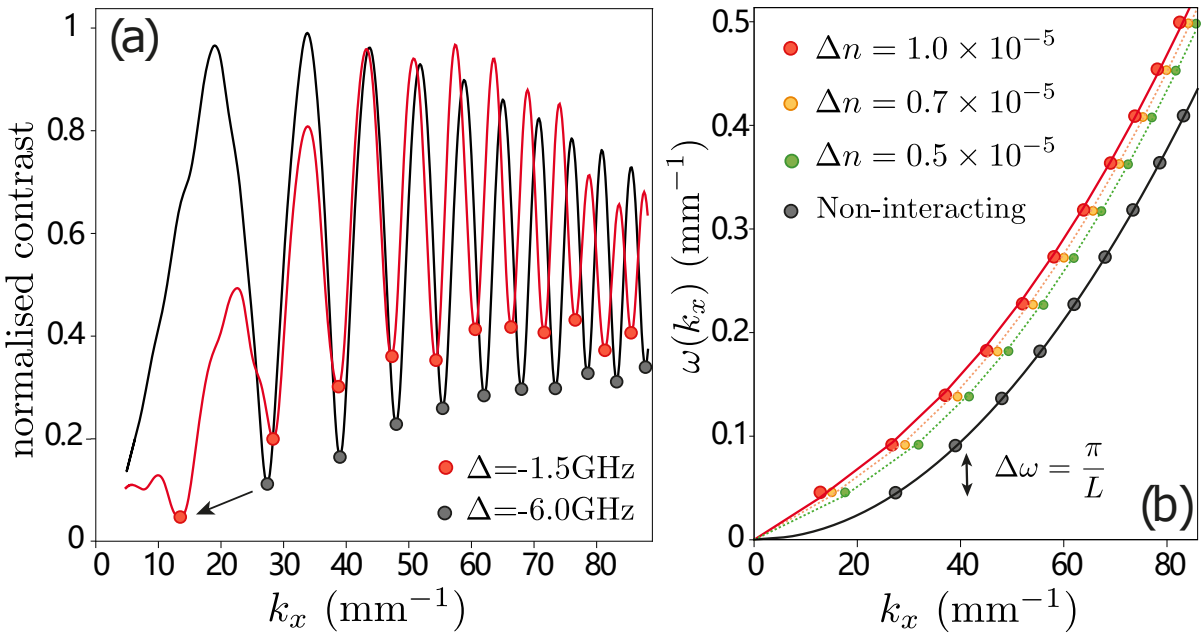

Figure 4.9: (a) Contrast results (smoothed and normalized) for the reference far-off resonance case (grey) with $\Delta n = 0$ and a close-to-resonance set (red) with an input power of 90 mW, a cell temperature of 128°C and an absorption of 50%. The shift of the minima of contrast toward the smaller k_x for the $\Delta = -1.5$ GHz set, shown by the grey arrow, is evidence of the nonlinear effect taking place. (b) Dispersion $\Omega(k_x)$ extracted from the minima of contrast of the reference far-off-resonance set, and for three data sets with decreasing detunings $\Delta = -2.5$ GHz (green curve), $\Delta = -2$ GHz (yellow curve) and $\Delta = -1.5$ GHz (red curve) with a laser power increased to 105 mW. The dots show the extracted experimental values $\Omega(k_x) = p\pi/L$ for the p-th minimum and the full lines the fits of the Bogolioubov dispersion. The resulting values of Δn are indicated in the legend.

We extract the structure factor from this contrast measurement using the methodology described previously. We first calibrate the phase imprinting efficiency of the SLM, the modulation transfer function of the optical system, and the depth of phase modulation experimentally by measuring the response function U for the non-interacting case. Since U is not modified while changing Δn, the structure factor for the interacting case is obtained by dividing the contrast maxima values for $\Delta n \neq 0$ by this calibrated value of U to obtain a normalization to 1 at large k_x. Experimentally, it corresponds to the ratio between the red and black maxima for the same p in Fig.4.10(a). The results are presented in Fig.4.10(a) for a weakly interacting fluid ($\Delta = -1.5$ GHz) and non-interacting case ($\Delta = -6$ GHz). The structure factor is a normalized, unitless quantity, that characterizes the spatial density-density correlations.

To complement our measurement of the structure factor, we provide a quantitative comparison with the Feynman relation [11]:

$$S(k_x) = \frac{k_x^2/2k_0)}{\Omega_B(k_x)} \tag{4.8}$$

The Feynman relationship predicts the excitation spectrum and structure factor of the condensates in the phonon regime drops to zero when the external interaction is neglected. It provides a fundamental understanding of the collective response for the ultra-cold gas in the small phonon regime without the spin.

Figure 4.10(b) clearly shows that $S(k_x)$ is highly reduced at low k_x (long wavelength). This can be explained by the creation of correlated pairs at $+k_x$ and $-k_x$ which minimize the total energy of the system, known as quantum depletion [71].The solid red line shown in Fig.4.10(b) presents this relation with no adjustable parameters.

We also extract the dispersion relation in these experimental parameters, shown in inset of Fig.4.10(b). The dots are the experimental points, and the full lines are fitted to the Bogoliubov relation. For the noninteracting case, we obtain the fit parameter $\Delta n = 0$ with an uncertainty of 2×10^{-7}. This value agrees, within the resolution of our experiment, with the expected quadratic dispersion $\omega_{lin} = k_x^2/2k_0$ in the absence of interaction. For the interacting case, the fit of the Bogoliubov dispersion relation gives a value $\Delta n = 4.6 \times 10^{-6} \pm 3 \times 10^{-7}$. This is the value we used to plot the Feynman relation in order to compare it with our data without extra adjustable parameters in Fig.4.10. Using the relation $c_s = c\sqrt{\Delta n}$, we can extract the sound velocity c_s from these fits, and we obtain $c_s = 2.1 \times 10^{-3} c$.

Finally, we evaluate the sensitivity of this method for resolving weak interaction (small Δn). The energy offset accumulated in the linear part of the dispersion translates into an energy shift at large k_x. The dispersion curve with $\Delta n \neq 0$ is vertically shifted relative to the non-interacting

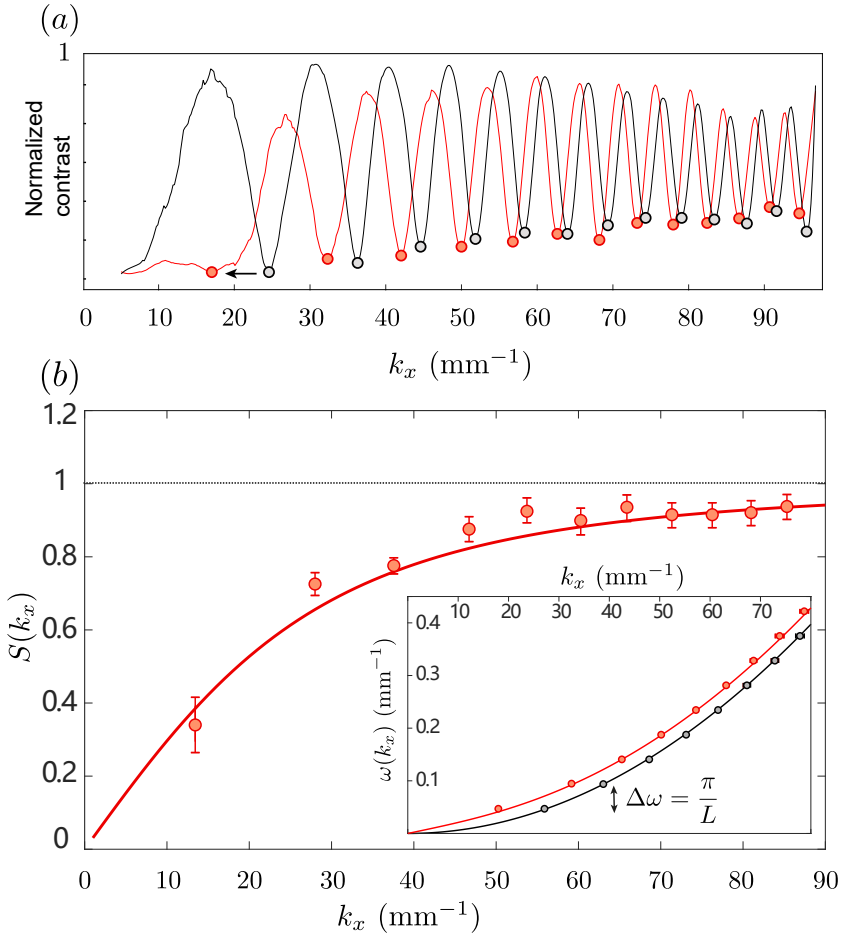

Figure 4.10: Static structure factor measurement for close-to-resonance set with an input power of 90 mW, a cell temperature of 106°C, and an absorption of 40%. The dashed line at $S_0(k) = 1$ is the structure factor of a noninteracting gas (coherent state). The solid red line is the Feynman model given by Eq. (7) with the parameter $\Delta n = 4.6 \times 10^{-6}$.

one ($\Delta n = 0$). We calculate this shift at large k_x as:

$$\Omega_B(k_x) - \omega_{lin}(k_x) = \sqrt{k_x^2|\Delta n| + \left(\frac{k_x^2}{2k_0}\right)^2} - \frac{k_x^2}{2k_0} \approx k_0 \Delta n \tag{4.9}$$

The value of Δn is then directly obtained by the difference with the noninteracting reference at high k_x. Knowing the uncertainty on k_x to be $dkx = 0.2\ mm^{-1}$, it is possible to estimate the smallest nonlinear index value achievable with this technique to be $\Delta n = 2 \times 10^{-7}$($c_s = 0.45 \times 10^{-3}c$). This is more than an order of magnitude better than previous techniques using a group velocity measurement we introduced earlier.

4.4 Conclusion

In this work, we have implemented Bragg spectroscopy in a paraxial fluid of light. This technique has proved to be an essential tool for studying ultracold atomic BEC and was missing in the fluid of light platforms. The optical analogue of the Bragg spectroscopy technique allows us to measure the dispersion relation with a better resolution at a low speed of sound. We show that our implementation is robust and highly sensitive since it allows us to measure the interactions an order of magnitude weaker than previously reported. Importantly, we present a measurement of the zero temperature static structure factor, which could be translated to the excitation strength of the phonons. It shows a good agreement with the Feynman relation because we find a significant reduction compared to free particles. This measurement of the structure factor reveals the presence of pair-correlated particles in a paraxial fluid of light. These results open the way to measuring Tan's contact and observing beyond mean field effects in photon fluids.

Chapter 5

Oscillating spectrum of a quenched quantum fluid of light

According to the quantum field theory, pairs of particles can be generated from the quantum vacuum when system parameter changes. This chapter introduces the oscillating spectrum of a quenched quantum fluid of light by sending a near-resonant laser pulse propagating in a warm atomic vapor cell. When photons propagating cross at the front and back faces of the nonlinear medium in this relatively simple setup, they encounter a pair of abrupt jumps in the interaction parameter. The fluid of light is stimulated as a result of these two quantum quenches. The fundamental excitation mechanism in the weak-nonlinearity regime is the emission of pairs of correlated counter-propagating Bogoliubov phonons, which results in unusual characteristics in the intensity distribution and the near- and far-field two-body correlation functions. We calculate the static structure factor and observe an acoustic peak in the density power spectrum, known as Sakharov oscillating, which is usually discussed in cosmic microwave background (CMB) radiation. This interesting analogy can then be drawn toward the analogue of cosmological particle creation. The result of this section has been published in: "Analogue cosmological particle creation in an ultracold quantum fluid of light", Nat. Comm, 13(1):1-7 (2022) [30].

5.1 Background

One of the most remarkable predictions of modern quantum theory is that the vacuum of space is not empty. In fact, we often consider the quantum vacuum as containing ubiquitous fluctuations, as implied by the Heisenberg uncertainty principle. Although the virtual particles (that make up the quantum vacuum) whose observable effects are not visible directly, it is an outstanding prediction of quantum field theory that the vacuum can generate pairs of real particles when boundary conditions are suddenly changed. For example, the quantum vacuum fluctuation (propagating in the cosmic fluid as acoustic pressure wave) due to the rapid expansion of the very early Universe can tear these fluctuations apart and, thereby, turn them into pairs of real particles [73, 74]. This is responsible for the generation of the seeds for cosmic structure formation and further explains why we can see a colorful world today [75]. However, the rate of expansion of our Universe is too slow to create a measurable amount of particles in the cosmic microwave background radiation (CMB) at present. What is exciting is that the field theory neglects the microscopic details. And the frequencies of particle modes evolving over time [76], so we can apply the Bogoliubov transformation to connect the mode states at earlier and later times [77]. As a result, it is possible to create analogue cosmological particles via various quantum fluids in the laboratory.

In fact, analogue cosmological particle creation is a type of dynamical Casimir Effect (DCE), which is defined as the generation of pairs of real particles or photons from the vacuum as a result of a non-adiabatic change of a system parameter or boundary condition. It has been reported that a periodically oscillating mirror could convert virtual photons into directly observable pairs of real photons (Pair particles will be generated at frequency $\Omega/2$ for a sinusoidal modulation at frequency Ω) [78, 79]. This kind of pair generation is due to a mechanical movement of mirrors, named "mechanical" DCE. An analogue effect can be achieved by simply modulating one of the system parameters by changing the boundary conditions, labeled "parametric" DCE. It has been suggested that a periodic change of an optical cavity either filled with or constituted by a medium of refractive index n is equivalent to a periodic change of the boundary conditions.

The change in the interaction strength in atomic superfluid is analogous to an optical index change. A key experimental observation was that the quench excites acoustic waves, which interfere in both the spatial and temporal domains, leading to Sakharov oscillations. The quench in this context does not indicate the rapid cooling of the metal from the high temperature at which it is formed in the heating process to increase its hardness and mechanical strength. It should be noted that quench refers to how the quantum fluid responds when subjected to an abrupt environmental change. The Sakharov oscillations are usually discussed in the context of universe evolution and the anisotropy of the cosmic microwave background. Notably, the oscillations are unaffected by the microscopic specifics of the medium and have been observed by quenching the sample and monitoring the subsequent density fluctuations at different time and length scales in an atomic superfluid [45]. Sakharov oscillations are identified as the multi-

peak structure in the atomic density power spectrum, resembling that of the cosmic microwave background (CMB). So this oscillating offers indispensable information for inferring the composition of the universe and its evolution.

We want to use the quantum fluid of light to simulate the expansion process of the universe. In particular, we report on the spontaneous production of analogous cosmic particles via the quantum fluid of light in laboratory circumstances. Compared to the cosmological particle creation in the early universe, the radiation pressure in the cosmic fluid can be considered as the interactions between the photons. To generate the sound in the quantum fluid of light, we send a near-resonant pulse laser into a Rubidium vapor cell so generating two-photon interaction quenches at the front and the back faces. The interaction between photons is zero when a laser beam is near the atomic resonance in the vacuum because the coupling cross-section is too small to be insignificant. However, as the beam enters the nonlinear medium's front face, the situation changes because the interaction begins to play a role as a result of the nonlinear medium's $\chi^{(3)}$ Kerr nonlinearity. This is the first quench in which the photon interaction abruptly changes from zero to nonzero. At the back face of the Rubidium vapor cell, the photon interaction drops to zero and experiences the second quench. The emission of correlated-phonon pairs in the fluid of light due to the quantum quench of the photon-photon interaction constant can also be detected in momentum space by taking a far-field and spectrally resolved picture of the light emerging from the back face of the nonlinear medium.

5.2 Theoretical considerations

We want to investigate analogous cosmological particles by calculating the static structure factor so that a comparison with the cosmic microwave background power spectrum. To extract the dynamics of phonons and search for Sakharov oscillations, we calculate the structure factor of the quenched superfluids. The structure factor $S(k,t)$. which measures the power spectrum of spatial density fluctuations, is analogous to the angular power spectrum used in analyzing the CMB radiation. The static structure factor $S(k)$ is defined as the ratio of the spatial Fourier transform of the density fluctuation to the total number of particles, which can be expressed as a mathematical formulation:

$$S(k_x, k_y, k_z') = \frac{\langle |\delta\rho(k_x, k_y, k_z')|^2 \rangle}{N} \tag{5.1}$$

where $\delta\rho(k_x, k_y, k_z')$ is the spatial Fourier transform of the density fluctuation $\delta n(k_x, k_y, k_z')$ at time τ, and N is the number of total photons. According to this definition, it is clear that $S(k) = 1$ at zero temperature for non-interacting gas, reflecting the presence of spatial shot noise (quantum fluctuations) and the absence of correlations between the opposite modes.

The operator $\hat{b}_k^\dagger$ corresponds to the creation of a quasiparticle after the quench, in mode $\mathbf{k} = (k_x, k_y, k_z')$ oscillating at frequency ω_k. In the presence of quasiparticle populations

$N \equiv \langle \hat{b}_k^\dagger \hat{b}_k \rangle$ and correlations $C \equiv \langle \hat{b}_k \hat{b}_{-k} \rangle$, the mean occupation numbers N are real and positive, while C is in general a complex number. The static structure factor within the Bogoliubov approximation is given by:

$$S(k) = 1 + 2N + 2Re(Ce^{-i2\omega_k \tau}) \tag{5.2}$$

The populations and correlations are given by

$$N = \beta^2 + N_0(\alpha^2 + \beta^2) + 2\alpha\beta Re(C_0) \tag{5.3}$$

$$C = \alpha\beta + C_0\alpha^2 + C_0^*\beta^2 + 2\alpha\beta N_0 \tag{5.4}$$

Where $N_0 \equiv \langle \hat{a}_k^\dagger \hat{a}_k \rangle$ and $C_0 \equiv \langle \hat{a}_k \hat{a}_{-k} \rangle$ are the populations and correlations before the quench, and the operators are related by the Bogoliubov transform $\hat{b}_k = \alpha \hat{a}_k + \beta \hat{a}_{-k}^\dagger$. Since our series of two quenches, Eqs. (5.3) and (5.4) are applied twice. Because each quench either starts or ends with no interactions. α and β are the same Bogoliubov coefficients which diagonalize the Hamiltonian of a weakly-interacting quantum fluid. In the absence of quasiparticles before a given quench, the pair production is spontaneous, and Eqs. (5.3) and (5.4) becomes $N = \beta^2$ and $C = \alpha\beta$.

5.3 Experimental Setup and result

We send a 100 ns laser pulse with 100 mW power and 4 mm Gaussian waist into a rubidium 85 vapor cell heated to 150°C via the resistance covered the cell. The laser is detuned -1.5 GHz from $5S_{1/2}, F = 3 \rightarrow 5P_{3/2}$ transition, giving $v_g = 0.007c$. When a coherent light passes through the nonlinear medium, the photons experience twice the sudden jumps of interaction parameter upon crossing the nonlinear medium's front and back faces. And the Kerr nonlinearity resulting from atomic resonance causes a repulsive interaction between the photons. This interaction appears suddenly at the entrance of the rubidium cell and drops to zero rapidly at the exit plane of the cell. Back-propagating light waves caused by reflection on the interfaces would break the positive-z laser propagation reformulation in terms of effective time evolution. To avoid dealing with them, we assume that the surfaces of the nonlinear-dielectric layer have a perfect anti-reflection coating. When the sudden change of the photon-photon interaction strength from zero to $g \neq 0$ occurs at $z = 0$, pairs of correlated Bogoliubov waves of opposite wave vectors $\pm\mathbf{k}$ are spontaneously emitted.

In such a configuration, the photon-photon interaction constant undergoes a sudden hat-shaped modulation along the optical axis. What is interesting for us is that the sudden emergence of the interaction at the entrance plane can mimic the universe's contraction process. The rapid decrease of the interaction at the exit plane of the cell can be used to simulate the expansion of

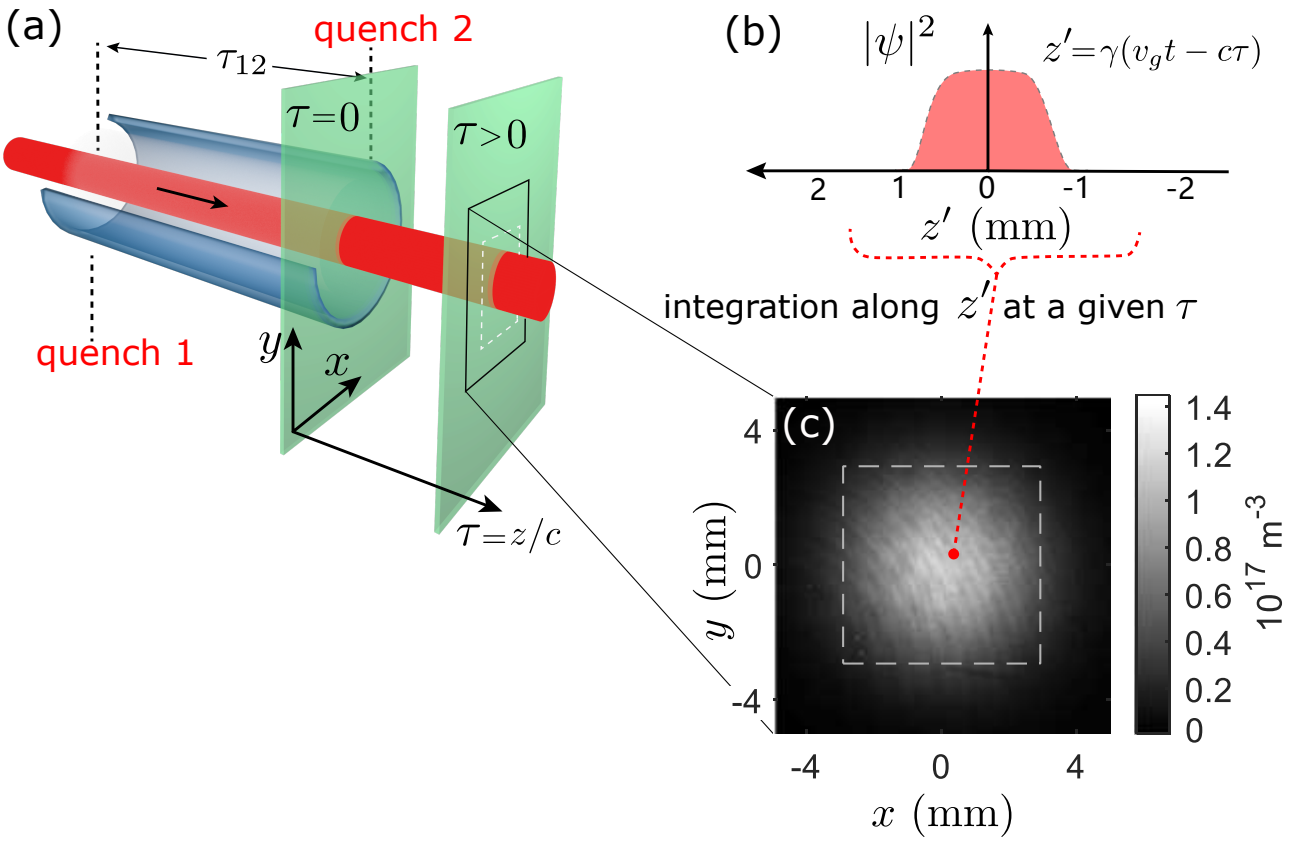

Figure 5.1: The analogue universe. **a** The fluid of light (red) is a laser pulse traversing a heated ^{85}Rb vapor cell. The axial position gives the effective time τ. The quenches occur at the entrance and exit of the vapor cell. $\tau = 0$ corresponds to quench 2. The time between the two quenches is τ_{12}. **b**. The true time gives an effective third spatial dimension z'. **c**. The typical image of the fluid of light integrated along z', given in units of photon density. An effective time $\tau = 103$ ps after quench two is shown.

the Universe. As a result of these two quenches, the fluid of light gets excited, and its quantum state, after the conservative evolution across the nonlinear material can be reconstructed from the statistical properties of the transmitted light. The resulting quantum correlations appearing in the transmitted light reveal the spontaneous emission of correlated counterpropagating excitations in the photon fluid.

The fluid of light is imaged on a CMOS camera, as shown in Fig.5.1(a). We tune the imaging system to pick out a certain z after the cell by fixing the effective time τ after the second quench. And the camera integrates over true time, as illustrated in Fig. 5.1(b). The power spectrum is computed by 2-dimensional Fourier transforms within the dashed square shown in Fig.5.1(c).

In the Fig.5.2, we observe the ring patterns in $S(k_x, k_y, k_{z'=0})$, oscillating as a function of k. Pairs of quasiparticles with momenta $\pm\mathbf{k}$ are generated at the moment of the quench with a random overall phase. A definite phase relationship between $+\mathbf{k}$ and $-\mathbf{k}$ oscillating with various frequencies ω_k. The synchronous generation ensures the phase coherence of the acoustic wave, while the sound speed v relates the time and length scales of wave dynamics. Assume that two counter-propagating waves with momenta $\hbar k$ and $-\hbar k$ are created with a relative phase ϕ, After propagating for a time τ, the waves interfere constructively when $2kv\tau + \phi = 2m\pi$ and destructively when $2kv\tau + \phi = 2(m - 1/2)\pi$, where m is integer. This explains why we see in Fig.5.2 that the interfering bright and dark ring fringes because only certain k-values interfere constructively at the observation time τ, resulting in a ring pattern. The rings shrink with τ since lower frequencies take longer to develop oscillations. The shrinking pattern of the rings is described quantitatively by the Eq.5.2, indicated by the dashed green curve.

The azimuthal averages $S(k)$ of $S(k_x, k_y, k_{z'=0})$ are indicated in black in Fig.5.3. The red curves are calculated from Eq.5.2, taking into account two quenches, and the variations in α, β, ω_k, which result from the measured absorption. It is clear that there is a great agreement between the experimental black and theoretical red curve. The most noticeable feature in Fig.5.3 is that density fluctuations of the sample after the quench show a multi-peak structure in the power spectrum. Depending on the value of the wave vector k, the emission processes at the back interfaces reveal constructive or destructive interferences at well-defined periods. The multiple peaks and troughs in momentum space result from the interference of sound waves with different wavelengths and are the key features of Sakharov oscillations in the angular spectrum of the CMB radiation. Moreover, At $\tau = 0$, the feature is not so clear, as a result of strong interaction adds a short correlation length. After the quench, the fluctuations amplify: a peak in the spectrum quickly appears in the first few picoseconds, and its location moves towards small k as time τ increases. The moving acoustic peaks as time evolves suggest that the correlations are spreading out at a finite speed of sound. This behavior supports the picture of phonons in the quantum fluid of light created coherently and can interfere at later times.

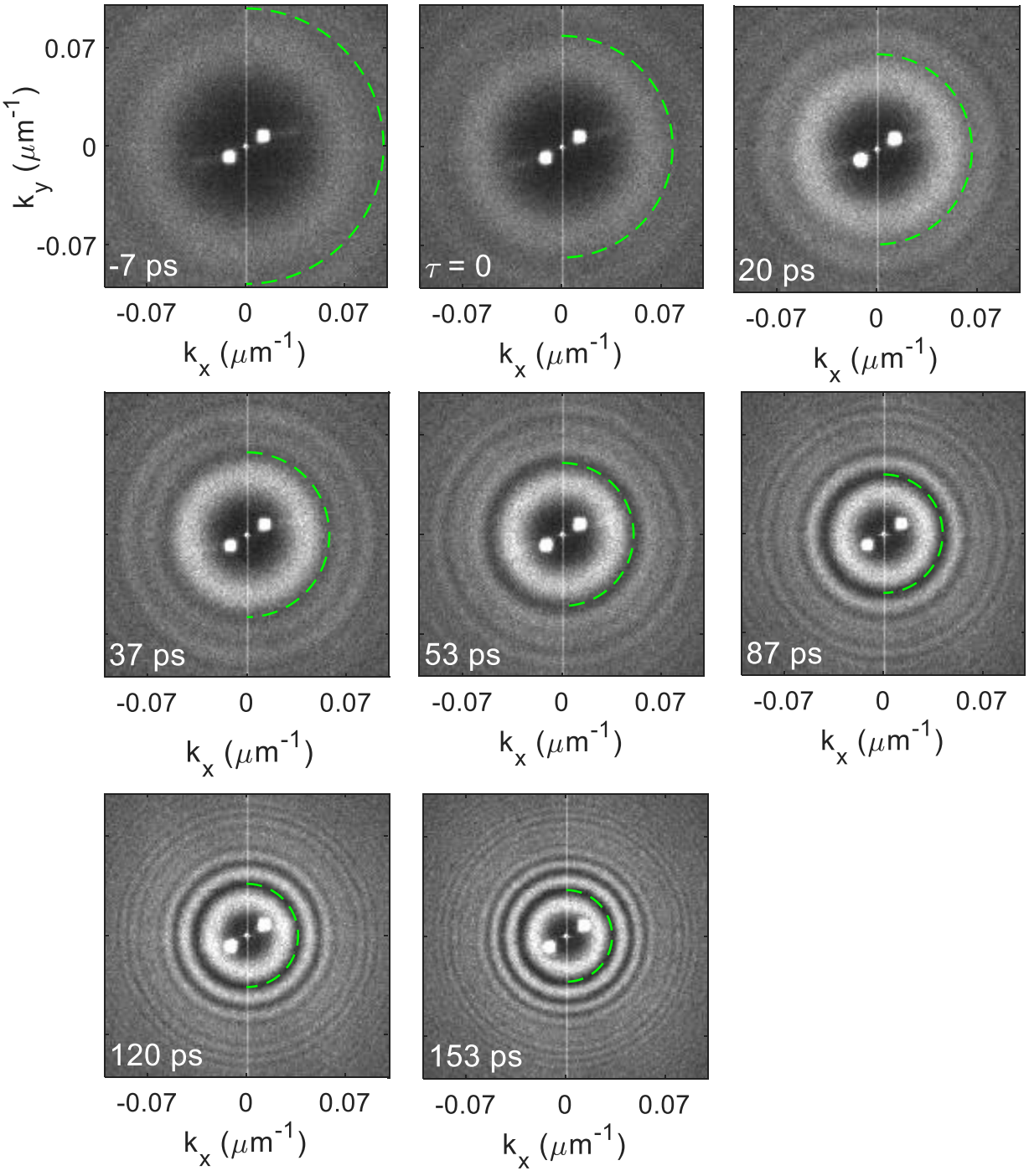

Figure 5.2: The static structure factor $S(k_x, k_y, k_{z'=0})$ at various times after the second quench. The dashed green curves indicate the first minimum of the red curves in Fig.5.3. The symmetric white points near the center of all panels are due to spurious fringes in the imaging system.

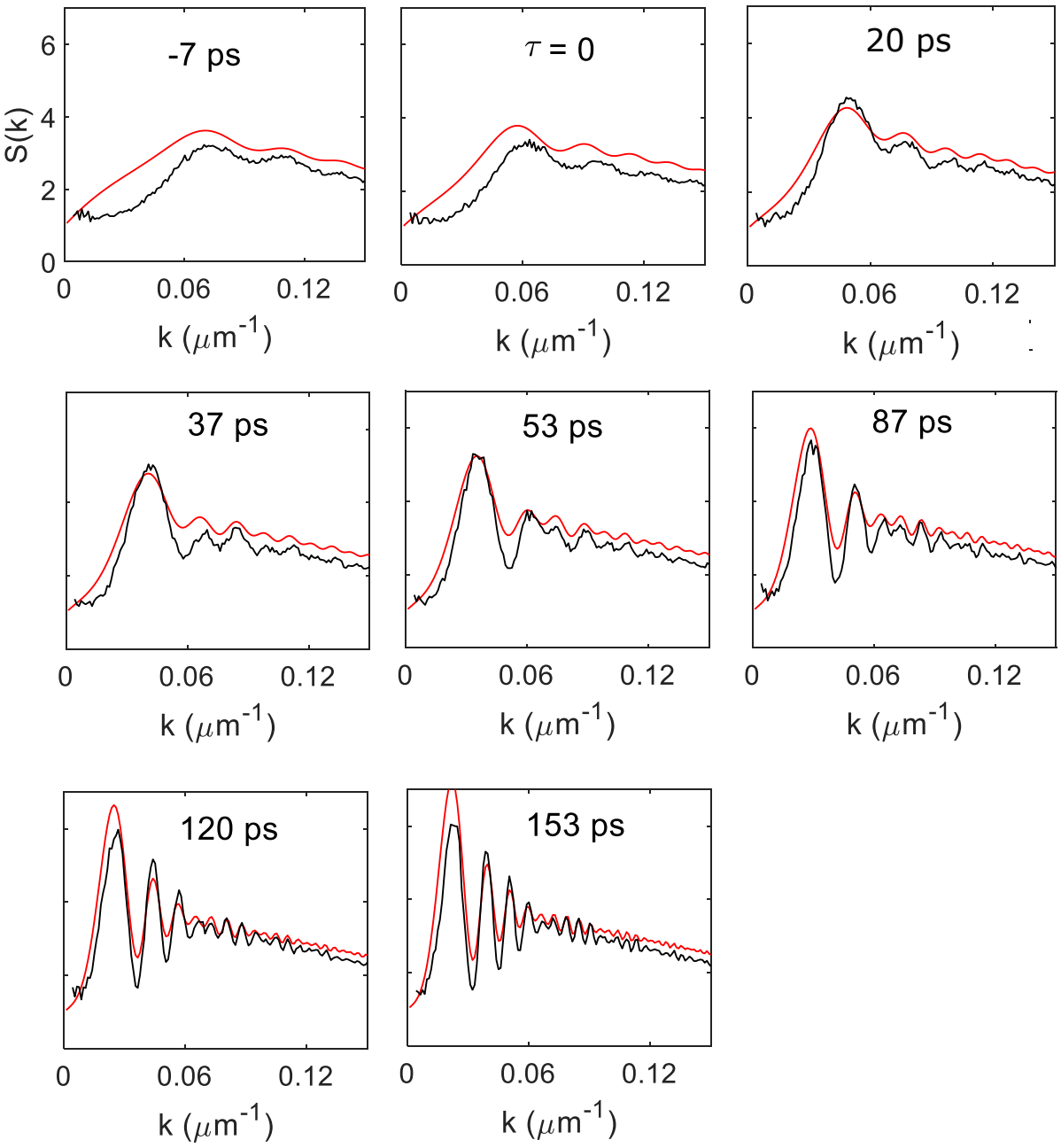

Figure 5.3: Radial Profile s of Fig.5.2 The black curves are the experimental data. The red curves are the prediction for analogue cosmological particle creation from the Eq.5.2.

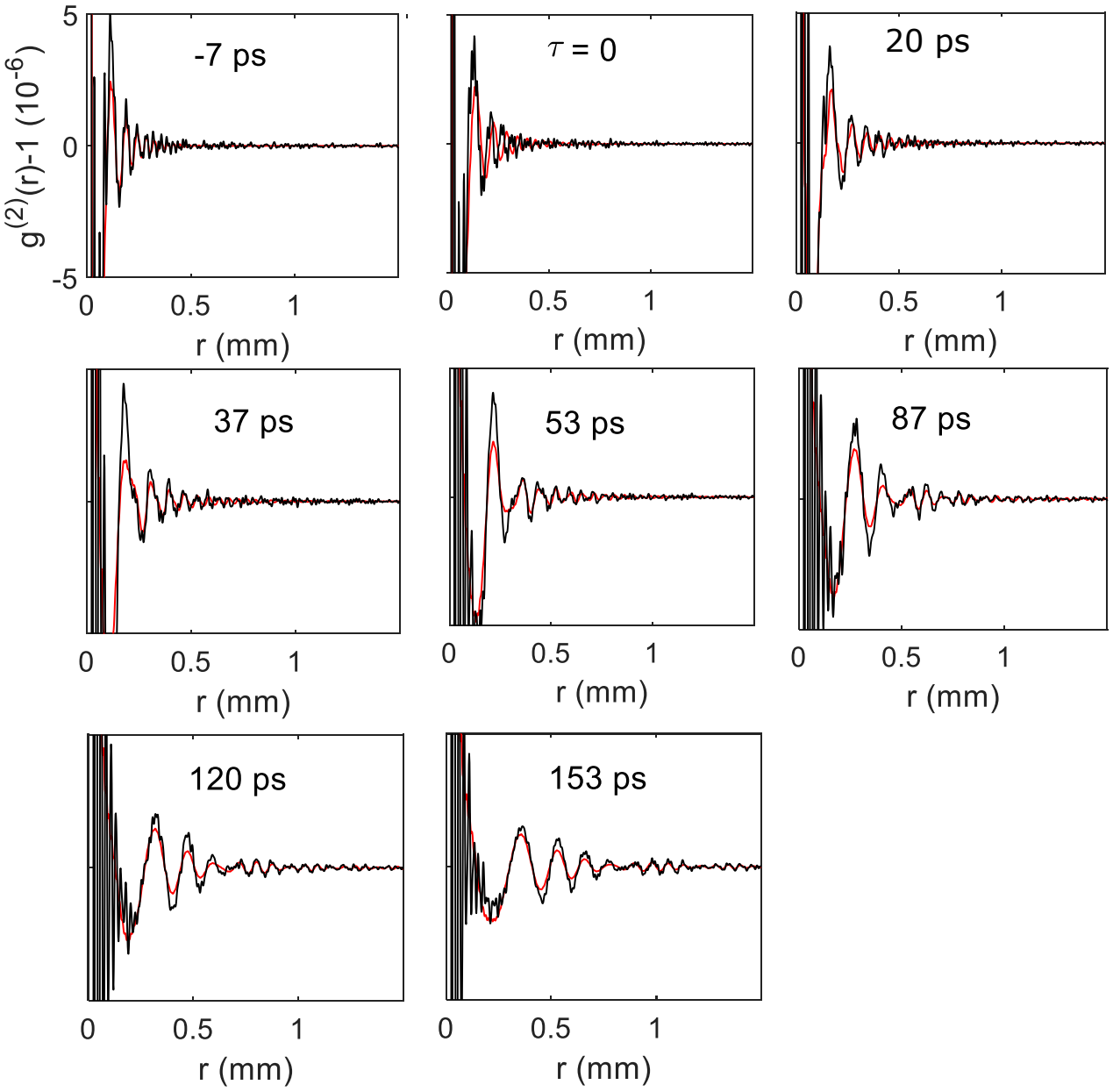

Figure 5.4: Density-density correlations. The experimental (black) and the theoretical (red) curves are obtained from **b** by the spherical Fourier transform of Eq.5.5.

We also demonstrate the spatial density correlations produced by the analogue cosmological particle creation. We derive the density-density correlation function $g^{(2)}(r)$ from the $S(k)$ by spherically-symmetric Fourier transform:

$$g^{(2)}(r) - 1 = \frac{1}{2\pi^2\rho} \int dk k^2 \frac{sin(kr)}{kr} [S(k) - 1] \tag{5.5}$$

At the back face of the nonlinear medium, the correlation between counterpropagating Bogoliubov excitations generated by the quench of the optical nonlinearity at $z = 0$ result in an oscillatory structure in the $g^{(2)}$ function. Fig.5.4 shows $g^{(2)}(r) - 1$, found by applying Eq.5.5 to fig.5.3. The oscillations are spherical shells propagating outward. This oscillatory behavior of the correlation function can be interpreted as resulting from a dynamical Casimir emission of elementary excitations on top of a quantum fluid of light presenting a quench of the photon-photon interaction constant. The amplitude of the fringe pattern diminishes as the separation distance r grows: The correlations between Bogoliubov excitations of opposite momenta are naturally all the weaker as the excitations are separated in space and time. The correlations are seen to reach increasing distances as time increases. They are on the order of 10^{-6}, which implies that the relative density fluctuations are on the order of 10^{-3}. The oscillations are clear despite the small signal, due to the high sensitivity of the optical detection. The theoretical red curves are obtained by applying Eq.5.5 to Eq.5.2, and quantitative agreement with the experimental curves are seen.

5.4 Conclusion

This experiment further establishes that the paraxial quantum fluid of light is an important participant in quantum fluids by sending a near-resonant pulsed laser beam through a warm rubidium vapor cell. In this configuration, the direction of propagation of the laser beam can be considered as the effective time in the Bose-Einstein condensates. With this device, we studied how a quantum fluid reacts to rapid changes in interaction in the second quench and have demonstrated the stimulated generation of analogous cosmological particles in the quantum fluid of light [32]. We evaluate the density structure factor after the second quench to study the evolution of the density fluctuations and search for the Sakharov oscillations. And an acoustic peak was observed in the density power spectrum, resembling those in the angular spectrum of CMB radiation.

Chapter 6

Turbulence in two counter-propagating fluids of light

Turbulence, characterized by cascades of excitations across lengthscales, is ubiquitous in nature [80]. Quantum turbulence studies the turbulence phenomenon in quantum fluids with special quantized vortices and is common with its classical counterparts. Although the superfluid turbulence has been studied for centuries and some universal and classical properties have been found, such as the same Kolmogorov energy spectrum in three-dimensional (3D) turbulence. However, incompressible two-dimensional (2D) classical fluids exhibit different flow characteristics. The existence of a range of length scales (the inertial range) over which kinetic energy is transferred from small to large length scales is known as an inverse energy cascade. It has been theoretically reported that the turbulence in super Helium and the cold atomic gas exhibit the key Kolmogorov $-5/3$ law. But a major challenge is how to prove the inverse energy cascade experimentally. Here, we investigate hydrodynamics behaviors in fluid of light by interfering two photon fluids. We observe the emergence of statistical isotropy, a key phenomenon associated with the development of turbulence. Importantly, we also get the $k^{-5/3}$ Kolmogorov power law in the inertial range in the incompressible kinetic energy spectrum thanks to the easy access to the velocity in our two counter-streaming fluids of light configuration. This experiment paves the way for the experimental investigation of out-of-equilibrium dynamics in a homogeneous density configuration. The paper titled "Inverse energy cascade in two-dimensional quantum turbulence with fluids of light" is in progress.

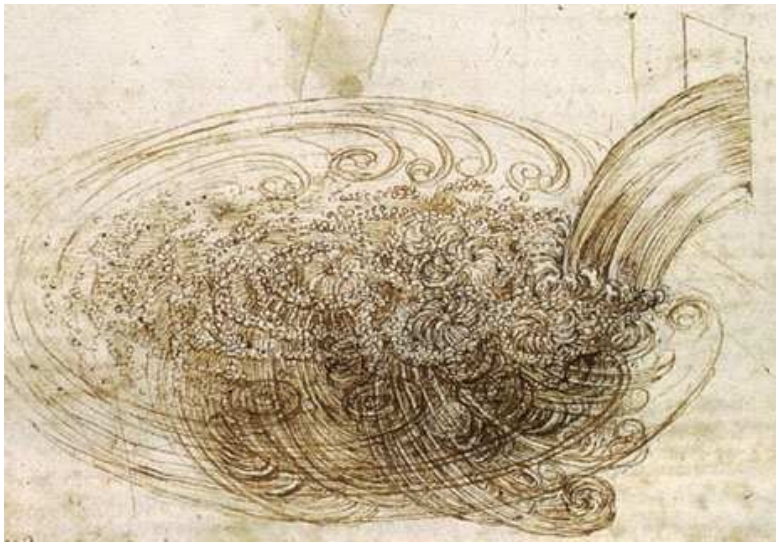

Figure 6.1: Leonardo da Vinci's Studies of water. The fall of a stream of water from a sluice into a pool. Source: Wikimedia Commons.

6.1 Background

Turbulence, one of the most common and striking phenomena in nature, was first described and investigated by Leonardo da Vinci. Fig.6.1 shows a pattern of vortices of various sizes. Since then, studying the turbulence phenomenon underlying the oceans [81], atmosphere, and supernovae [82] has drawn much attention from scientists since it was believed to be the last question unsolved in the classical physical community. Turbulence, characterized by a large number of degrees of freedom, distributed over a substantial range of scales, produces a disordered state both in space and time. Although they have intricate spatiotemporal dynamics, turbulent flows frequently follow a universal law: transfer of energy from large to small length-scales in turbulent flows in Fourier space discovered by Kolmogorov in [83]. Although it has a unique and important role in modern physics, it is a sad story that not only can we tell more about how turbulence appears, it is impossible for us to predict the behavior of turbulence at a given time until today.

6.1.1 Classical turbulence (CT)

When we think of "turbulence," a wide range of living phenomena come to mind. Maybe you wish to give a precise description and definition of turbulence. In fact, many physicists have attempted to do it in this manner. However, due to the difficulty of giving a general and complete definition, more researchers are inclined to abandon the formal definition in favor of intuitive characterizations since we haven't learned enough about turbulence until this point. It was believed that turbulence in a classical fluid is expected to exhibit all of the following main features [80, 84]:

1. **Irregularity**

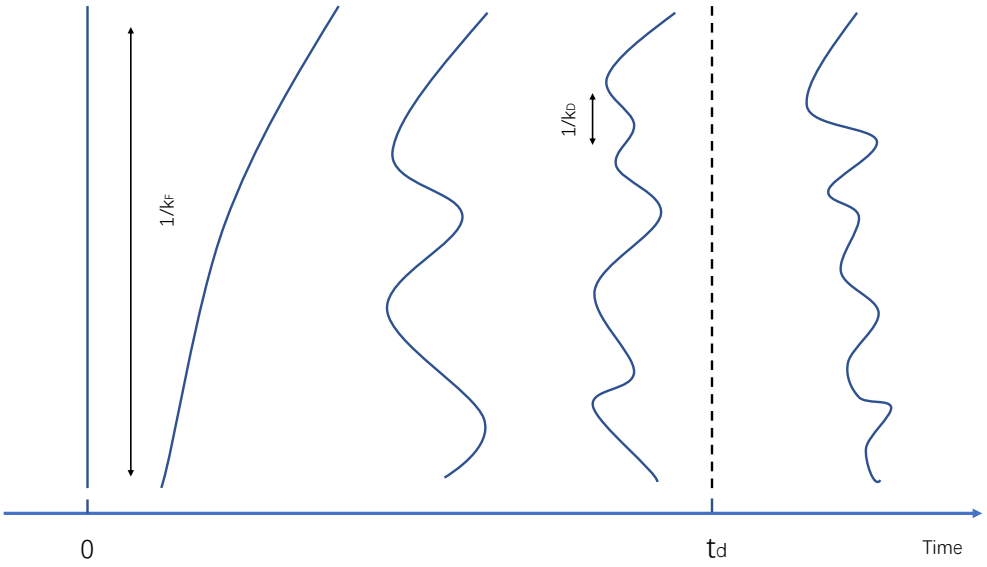

Figure 6.2: Cartoon of a turbulent wave's dynamics in real space. By forcing the matter-wave field at a significant lengthscale, $1/k_F$, energy is introduced, and it propagates to smaller scales as a result of nonlinear interactions. Once the excitations reach the $1/k_D$ small dissipation lengthscale at time t_d, a steady state can be created.

The turbulent flow is a random, free, and chaotic spectrum of different scales. The turbulent vortex exists for a limited time in a specific region of space before being destroyed. The smallest vortices at the far end of the spectrum are converted into thermal energy by viscous forces, causing the temperature to rise.

2. **High diffusivity and thus efficient mixing**

   The diffusivity and exchange of momentum increase in a turbulent flow. Increased diffusivity raises resistance (wall friction) and heat transfer in internal flows like channels and pipes.

3. **High Reynolds numbers**

   Reynolds studied the transition from laminar to turbulent flows in a pipe and used the Reynolds number to characterize the behavior of dye streak flow in a pipe with a smooth, transparent wall: $Re = \rho U L/\mu$, where ρ is the flow density, μ is the viscosity, the L is the length of the pipe, and U is the velocity. Reynolds number can also be translated to the ratio of inertial forces to viscous forces within a fluid subjected to relative internal movement due to different fluid velocities. Reynolds concluded that turbulence takes place at high Reynolds numbers.

4. **High Dissipation**

At the moment, all of our understanding on turbulence is based on Richardson's theory, which states that energy injected into a system at a large lengthscale flows without loss through momentum space until it is dissipated at some small lengthscale at the same rate in the 1920s [85]. This no dissipation occurs range, called inertial range, or intermediary range, was independent of viscosity. We describe this turbulence cascade process in fig.6.2: The field is continuously forced from the mean flow at a large length scale $1/k_F$, and the excitation propagates to smaller length scales due to nonlinear interactions until kinetic energy in small vortices is converted to thermal energy. The energy is dissipated at k_D at the same rate as it is injected at k_F. This scaling is thought to arise from a Richardson cascade process as large vortices break up into smaller and smaller vortices until at very small scales, energy is dissipated.

In 1941, Kolmogorov proposed a universal law describing energy cascade with a self-similar behavior of the turbulent flow [83]. Assume in the simplest case of an isotropic and homogeneous steady state, the energy injected into the system at the largest length scale F to the smallest one D, with a constant dissipation rate ϵ as shown in fig. 6.3. The Reynolds number connects these length scales, $D/F \approx Re^{-3/4}$. Instead of working in real space, it is convenient to go to the momentum space to describe the cascade as a function of wavenumbers $k = 2\pi/r$. Kolmogorov revealed that some aspects of turbulence are universal in the inertial range: the kinetic energy is given by $E_k = C\epsilon^{2/3}k^{-5/3}$.

5. **Continuum**

   Although the flow has small turbulent scales, they are much larger than the molecular scale and can be considered a continuum.

6.1.2 Quantum turbulence

In comparison to classical fluids, superfluids exhibit fascinating characteristics such as irrotational and frictionless flow, raising fundamental questions about the nature of turbulent cascades [86]. Classical turbulence is made up of vortices with different vorticity and size, and in order to mathematically analyse viscous fluid dynamics, the Navier-Stokes equation must be solved[87]. QT, on the other hand, is made up of simpler vortices structure, each with a well-defined vortex core and quantized circulation. Because superfluid flow is inviscid, vortices cannot decay through viscous vorticity diffusion. In fact, the term QT was first used in 1982 by Barenghi in his Ph.D. thesis [88]. Donnelly and Swanson, who adopted the term in 1986, were responsible for the shift from the commonly used superfluid to QT [89]. This change was not simply a matter of terminology; it showed that turbulence had more to do with the quantization of vortices than the lack of viscosity of superfluids.

Despite differences due to the nature of vortices, classical and quantum turbulence share pro-

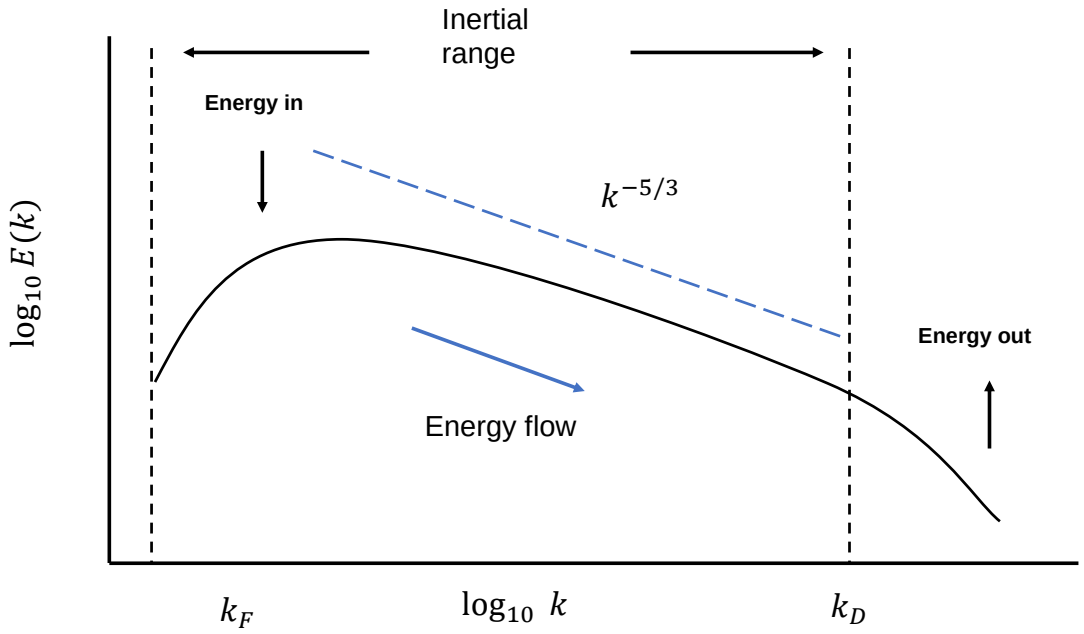

Figure 6.3: Energy injection at large lengthscales at k_F and transfer it over the inertial range to the small lengthscale at k_D. The incompressible energy cascade exhibit the $k \sim^{-5/3}$ law.

found similarities that highlight turbulence's universality. In 3D turbulence, the vortex core structure is unimportant in locations far from vortex cores and for length scales greater than the average intervortex spacing. The quantized vortex lines are analogous to vortex filament lines in an Euler fluid [90]. Therefore, the classical and quantum turbulence exhibit same Kolmogorov spectrum $E(k) \sim k^{-5/3}$ in the inertial range for 3D turbulence.

QT experiments have been conducted for over half a century with superfluid helium systems[91]. Because superfluid ^{4}He and ^{3}He-B systems have a wide range of accessible length scales, turbulent vortex tangles can contain hundreds of thousands of vortices. The intrinsic superfluid parameters, such as the fixed strength of atom-atom interaction and the homogeneous density make it a good participant in the study of quantum turbulence. The same classical Kolmogorov scaling has been verified numerically and experimentally in liquid helium [92, 93, 94]. However, controlling single-vortex dynamics in a turbulent ^{4}He and ^{3}He-B superfluid is extremely difficult. Moreover, the strong interaction between atoms in liquid and superfluid helium limit the theoretical understanding [95].

Superfluid Bose-Einstein condensates (BECs) have recently received attention because many condensate parameters can be finely controlled. By adjusting an external magnetic field around a Feshbach resonance, one can control the strength of atom-atom interactions[96]. Moreover, the visualization of vortex cores thanks to the imaging techniques make it more easier to explore to control individual vortex dynamics and position. The presence of a Kolmogorov spectrum has also been established in numerical studies of 3DQT in trapped and homogeneous atomic

condensates using the Gross-Pitaevskii equation (GPE) [97, 54, 98]. These evidence has sparked intense interest in the similarities between classical turbulence (CT) and quantum turbulence (QT), with the belief that a quantitative understanding of aspects of QT may aid in a broader understanding of the whole turbulence subject.

There are lots of papers that reported the quantum vortices and turbulence in the atomic BECs. For example, the São Carlos group was responsible for the first evidence of QT in trapped dilute atomic BECs and found turbulent cloud expands keeping the ratio between their axis constant in 2009 [55]. It has been demonstrated that the formation of clusters of quantum vortices is triggered by the increase of the incompressible kinetic energy per vortex [99]. The observation of a cascade process characterized by an isotropic power-law distribution in momentum space has been reported by driving a Bose-Einstein condensate in an optical box out of equilibrium with an oscillating force that pumps energy into the system at the largest length scale [100]. The Kelvin-Helmholtz instabilities, which were believed to occur at the interface of two fluids with a relative motion and give rise to the formation of the vortices, have been demonstrated to contribute to nucleating the vortices and eventually lead to the turbulent state by directly observing the quadrupolar modes, as well as vortex structures in the interface of the dense core [101].

It is critical to ascertain whether the highly excited state is truly QT. Several ways for identifying the turbulent state are explored in this part.

Signature of quantum turbulence

1. Power low

What concerns us is how to know a N excited state is the quantum turbulence. It has been demonstrated that if the incompressible kinetic energy spectrum of the turbulent regime obeys Kolmogorov's $-5/3$ law [102], we could be sure that the system is turbulent.
The wave function of the condensate can be written as

$$\Psi(\mathbf{r},t) = \sqrt{n(\mathbf{r},t)}e^{i\theta(\mathbf{r},t)} \tag{6.1}$$

The kinetic energy E_{int} can be expressed as sum of the superfluid kinetic energy E_k and quantum pressure energyE_q: $E_{int} = E_k + E_q$, where the $E_k = (\hbar^2/2m)\int d\mathbf{r}\,|\sqrt{n}\nabla\theta|^2$ and the $E_q = (\hbar^2/2m)\int d\mathbf{r}\,|\nabla\sqrt{n}|^2$.The quantum pressure energy only happens when there are sharp variations in the condensate density, such as at vortex cores, dark solitons, and other density discontinuities. The vector field $\sqrt{n}\nabla\theta$ can be divided into incompressible and the compressible components: $\sqrt{n}\nabla\theta = (\sqrt{n}\nabla\theta)^i + (\sqrt{n}\nabla\theta)^c$, where the $\nabla\cdot(\sqrt{n}\nabla\theta)^i = 0$ and $\nabla\times(\sqrt{n}\nabla\theta)^c = 0$. Therefore, the incompressible and compressible kinetic energy is defined as: $E_k^{i,c} = (\hbar^2/2m)\int d\mathbf{r}\,|(\sqrt{n}\nabla\theta)^{i,c}|^2$. They correspond to kinetic energy and sound waves, re-

spectively. As a result of the incompressible and compressible fields orthogonal, it follows the: $E_k = E_k^i + E_k^c$. The kinetic energy spectrum as a function of the wavenumber k is defined as:

$$\epsilon_k^{i,c} = \frac{\hbar^2}{2m} \int k^2 sin\theta d\theta d\phi \left| \int e^{i\mathbf{k}\cdot\mathbf{r}} (\sqrt{n}\nabla\theta)^{i,c} \frac{d\mathbf{r}}{(2\pi)^3} \right| \tag{6.2}$$

such $E_k^{i,c} = \int_0^\infty \epsilon_k^{i,c}(k)dk$. The Kolmogorov laws states that the incompressible energy spectrum obeys the power law $\epsilon_k^i(k) \approx k^\nu$ where over the range of k [54].

***2. Vortex line density** L **on** t*

The structure of the quantum turbulence is reflected in the time dependence of the decay of the total vortex line density L after tuning off the excitation that sustains the turbulence. Correlations of vortex tangles can be classified into two kinds [93]: correlated vortex tangle and uncorrelated vortex tangle. For the correlated vortex tangle, it exhibits the Kolmogorov spectrum. The energy is then transferred to smaller scales by Richardson cascades, and L decays as $t^{-3/2}$. For the uncorrelated vortex tangle, L decays as t^{-1}.

3. Self-similar expansion

Another remarkable feature of quantum turbulence observed by Henn et al. The turbulent state does not expand like either a quantum or a thermal but has a similar expansion preserved the initial aspect ratio [55].

6.1.3 Two-Dimensional Turbulence

A direct Kolmogorov $k^{-5/3}$ cascade from the forcing scale to the dissipated scale in the inertial range is visible in 3D turbulence. 2D turbulence is the approximate counterpart produced in the laboratory to simplify complex situations. Due to the presence of enstrophy, incompressible two-dimensional (2D) classical fluids display very different flow characteristics [103]. Energy flux toward shorter scales is suppressed in two-dimensional (2D) flows subject to small-scale forcing, while kinetic energy is transported toward larger scales. These interactions result in the well-known inverse energy cascade (IEC). This phenomenon is well-known in classical fluids and is thought to be the cause of Jupiter's great red spot [104] and was observer in soap films [105]. Despite the fact that there is a wealth of information regarding 3DQT in BECs [106]. However, the proof of inverse energy cascade in the turbulence experiment is still missing. Understanding the fundamental characteristics of 2DQT requires additional work.

6.2 Turbulence in the quantum fluid of light

As we have know that one major aspect that remains unexplored in quantum turbulence is the experimental demonstration of an inverse energy cascade. In this work, we want to show that a 2D quantum fluid contains an inverse energy cascade by using the fluid of light platform. Two counter-streaming phonon fluids with controlled velocities and densities collide to create the turbulence. We are able to directly measure the fluid velocity and divide it into compressible (linked to phononic-excitations) and incompressible (linked to vortices) components thanks to optical techniques. This allows us to access to the role of vortices in the appearance of power law decay of the kinetic energy. In addition, we also study the other hydrodynamics behaviors of the quantum turbulence.

6.2.1 Numerical simulation

Two-stream instability is a widely studied phenomenon. In the paper [42], the author develops a theory to describe the onset of the kinetic instability in the case of two photon fluids of light with different velocities interacting in the nonlinear medium. This instability rooted in the resonant energy transfer from the drift velocity to the elementary Bogoliubov excitations of the photon gas. Inspired by this paper, we We use paraxial fluids of light in hot atomic vapors to observe the hydrodynamic phenomena by varying the ratio of flow velocity to sound speed of collective Bogoliubov excitations.

Let's first analyze the behavior of the dispersion relation between two 2D photon fluids. [42]. We have two photon fluids of light and these two fluids satisfy the hydrodynamic equation 1.12 and 1.13. To clarify this derivation, we rewrite the hydrodynamic equation here.

$$\frac{\partial \rho}{\partial z} + \nabla_\perp(\rho v) = 0 \tag{6.3}$$

$$\frac{\partial v}{\partial z} + (v \times \nabla_\perp)v = -\frac{g}{nk_0}\nabla_\perp \rho + \frac{1}{2}\nabla_\perp\left(\frac{1}{\sqrt{\rho}}\nabla_\perp^2\sqrt{\rho}\right) \tag{6.4}$$

The term inside the brackets on the right side of the Euler equation can be simplified to:

$$\nabla_\perp^2\sqrt{\rho} = \nabla_\perp\left(\frac{1}{2\sqrt{\rho}}\nabla_\perp\rho\right) = \frac{1}{2\sqrt{\rho}}\nabla_\perp^2\rho - \frac{1}{4}\frac{1}{\rho^{3/2}}(\nabla_\perp\rho)^2 \tag{6.5}$$

$$\frac{1}{\sqrt{\rho}}\nabla_\perp^2\sqrt{\rho} = \frac{1}{2\rho}\nabla_\perp^2\rho - \frac{1}{4}\frac{1}{\rho^2}(\nabla_\perp\rho)^2 \tag{6.6}$$

Finally, the second term in Euler's right side equation is expressed as:

$$\frac{1}{2}\nabla_\perp\left(\frac{1}{\sqrt{\rho}}\nabla_\perp^2\sqrt{\rho}\right) = \frac{1}{4}\left(\frac{1}{\rho} - \frac{1}{\rho^2}\right)\nabla_\perp^3\rho \tag{6.7}$$

Now, we consider two fluids with the same density but one is considered as rest and another photon fluid propagating with the velocity v_0,:

$$\rho_{1,2} = \frac{\rho_0}{2} + \delta\rho_{1,2} \tag{6.8}$$

$$v_1 = \delta v_1, v_2 = v_0 + \delta v_2 \tag{6.9}$$

Inserting the above equations into the fluid dynamics equation, we get:

$$\frac{\partial}{\partial_z}\left(\frac{\rho_0}{2} + \delta\rho\right) + \nabla_\perp\left(\left(\frac{\rho_0}{2} + \delta\rho\right)\delta v\right) = 0 \tag{6.10}$$

$$\frac{\partial \delta v}{\partial z} + (\delta v \cdot \nabla_\perp)\,\delta v = -\frac{g}{nk_0}\nabla_\perp\delta\rho + \frac{1}{2\rho_0}\nabla_\perp^3\delta\rho \tag{6.11}$$

For the first fluid, we have:

$$\frac{\partial}{\partial_z}\delta\rho_1 + \frac{\rho_0}{2}\nabla_\perp(\delta\rho_1) = 0 \tag{6.12}$$

$$\frac{\partial \delta v_1}{\partial z} + (\delta v_1 \cdot \nabla_\perp)\,\delta v_1 = -\frac{g}{nk_0}\nabla_\perp\delta\rho_1 + \frac{1}{2\rho_0}\nabla_\perp^3\delta\rho_1 \tag{6.13}$$

The same applied for the second fluid,

$$\frac{\partial}{\partial_z}\delta\rho_2 + \frac{\rho_0}{2}\nabla_\perp(\delta\rho_1) + v_0 \cdot (\nabla_\perp\delta\rho_2) = 0 \tag{6.14}$$

$$\frac{\partial \delta v_2}{\partial z} + (\delta v_2 \cdot \nabla_\perp)\,\delta v_2 = -\frac{g}{nk_0}\nabla_\perp\delta\rho_2 + \frac{1}{2\rho_0}\nabla_\perp^3\delta\rho_2 \tag{6.15}$$

Here, we assume that:

$$\delta\rho_{1,2} = A_{1,2}e^{ikr_\perp - i\Omega z} \tag{6.16}$$

where A_i is the amplitude, $\mathbf{k}$ is the transverse wave vector and Ω represents the frequency of the elementary excitations. Inserting the eq.6.16 to the above hydrodynamics equations, finally the dispersion relation can be expressed as:

$$1 - \frac{1}{2}c_s k^2\left(\frac{1}{\Omega^2 - k^4/4} - \frac{1}{(\Omega - \mathbf{v_0}\cdot\mathbf{k})^2 - k^4/4}\right) = 0 \tag{6.17}$$

Where the $c_s = c\sqrt{\Delta n}$ is the speed of the sound of the photon fluid. The Bogoliubov dispersion of the weakly interacting Bose gas, which describes an acoustic regime at low momenta, can be derived from eq.6.17. We also define the healing length $\xi = \dfrac{1}{k_0\sqrt{|\Delta n|}}$ as the scale where the fluid behavior break and turns into a single-particle regime.

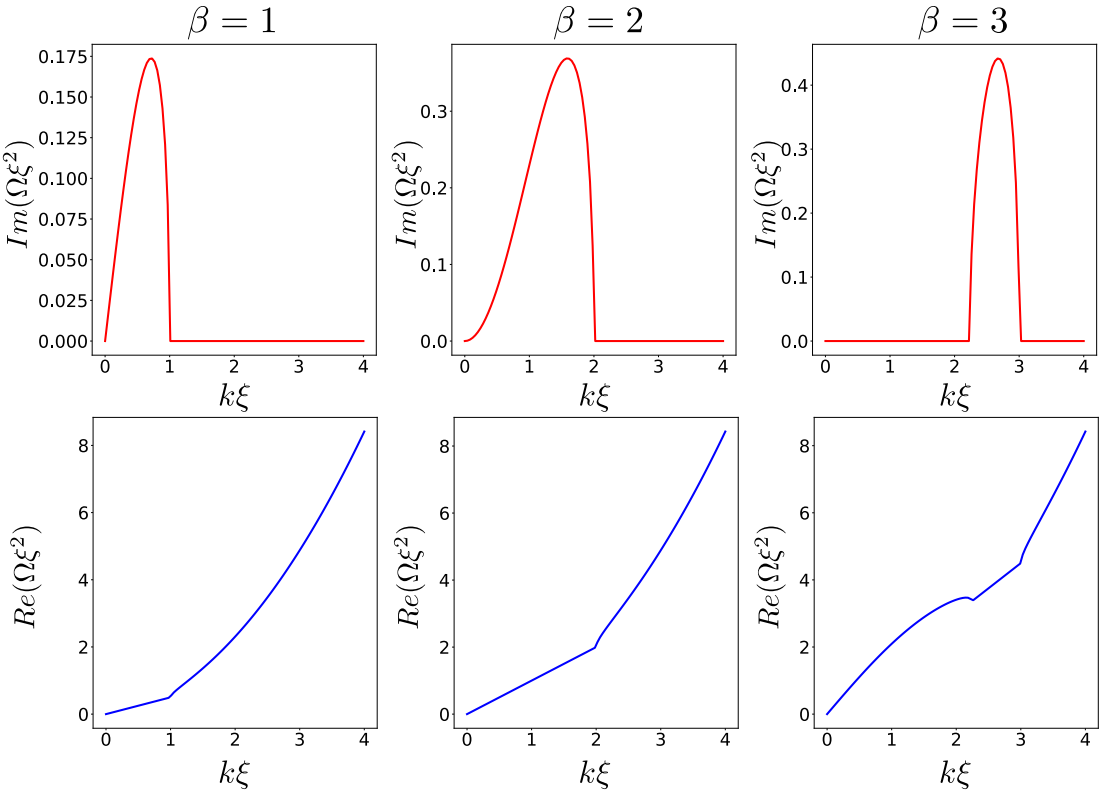

Figure 6.4: Imaginary and real parts of the dispersion relation of two-fluid system. From left to right, indicating the velocity of the fluid is increased, corresponding to Mach number $\beta = 1$, $\beta = 2$, $\beta = 3$.

Then the solution gives:

$$\Omega\xi^2 = \frac{1}{2}k\xi\left(\beta \pm \sqrt{2 + \beta^2 + (k\xi)^2 \pm 2\sqrt{1 + 2\beta^2 + \beta^2(k\xi)^2}}\right) \tag{6.18}$$

We obtain a two fluids counter-propagating modified Bogoliubov dispersion relation with unstable zones (Mach number $\beta = v_0/c_s$). Unlike the single-fluid dispersion relation, this collective excitation spectrum features a region of instability when the right-hand inside of the root of Eq.6.18 become negative. We also plot the real (blue curves) and imaginary parts (red curves) of the dispersion relation in fig.6.4 for the different flow velocities. We could find that there is always a region $\sqrt{\beta^2 - 4} \leq k\xi \leq \beta$ where the imaginary part of the dispersion relation is greater than zero. And it is in this region that there is a gain of energy. The system will dissipate excessive energy by generating vortices, which will cause instabilities similar to those seen in classical hydrodynamics.

We also employ a split-step Fourier method [107] to integrate the nonlinear Schrödinger equation in order to investigate the simulation model of the two fluid instabilities and the results shown in the fig.6.5. Panels (a)(b) depict a typical evolution of the two-fluid density

$\rho = |\phi|^2 = |E|^2$ for the linear case and nonlinear case. The instability develops slowly as one fluid propagates toward the other. As we can see for the nonlinear stage (b), vortex-antivortex pairs are formed. Panels (c)(d) show the phase distribution extracted from panels (a)(b). Panels (e)(f) present the Fourier spectrum of the region of interest from panels (a)(b).

6.3 Experimental design and result

6.3.1 Experiment method

This field propagates along the z-axis into a cylindrical cell of length $L = 5\ cm$ and diameter $D = 2.5\ cm$ filled with an isotopic mixture of 95% of ^{85}Rb and 5% of ^{87}Rb. Such a vapor behaves like a nonlinear medium whose strength can be tuned experimentally. The fluid is created with a μquans laser source whose wavelength λ is tuned near the D2 resonance of ^{85}Rb. The laser detuning can be adjusted from -5 to 5 GHz with respect to the $F = 3 \rightarrow F'$ transition of ^{85}Rb by the voltage applied on the laser device. In practical implementation, the detuning is set at $\Delta = -5$ GHz for the photon non-interacting case and $\Delta = -2$ GHz for the photon interacting case, which is large compared to the Doppler broadening (≈ 250 MHz) such that the Lorentzian shape of the line dominates. The atomic vapor density, as introduced in chapter 2, is controlled by adjusting and stabilizing the cell's temperature. To calibrate the value of n_2, we measure the far field intensity of a collimated Gaussian beam with the initial waist of 0.5 mm and peak intensity $I = 1.25 \times 10^6\ Wm^{-2}$. Due to self-phase modulation, this configuration generates curved fringes and provides a measurement of the nonlinear phase $\phi_{NL} = k_0 n_2 I L$ accumulated by the beam along its propagation. Here, we measure values of $n_2 = 6.75 \times 10^{-10}\ m^2 W^{-1}$. The nonlinearity can be adjusted through the beam intensity I, the detuning Δ or the atomic density of the vapour ρ_{at} (tunable with the vapour temperature).

The experimental setup is depicted in fig.6.6. An initial 500 mW laser beam is magnified with the telescope and then sent to a SLM. The SLM displays a vertical and horizontal grating, which imprints a phase modulation of wave vector $\Delta k_\perp$ that creates left and right two counter-propagating fluids of light with opposite velocities. The non-diffracted beam corresponds to the zero order of the grating and is cut by a slit in the Fourier plane. We only keep the first-order laser beam diffracted by grating after the SLM to eliminate the unmodulated reflection on the SLM. The beam waist $\omega = 0.5\ mm$ is locate at the entrance of the nonlinear medium $z = 0$ with a demagnification factor of 4, to increase its resolution. The experimental protocol consists of fixing the laser transmission by adjusting the laser detuning Δ after the cell has been heated to a given temperature T. Here, we control our Rubidium vapour cell temperature at $150°C$ (the atomic density of $\rho_{at} \approx 9 \times 10^{19}$ atoms $/m^3$) and a transmission of 4%. The output plane of the cell is imaged on the camera in order to observe the dynamics phenomenon of the fluid of light at different effective time $Z/Z_{NL}(Z_{NL} = 1/k_0\Delta n)$ within the non-linear medium [41]. Since the nonlinear medium has a finite size, reducing Z_{NL} through Δn mimics an increase of the effective propagated time. Another typical important lengths in the system is the healing

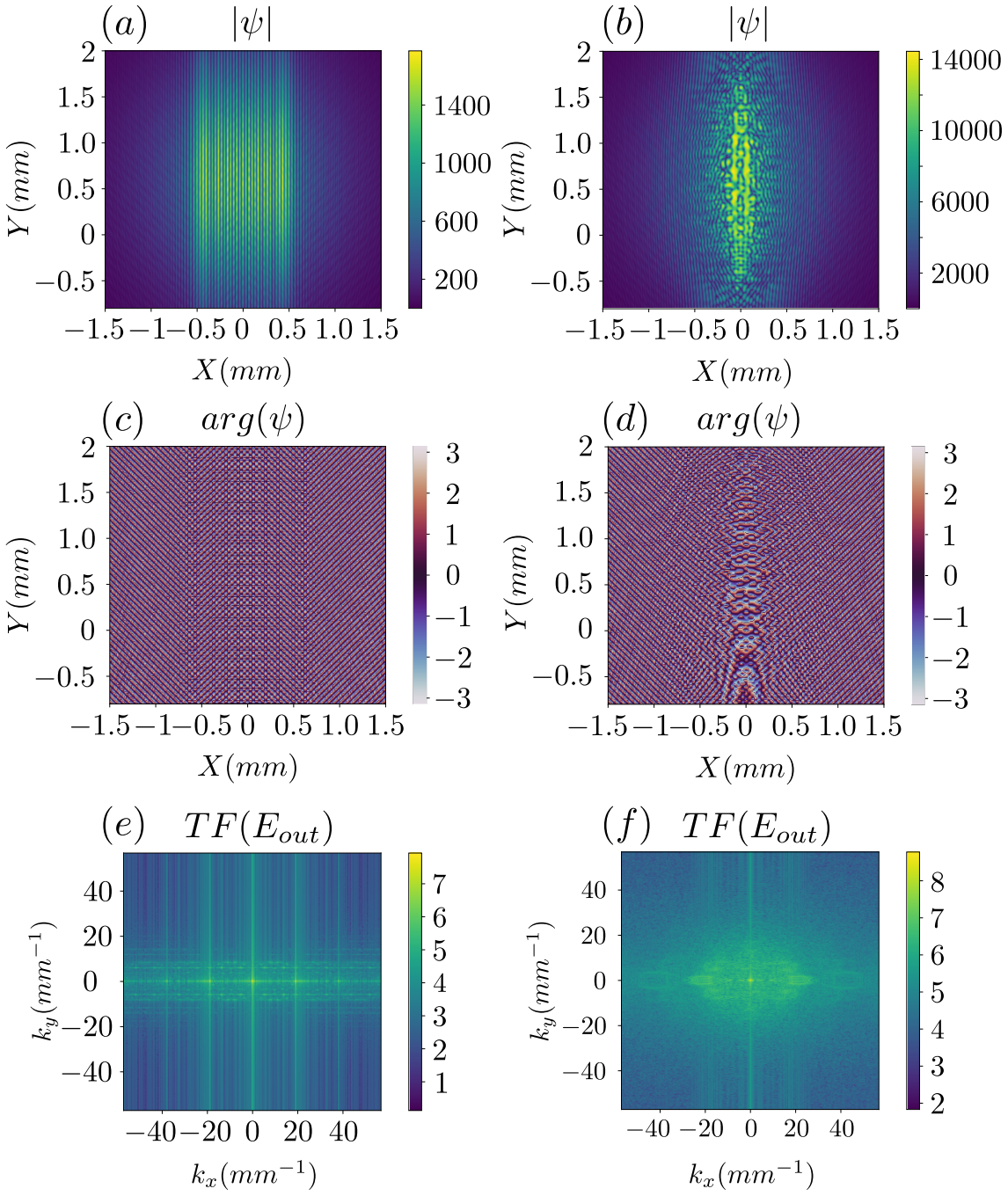

Figure 6.5: Numerical results on the two-stream instability. Panels (a)(b) depict a typical evolution of the two-fluid density $\rho = |\phi|^2 = |E|^2$ for the linear case and nonlinear case. The instability develops slowly as one fluid propagates toward the other. As we can see for the nonlinear stage (b), vortex-antivortex pairs are formed. Panels (c)(d) show the phase distribution extracted from panels (a)(b). Panels (e)(f) present the Fourier spectrum of the region of interest from panels (a)(b).

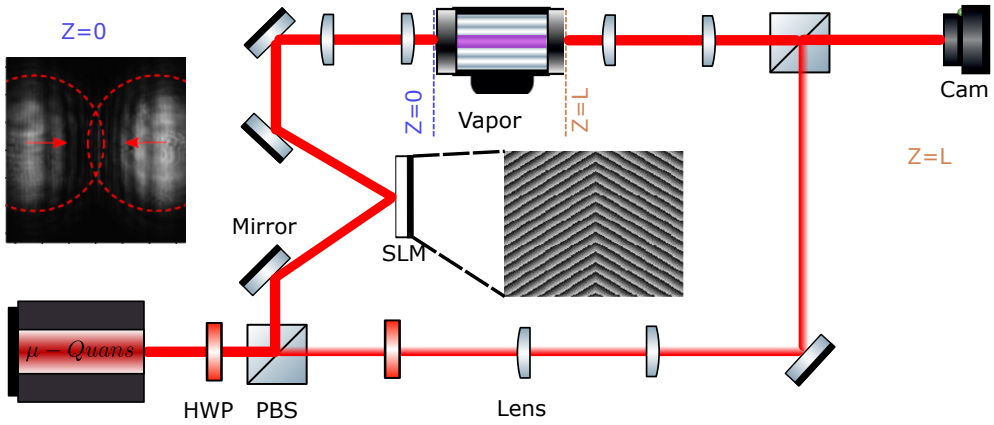

Figure 6.6: An experimental schematic representation of the experiment. The laser beam from μquans laser source split in two (pump beam and probe beam) by a polarizing beam splitter (PBS), coupled with a half-waveplate (HWP) to tune the power in each arm. A special phase is imprinted on the pump beam with a spatial light modulator (SLM) and then focused on the entrance of $L = 5\ cm$ rubidium cell heated at $150°C$ used to create two photon fluids propagating with different velocity. The probe beam as the reference beam interfere with the pump beam by putting them together at a beam splitter (BS) used to extract the relevant phase. A half-waveplate and a polarizer ensure that the reference has the same polarization as the pump. A camera is used to record the image at the exit plane of the nonlinear medium so as to see how the system evolves from the initial condition after propagating along the effective time $\tau = Z/Z_{NL}$.

length $\xi = 1/k_0\sqrt{2\Delta n}$, corresponding to the minimal length scale for density variation in the transverse plane. The images captured by the camera in the real space detection arm offers the possibility to measure the intensity and phase (The probe beam interacts with the pump beam and the resulting interferogram is used to reconstruct the phase map) of the field directly, which access to the optical fluid density and velocity in our experiment.

Fig.6.7(a) shows typical beam images obtained for the non-interacting case ($\Delta n = 0$) with $\Delta k_\perp = 45\ mm^{-1}$. This non-interacting case is realized experimentally by setting a large detuning ($\Delta = -5$ GHz) from the $^{87}Rb\ F = 3$ to F' transition with a low laser power $P = 10\ mW$, corresponds to an effective time $Z/Z_{NL} \approx 0$. The fringes shown here look like the normal case of two beams interfering in the vacuum. The Fig.6.7(b) shows the Fourier transform of Fig.6.7(a). For the nonlinear case, we set the experimental parameters as follows, the laser detuning $\Delta = -2$ GHz from the $^{87}Rb\ F = 3$ to F' transition with a laser power $P = 500\ mW$. Under these conditions, the effective time equals $Z/Z_{NL} = 70$. We can see from fig.6.7(c) that fringes behave as snake shapes and occur lots of vortices in the meanwhile. Note that we don't change the phase image on the SLM, which means we use the same phase pattern on the SLM. The interaction of photons is the only reason this phenomenon occurs. And the relevant Fourier transform of fig.6.7(c) is showed in fig.6.7(d).

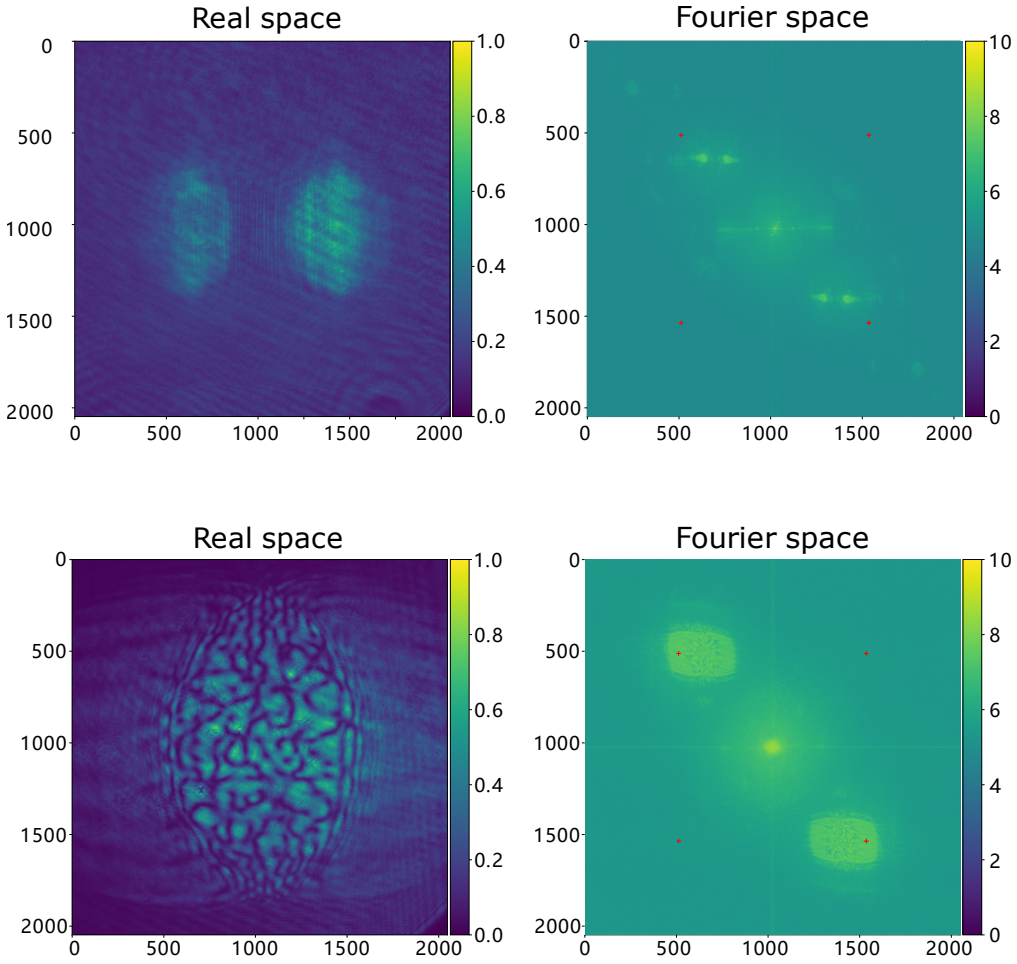

Figure 6.7: The image captured by the camera in the real space in the non-interacting case ($\Delta n = 0$) with wave vector $\Delta k_\perp = 45\ mm^{-1}$, the laser power is $P = 10\ mW$ and detuning $\Delta = -5$GHz shown in fig.(a). The corresponding Fourier transform is shown in fig.(b). In the interacting case, the laser detuning $\Delta = -2$ GHz with the laser power $P = 500\ mW$ is shown in fig.(c). And fig.(d) is the Fourier transform.

6.3.2 Evolution of the dynamics

To further study and understand how the vortices were created in our experimental setup and the generation mechanism of the turbulent state. We use a camera that captures the near field at the output of the medium for different power by progressively increasing the nonlinearity realized by changing the power of the fluids of light, thus, reducing Z_{NL}. We also reconstruct the phase map of instabilities by interfering with the emitted light with a reference beam extracted from the driving field before any modulation by the SLM. We observed the fluid evolution after different effective times at the output facet as shown in Fig.6.8. Begin with the linear case, we give a power of $P = 10\ mW$ with detuning $\Delta = -5$ GHz. In the linear regime, we observed linear straight fringes behave as two beams interfering with each other in the air. The phase map, on the other hand, is the same as the phase modulation placed on the SLM.

When the fluid power is increased to $P = 100\ mW$, the fringes begin to curve in comparison to the linear case. It is also obvious that the larger image size than in the linear case is most likely due to the nonlinear medium's defocusing effect.

When the fluid's power increased to $P = 200\ mW$, the trend of the curve of fringes in the center of the region of interest (ROI) substantially improved. Another discovery is that vertical phase jumping lines ('solitons') emerge as a result of system disorder and solitary wave that propagates without being distorted in a nonlinear and dispersive fluid at this moment.

When the fluid's power increases to $P = 300\ mW$, there are instabilities in the interference fringes caused by solitons moving at opposing velocities to each other and eventually breaking up. Certain vortices appear on the phase map in the high power zone. It is well known that dark solitons are unstable against snake instabilities and shatter into quantum vortex-antivortex pairs. When the fluid power increases to $P = 400mW$, the instabilities begin to break quickly, more vortices are generated, and the system becomes chaotic.

When the power of the fluid is increased to $P = 500mW$, we can see that more vortices are generated in the system, and they are all distributed randomly. The system is currently in a highly chaotic state. The image's interferogram, which shows phase irregularities and dislocation of fringes, also known as 'forks' in the phase map, is the typical signature of vortices. The phase shift of the quantum vortices indicated by the orange circle is clearly visible. It is formed when solitons decay into vortex anti-vortex pairs with opposing circulation.

Remarks on the observation

- Turbulence is a phenomenon that occurs when the kinetic energy of a flowing fluid becomes too large compared to the viscous forces. The excess energy will then be dissipated by the system via the generation of vortex pairs.
- At low power, snake instabilities do not have the necessary evolution time to break into

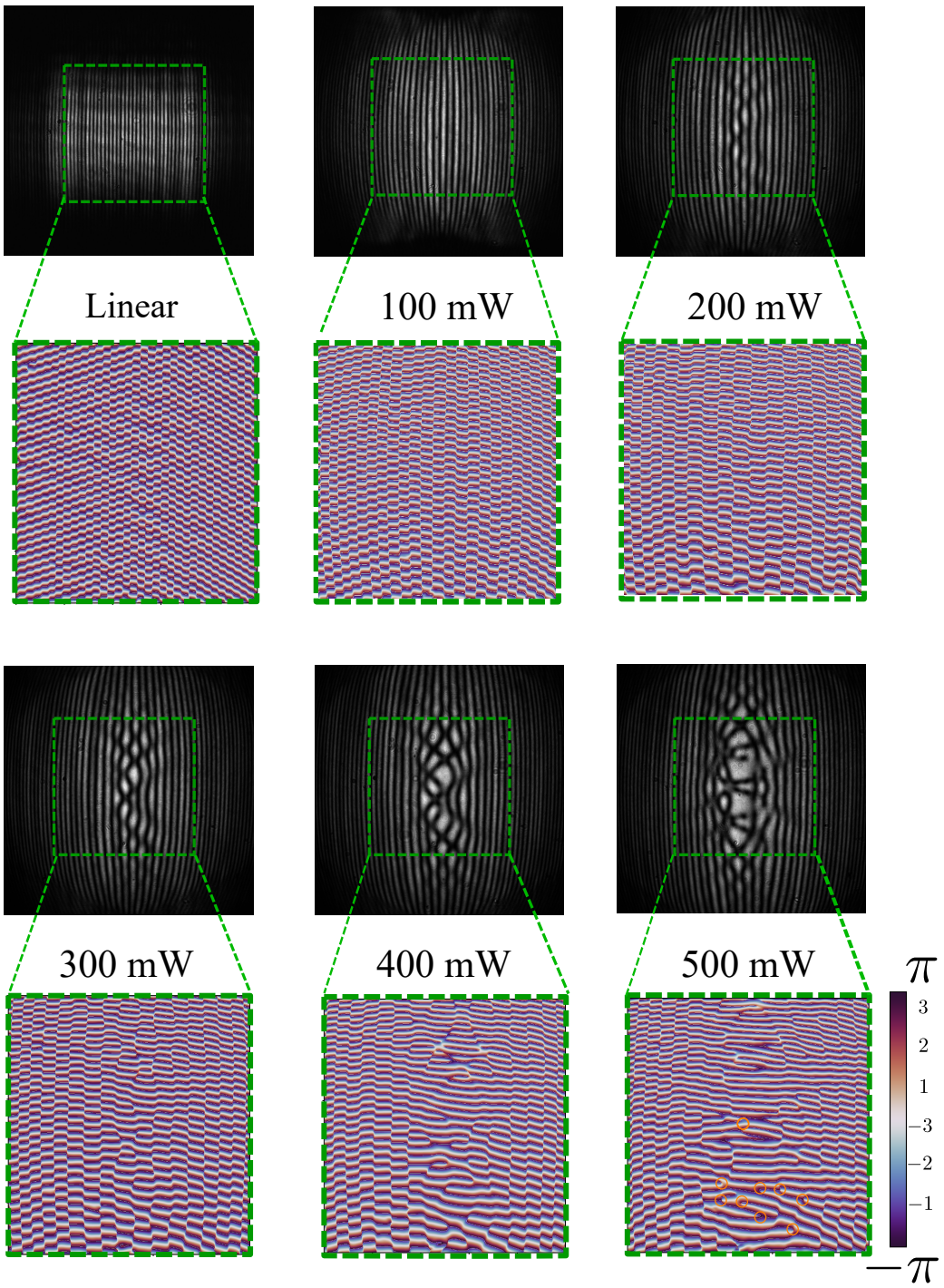

Figure 6.8: Experimental images of the density from the camera and the relevant region of interest (green dashed region) phase map. Each image is taken with different power, from 10 mW to 500 mW at a step of 100 mW. Experimental parameters as follows: Detuning $\Delta = -2\ GHz$, $k_\perp = 17.5\ mm^{-1}$ and cell temperature stabled at $105°C$ with transmission $Tr = 4\%$.

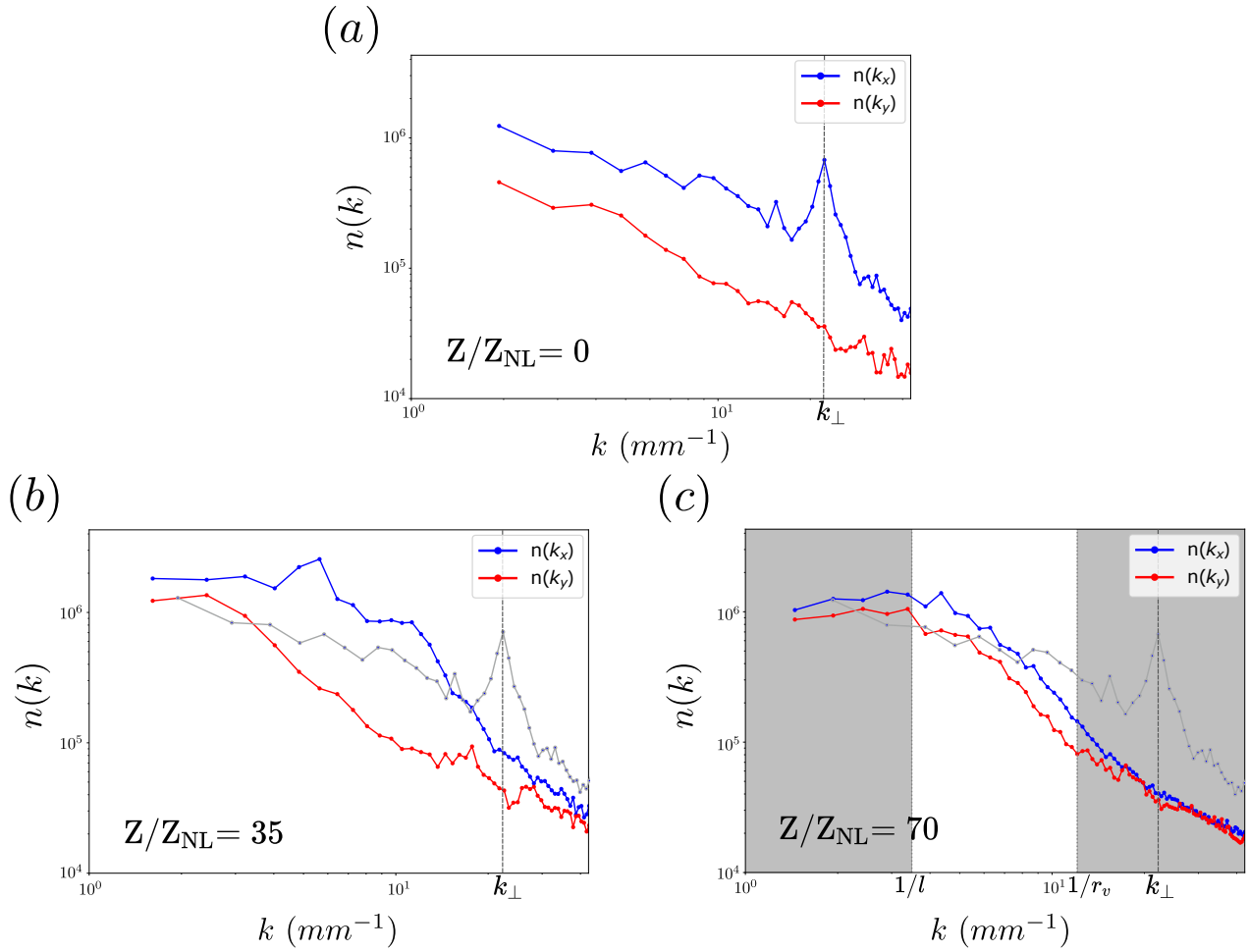

Figure 6.9: Density profile along k_x in blue solid curve and along k_y in red solid curve for the different effective time. (**a**). In the non-interacting photon case, we use the grey dashed line label the $k_\perp = 22.5\ mm^{-1}$ value of peaks occurs in the blue curve. This value is exactly correspond to the value imposed on the SLM. We also plot this curve at (**b**). The effective time $Z/Z_{NL} = 35$ and (**c**). The effective time $Z/Z_{NL} = 70$ for a clear comparison.

too many vortices. An increase of Mach number β accelerates the snake instability growth and leads to vortex nucleation. The snake instability always leads to breaking up into a pair of oppositely charged vortices to conserve the total topological charge of the system to zero.

6.3.3 Isotropic behavior

To study the turbulence, we investigate how the density distribution in the momentum space evolves line-integrated distributions parallel $n(k_x)$ and perpendicular $n(k_y)$ to the drive in the linear and nonlinear regime.

We took 20 images for 3 different effective times ($Z/Z_{NL} = 0$, $Z/Z_{NL} = 35$, $Z/Z_{NL} = 70$) under

the same experimental conditions except for adding random noise. The initial state ($\tau = 0$) corresponds to the linear regime and is obtained by setting a large detuning ($\Delta = -5$ GHz) and low laser power ($P = 10$ mW). Longer effective times ($\tau = 35, 70$) are obtained by setting the detuning closer to resonance and a higher power. Then we perform a Fourier analysis to gain access to the density profile in Fourier space $n(k)$ long the k_x and k_y. Each configuration is averaged over 20 images obtained by adding random noise to the input plane of the nonlinear medium.

At the initial state ($\tau = 0$), due to the angle imposed between the two fluids by the SLM modulation, a clear modulation (the vertical grey line) at the forcing length-scale $k_f \approx 22.5\ mm^{-1}$ is visible along k_x. This initial state reflects anisotropic forcing on a short time scale. The grey curve plotted at $\tau = 35$ and $\tau = 70$ is the density profile along k_x of the non-interacting case multiplied by the power difference ratio. We see a clear reduction in the forcing peak as the effective time increases, but the density spectrum remains anisotropic at short effective times ($\tau < 70$). A quasi-isotropic behaviour between the profile along k_x and k_y emerges at $\tau = 70$. The emergency of isotropy is seen in the convergence of two curves for $k > k_\perp = 22.5\ mm^{-1}$. So we can say that beyond a sufficiently large effective time, the cascade is statistically isotropic. While at low k, their distribution is anisotropic. This result agreement with a recent finding in ultra-cold atomic gases about the emergence of statistical isotropy under anisotropic forcing [108].

6.3.4 Velocity

We can directly extract the total velocity of the system $\boldsymbol{v^{tot}(r)} \propto \nabla_\perp \theta(\boldsymbol{r})$ from the phase map of the fluid in fig. 6.8 as we can direct access to the fluid's phase. This is also one of the advantages of the fluid of light compared to atomic gas. To disentangle the velocity into its incompressible and compressible parts, we adopt the Helmholtz decomposition for vector fields from the density-weighted velocity, given by $\boldsymbol{u^{tot}(r)} = \sqrt{\rho(\mathbf{r})}\boldsymbol{v^{tot}(r)}$, where $\rho(\mathbf{r})$ is the light intensity. Given $\boldsymbol{v^{tot}(r)}$, we can write it as the sum of a potential and a divergence-free contribution:

$$\boldsymbol{u^{tot}(r)} = \boldsymbol{\nabla}\phi(\boldsymbol{r}) + \nabla \times \boldsymbol{A}(\boldsymbol{r}) \tag{6.19}$$

where ϕ and $\boldsymbol{A}$ are a scalar and a vector field, respectively. In the Fourier space, the decomposition has a straightforward implementation. Indeed, given the vector field in real space $\boldsymbol{v(x)}$:

$$\boldsymbol{U(k)} = \frac{1}{2\pi} \int e^{-i\boldsymbol{kx}} \boldsymbol{v(x)} dS_x \tag{6.20}$$

Which can be decomposed as Fourier space:

$$\boldsymbol{U(k)} = i\boldsymbol{k}U_\phi(\boldsymbol{k}) + i\boldsymbol{k} \times \boldsymbol{U_A(k)} \tag{6.21}$$

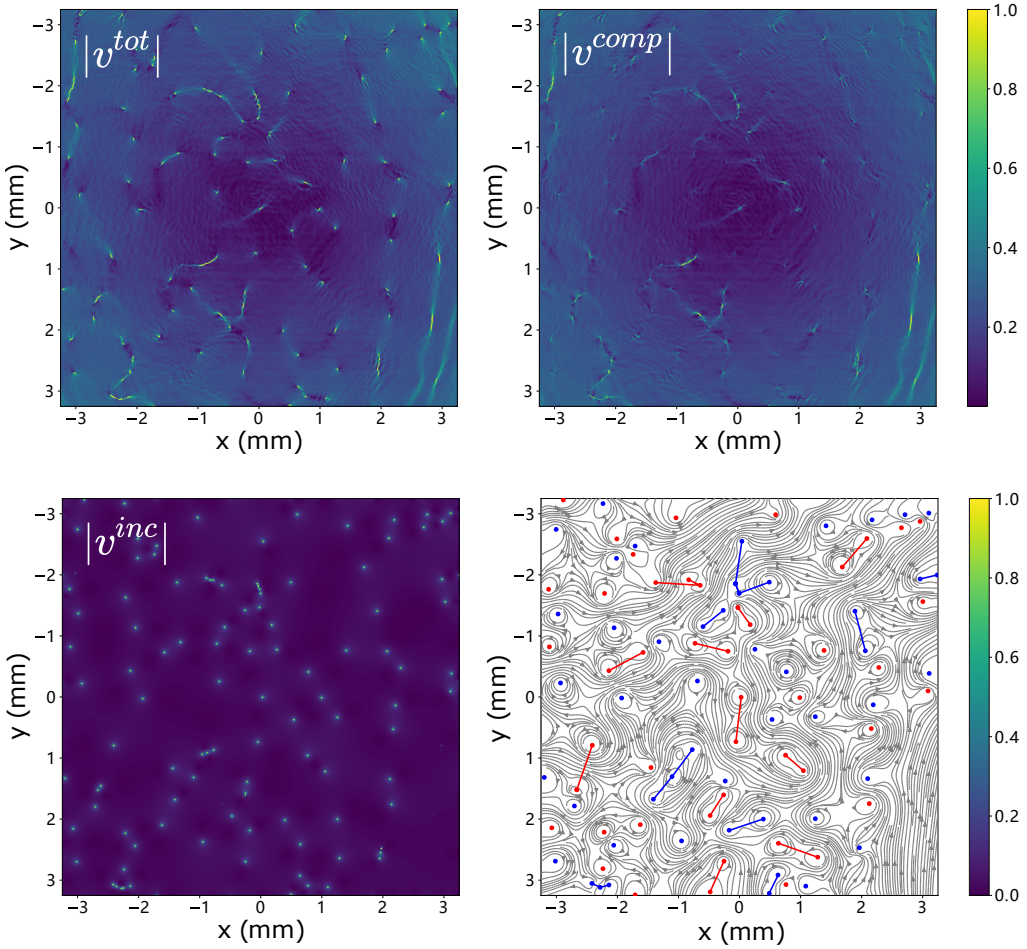

Figure 6.10: Velocity field decomposition in the region of interest(ROI). (**a**). The module of total velocity. (**b**). The module of compressible velocity. (c). The module of incompressible velocity. (d). Circulation distribution of the vortices in (**c**). The red and blue dots represent the position of the positive and negative vortices linked by solid lines if they belong to the same cluster. The classification of the vortices is based on their signs and positions: vortices (antivortices) are indicated by red(blue) points; clusters by lines of the same color. Streamlines of the computed flow are shown in gray.

Where we used the scalar and vector fields:

$$U_\phi(\boldsymbol{k}) = -i\frac{\boldsymbol{k}\cdot\boldsymbol{U}(\boldsymbol{k})}{||\boldsymbol{U}(\boldsymbol{k})||^2} \tag{6.22}$$

$$\boldsymbol{U_A}(\boldsymbol{k}) = i\frac{\boldsymbol{k}\times\boldsymbol{U}(\boldsymbol{k})}{||\boldsymbol{U}(\boldsymbol{k})||^2} \tag{6.23}$$

Once we calculated these in the Fourier space, back to the real space we have:

$$\nabla\phi(\boldsymbol{x}) = \int e^{i\boldsymbol{k}\cdot\boldsymbol{x}} i\boldsymbol{k}U_\phi(\boldsymbol{k})dS_k \tag{6.24}$$

$$\nabla\times\boldsymbol{A}(\boldsymbol{x}) = \int e^{i\boldsymbol{k}\cdot\boldsymbol{x}} i\boldsymbol{k}\times\boldsymbol{U_A}(\boldsymbol{k})dS_k \tag{6.25}$$

After decomposing the velocity into the compressible and incompressible parts of the fluid, which allows to separate the divergent (incompressible) and irrational (compressible) part of the superfluid velocity, associated with the vortex distribution and the sound waves, respectively. Therefore, it is possible to remove the contribution of the acoustic waves as shown in fig.6.10 (b). The module of the incompressible velocity $|\boldsymbol{U}^{inc}|$ is shown in fig.6.10 (c). The bright points in fig.6.10 (c) correspond to singularities in the turbulent state phase. And the incompressible velocity field can be used as a tool to compare the information on the kinetic energy with the vortex classification analysis.

Moreover, it provides possibilities for us to study the direction of the rotation of each vortex with its position and then apply the vortex classification algorithm by calculating the vorticity of the system, given by $\nabla\boldsymbol{v}^{tot}$. In the tracking and classification analysis, we consider only those vortices with cores separated by a distance larger than the healing length ξ.

We used a vortex classification algorithm[109, 110] to identify vortices as clusters, dipole, pairs, or free vortices. Sign of topological charges is conventionally defined depending on the wind direction as follows: + for anti-clockwise (blue) and − for clockwise (red) velocity. Each pair is composed of the same charged vortices. Any two like-sign vortices are said to belong to the same cluster if they are closer to one another than either is to an opposite-sign vortex. Because the vortices are quantized, the spatial clustering of like-sign vortices forms the equivalent of classical large-scale flows. A vortex–antivortex pair is defined as a dipole if they are mutual nearest neighbors. Free vortices are those that are left over after all clusters and dipoles have been assigned. For experimental results, please refer to fig.6.10(d).

6.3.5 Vortex spectra

Decomposing the condensate kinetic energy into compressible and incompressible parts is a useful technique, which allows us to analyze how kinetic energy distributed over length scales due to vortex lines and sound.

in order to explore the role of the vortex in exhibiting the energy cascade, we utilize this optical imprinting method by accurately shaping the beam with a Spatial Light Modulator. which allows us to generate an on-demand vortex on a photon fluid. For example, we can design the position and number of vortices. In the previous section, we explained that it offers opportunities for us to calculate the incompressible part of the velocity field from the phase measurement. We can define the density-weighted velocity field given by $\mathbf{u}(\mathbf{r})^{inc} = \sqrt{n(\mathbf{r})}\boldsymbol{v}(\boldsymbol{r})^{inc}$. The incompressible energy can be expressed by analyzing the Fourier space [111, 99]:

$$E_{kin}^{inc} = \frac{m}{2} k \sum_{i=x,y} \int_0^{2\pi} |U_i^{inc}(\mathbf{k})|^2 d\theta \tag{6.26}$$

with $\mathbf{U}^{inc}(\mathbf{k}) = TF[\mathbf{u}(\mathbf{r})^{inc}]$.

With the incompressible density-weighted velocity field, we present the streamlines and incompressible density-weighted velocity field and compute the incompressible kinetic energy spectrum. The experimental incompressible energy spectra for several initial states are presented in Fig.6.11. Firstly we have investigated the kinetic energy spectrum from a single vortex and dipole vortices (opposite sign) by direct imprinting with the SLM. For a single vortex without acoustic energy, the field is automatically incompressible [112]. The spectrum of a single vortex state shows a $E_{kin}^{inc} \propto k^{-1}$ decay in the infrared (IR) range ($k\xi \ll 1$) which arises purely from the irrotational velocity field of a quantum vortex. The scaling is similar to point-like vortices and is the only remaining sign of the vortex far from its core. However, in contrast with the point-like model, in the ultraviolet (UV) range ($k\xi \gg 1$), we observe a $E_{kin}^{inc} \propto k^{-3}$ decay which stems from the internal structure of the vortex core as described theoretically in [113].

Because the vortex core structure remains unchanged, the UV scaling for the dipole spectra remains unchanged. For the dipole spectrum, a $E_{kin}^{inc} \propto k^1$ IR-scaling is observed, which results from the cancellation of the velocity field for length scales much larger than typical inter-vortex separation in any neutral configuration of vortices [112]. As expected, the UV scaling remains identical for the dipole spectra since the vortex core structure is not modified. For the dipole spectrum, a $E_{kin}^{inc} \propto k^1$ IR-scaling is observed for the dipole configuration, which originates from the cancellation of the velocity field for length scales much larger than typical inter-vortex separation in any neutral configuration of vortices [112].

6.3.6 Energy spectrum

2D turbulence is quite different from turbulence in three-dimensional (3D) classical fluids and is connected with an energy cascade from large-length scales specified by the features of an energy-forcing mechanism to short-length scales where viscous damping reduces the fluid's kinetic energy. The inertial range of energy flux is defined by this range of length scales and the

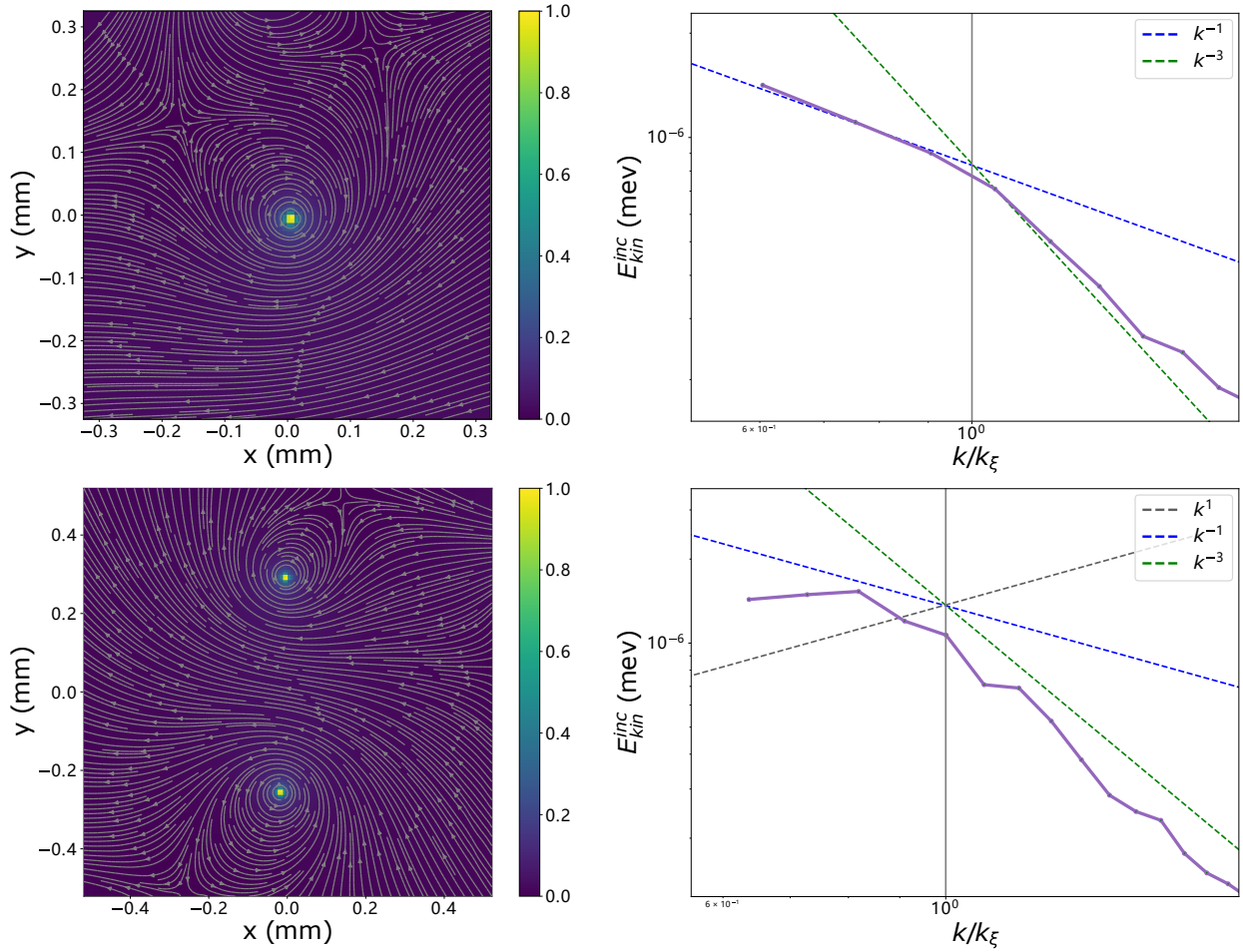

Figure 6.11: (**a**). Module and streamlines of the incompressible velocity field from a single vortex. (**b**). The kinetic energy spectra corresponding to (**a**) is shown in the purple curve. The blue and the green dashed lines are the fitting curves k^{-1} and k^{-3}. (**c**) Module and streamlines of the incompressible velocity field from a pair of vortices. (**d**). The purple curve shows the kinetic energy spectra corresponding to the vertex/antivortex dipole. The grey dashed curve stands for k^1 fitting curve besides the same meaning for the blue and green dashed lines.

range of related wave numbers k. Kolmogorov demonstrated that the energy cascade corresponds to a kinetic-energy spectrum corresponding to $k^{-5/3}$ in the inertial range [83].

Although the results of some theoretical and experimental simulations have proved that there is an inverse energy cascade in the two-dimensional turbulent flow of quantum fluids. However, a question still unsolved in quantum turbulence is the experimental demonstration of an inverse energy cascade. We calculate the incompressible energy spectrum from the region of interest (ROI) in Fig. 6.8 for a turbulent state. The spectrum is averaged over 20 images, adding a random noise on the input of the nonlinear medium. And the result showed in Fig.6.12, an inertial range appears 1 and k_l/k_ξ, the energy spectrum is displayed for a range of wavevectors that spans from the healing length (solid vertical grey line) of the medium to wave-vector associated to $l \approx 3-4\xi$ the size of the cluster, showed by the solid vertical green line. Due to the fact that the vortex structure doesn't change in this turbulent state, we still observe the k^{-3} in the UV range. However, this configuration can be considered as several dipoles composed, so we can observe k^1 IR-scaling appears as same as what we have seen in the dipole vortices. Importantly, a spectral range between these two limits with different scaling is also clearly visible. In the momentum range between the inverse of the mean vortex cluster radius and the inverse of the healing length, the kinetic energy spectrum decays as $k^{-5/3}$, which is in perfect agreement with the Kolmogorov exponent predicted for the inverse energy cascade mechanism.

6.3.7 C_2 and C_4

We also explore the number of vortices as a function of effective time. The result is shown in Fig.6.13(a). With the increase of the effective time, we could observe more vortices. The number of vortices shows an exponential growth trend. We then study the vortex interaction based on the vortex algorithm by exploring the correlation between them [114]. For N vortices the correlation C_d is given by: The 2nd and 4th-order nearest-neighbor correlation functions C_2 and C_4 are also calculated (left panel). Those are defined by:

$$C_d = \sum_{i=1}^{N} \sum_{j=1}^{d} c_{ij}/dN \tag{6.27}$$

where $c_{ij} = 1$ if vortex i and its jth nearest neighbor have the same sign, and $c_{ij} = 0$ if they have opposite sign. For both C_d, the points never exceed the bar of 0.5, representing what is expected for a random distribution of vortices, and remain between 0.3 and 0.5. In agreement with [114], this allows us to determine that our clustering occurs in regions that are spatially independent since for a configuration dominated by dipoles (clusters), the sign of C_2 and C_4 should constant [111].

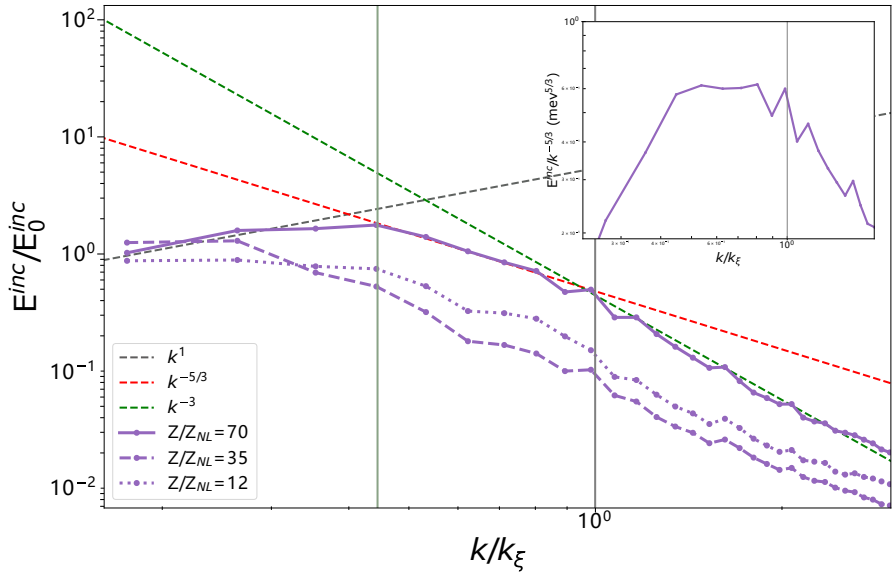

Figure 6.12: Incompressible kinetic energy spectra measured on all vortices in the center region of interest(ROI), for $Z/Z_{NL} = 0$ (purple chain line), $Z/Z_{NL} = 35$ (purple dashed line) and $Z/Z_{NL} = 70$ (solid purple line). The grey, red, and green dashed lines are power-law functions plotted respectively for k^1, $k^{-5/3}$, and k^{-3}. The crossover scale $k/k_\xi = 1$ is given by the solid grey vertical line. The solid green vertical line represents the start of the inertial range set at k_l/k_ξ.

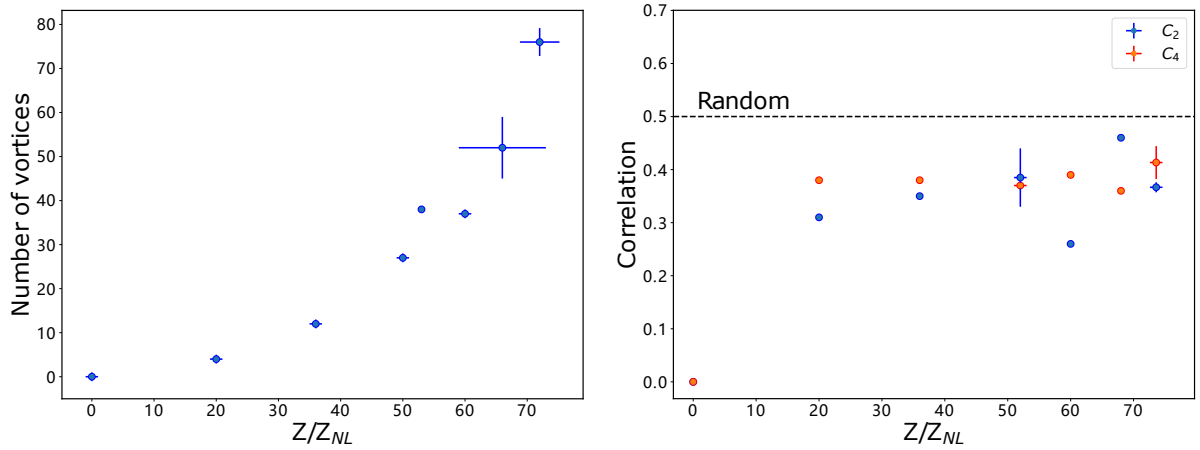

Figure 6.13: (**a**). Total number of vortices was measured by tuning the effective time. (**b**). C_2 and C_4 vortex correlation represented by the blue and red dots, respectively. The horizontal dashed line is the expected correlation for a random distribution of vortices.

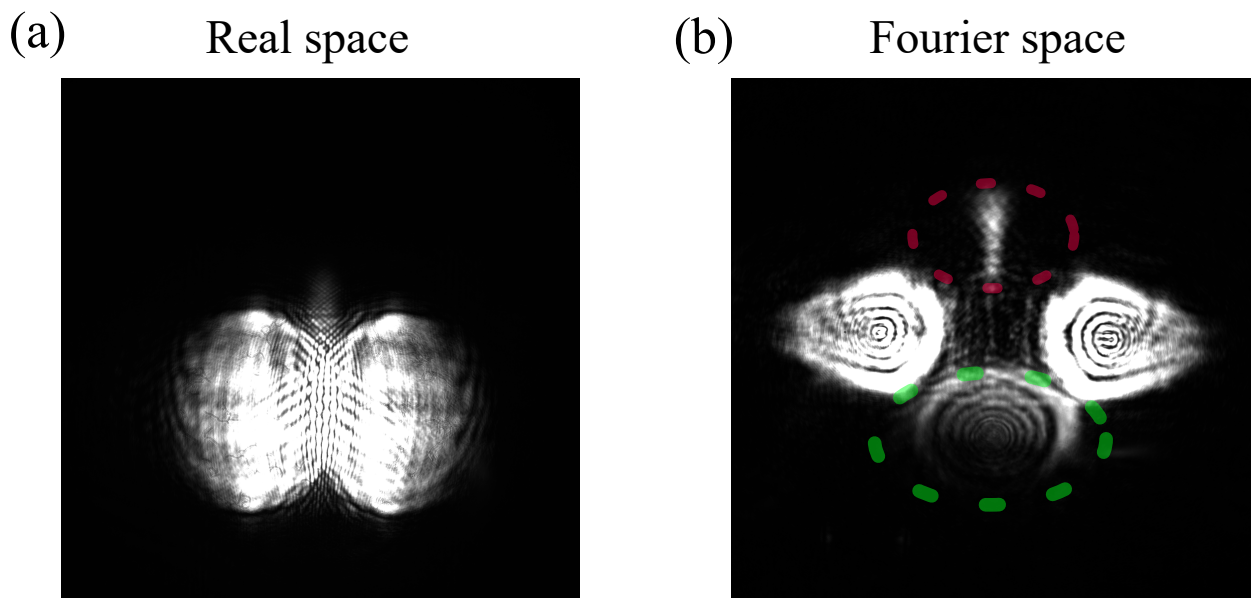

Figure 6.14: Image when a probe beam interferes with the fluid in the real space and Fourier space.

6.3.8 Explore the energy transfer

As previously stated, an unstable region exists where the imaginary part of the Bogoliubov dispersion relation is positive, which is caused by excess energy in the turbulent state. To show that turbulence is generated in our fluid of light system, we designed an experiment in which a probe beam $k_{pr}sin\theta$ interacts with a turbulent region of the fluid of light, where k_{pr} is the probe beam's wavenumber and θ is the angle between the probe beam and the signal. If there is a transfer of energy from the turbulent flow to the probe light, or if the probe light gains energy, this indicates that the system is in a turbulent state.

The energy of the probe beam is measured by directing it to a spectrum analyzer or oscilloscope. However, the low transmission of the rubidium cell under the experimental conditions of our system's turbulent state makes measurement difficult. On the other hand, the laser source's limited maximum output power prevents us from providing more power to the probe path. As a result of the experimental results, we did not see energy peaks at specific wave numbers $k_{\perp}$. This inspired us to change our plan and use the camera to see if we could spot a conjugate beam on the other side of the photon fluid. The experimental results are shown in Fig.6.14. The probe beam is represented by the bottom green dashed circle, and the conjugate is represented by the top red dashed circle. This exciting phenomenon confirms that photon fluid is an excellent platform to generate quantum turbulence.

6.4 Conclusion

Our results demonstrate the potential of photon fluid for experimental studies of quantum turbulence. The fluid's velocity and density access to fluid density and phase can be finely controlled by optical means. We have demonstrated that quantum turbulence in a 2D paraxial fluid of light starting with an anisotropic forcing will become isotropic. We reported the incompressible kinetic energy spectrum in 1, 2, and N vortices configurations by extracting the incompressible density-weighted velocity using the Helmholtz decomposition. The most striking finding is the observation of a $k^{-5/3}$ scaled Kolmogorov spectrum for an inverse energy cascade in a superfluid. This is the first direct experimental signature of a flux of kinetic energy from small to large length scales in a quantum fluid of light. And this configuration offers the opportunity to probe more complex phenomena. The new experimental scheme's flexibility and ease of control pave the way for research into the out-of-equilibrium physics of quantum fluids.

.

General conclusion and outlooks

This thesis manuscript's primary goal was to investigate several hydrodynamic properties of a photon fluid passing through hot rubidium vapors. While photons do not interact in a vacuum, the situation will change when an intense laser is adjusted near an atomic resonance within a hot rubidium vapor cell. The dynamics of the electric field in a nonlinear medium are described by the nonlinear Schrödinger equation, which can be mapped to the Gross-Pitaevskii equation, which explains the space-time evolution of atomic Bose-Einstein condensates under the mean-field approximation. As a result of this analogy, interact photons behave like a fluid flowing in a plane perpendicular to the optical axis. Those systems exhibit, in particular, the ability of superfluity without dissipating energy. Therefore, it is an excellent platform to investigate the many-body problem and the hydrodynamic behavior of the superfluid.

Chapter 1 deduces the nonlinear Schrödinger equation. The relationship with the Gross Pitaevskii equation is established and thoroughly investigated. Following that, the dynamics of tiny amplitude density waves moving onto the photon fluid are described. Using the Bogoliubov transform, we show that those waves obey the Bogoliubov dispersion relation, which has two distinct regimes. It starts linearly for low excitation wave vectors, when density waves behave as collective phonons all moving at the same speed (the sound velocity), before gaining a quadratic tendency, which is characteristic of particle-like dispersion. I also introduce how to know a fluid belongs to the superfluid. The presence of the sound speed, according to the Landau criteria for superfluidity, would ensure the detection of superfluid light flows in our system.

In Chapter 2, I present some necessary knowledge on our system to create the photon fluid. Start with the introduction of the rubidium structure and the heating mechanism of the nonlinear medium. I also discuss some important factors that should take into account when a laser beam passes through a hot vapor cell. Furthermore, a substantial portion of this chapter is devoted to presenting our method for calculating the nonlinear refractive index Δn by measuring the spatial changes of the nonlinear phase shift accumulated by the beam.

In chapter 3, we report the working principle of several experimental tools used to create and characterize a photon fluid. I first briefly present how the laser sources work. Then the attention turns to describing the Spatial Light modulator (SLM), which imprints a special phase

to the laser beam so as to modulate the properties of photon fluid through the liquid crystal. The acousto-optic modulator (AOM) used to diffract and shift the frequency of light using sound waves is also presented. Finally, some technical details about the glass cells containing rubidium vapor and the homemade heating system designed to control its temperature are introduced.

In chapter 4, we implement Bragg-like spectroscopy in a paraxial fluid of light by imprinting analogues of short Bragg pulses on the photon fluid using wavefront shaping with a spatial light modulator. We provide a static structure factor measurement and observe a decrease in small wave vector variations. This conclusion is in great accord with the Femann relation, which indirectly reveals the presence of pair-correlated particles in the photon fluid. We also get the Bogoliubov dispersion, which describes small amplitude density fluctuations traveling onto the fluid of light. And the relation shows a linear phononic domain for photons with weak interactions and low sound velocity. This work opens the way to the measurement of Tan's contact [115] and the observation of beyond mean field effects in photon fluids.

In chapter 5, by sending a near-resonant laser pulse propagating in a warm atomic vapor cell, I introduce the analogue of cosmological particle creation in the quantum fluid of light. When photons cross the front and back faces of the nonlinear medium, they encounter a pair of abrupt jumps in the interaction parameter, which can be translated into quantum quenches. The emission of pairs of correlated counter-propagating Bogoliubov phonons results in unusual characteristics in the intensity distribution and the near- and far-field two-body correlation functions in the weak-nonlinearity regime. We see acoustic peaks in the density power spectrum, known as Sakharov oscillating, which is usually discussed in the context of universe evolution, and cosmic microwave background anisotropy is the manifestation of interfering acoustic waves in an ideal fluid. Our experiments show that vacuum fluctuations in these two quench processes produce analogous cosmological particles.

In chapter 6, I introduced some basic concepts and properties of classical turbulence and quantum turbulence. We want to utilize two counter-propagating fluids of light that interfere with each other in hot atomic vapors to investigate the existence of the inertial range where kinetic energy is transferred from small to large lengths in two dimensions of quantum turbulence. We first explore the instability evolution process from the quantum soliton and quantum vortices to the completely disordered quantum turbulence by varying the Mach number. Meanwhile, we decompose the velocity into the compressible and incompressible parts associated with the sound waves and the vortex distribution from the phase of fluid by the Helmholtz decomposition method. Then, we analyze the energy spectrum of incompressible flow and find energy cascade $E(k) \propto k^{-5/3}$ agrees with Kolmogorov's prediction in the inertial range. This is the first direct experimental evidence of inverse energy cascade in 2D quantum fluid. Moreover, we study the density distribution $n(k_x)$ and $n(k_y)$ in the momentum space for different effective propagation times. We find the system begin with an anisotropic state and ends up with an

isotropic state. To demonstrate the energy transfer from the streaming flow to the elementary (Bogoliubov) excitations, we use a probe beam to interfere with the photon fluid. A conjugate beam appears on the symmetrical side of the probe beam. Our experiments demonstrate the great potential of photon fluid for studying quantum turbulence. This novel platform opens exciting possibilities for studying non-equilibrium turbulence dynamics in reduced dimensions with a controlled forcing mechanism and a homogeneous density.

Bibliography

[1] F.A. Staas, A.P. Severijns, and H.C.M. Van der Waerden. A dilution refrigerator with superfluid injection. *Physics Letters A*, 53(4):327–328, 1975.

[2] Tomonori Ohba. Limited quantum helium transportation through nano-channels by quantum fluctuation. *Scientific Reports*, 6(1):28992, Jul 2016.

[3] G. B. Hess and W. M. Fairbank. Measurements of angular momentum in superfluid helium. *Phys. Rev. Lett.*, 19:216–218, Jul 1967.

[4] J. F. ALLEN and A. D. MISENER. Flow of liquid helium ii. *Nature*, 141(3558):75–75, Jan 1938.

[5] P. Kapitza. Viscosity of liquid helium below the λ-point. *Nature*, 141(3558):74–74, Jan 1938.

[6] L. Pitaevskii and S. Stringari. *Bose-Einstein Condensation*. Oxford University Press, London, 2003.

[7] Oliver Penrose and Lars Onsager. Bose-einstein condensation and liquid helium. *Phys. Rev.*, 104:576–584, Nov 1956.

[8] Mike H Anderson, Jason R Ensher, Michael R Matthews, Carl E Wieman, and Eric A Cornell. Observation of bose-einstein condensation in a dilute atomic vapor. *science*, 269(5221):198–201, 1995.

[9] Kendall B Davis, M-O Mewes, Michael R Andrews, Nicolaas J van Druten, Dallin S Durfee, DM Kurn, and Wolfgang Ketterle. Bose-einstein condensation in a gas of sodium atoms. *Physical review letters*, 75(22):3969, 1995.

[10] Cl C Bradley, CA Sackett, JJ Tollett, and Randall G Hulet. Evidence of bose-einstein condensation in an atomic gas with attractive interactions. *Physical review letters*, 75(9):1687, 1995.

[11] D. Pines. *Theory Of Quantum Liquids: Normal Fermi Liquids*. CRC Press, 2018.

[12] Iacopo Carusotto and Cristiano Ciuti. Quantum fluids of light. *Rev. Mod. Phys.*, 85:299–366, Feb 2013.

[13] Iacopo Carusotto. Superfluid light in bulk nonlinear media. *Proceedings of the Royal Society A: Mathematical, Physical and Engineering Sciences*, 470(2169):20140320, 2014.

[14] Claude Weisbuch, Mr Nishioka, A Ishikawa, and Y Arakawa. Observation of the coupled exciton-photon mode splitting in a semiconductor quantum microcavity. *Physical Review Letters*, 69(23):3314, 1992.

[15] Jacek Kasprzak, Murielle Richard, S Kundermann, A Baas, P Jeambrun, Jonathan Mark James Keeling, FM Marchetti, MH Szymańska, R André, JL Staehli, et al. Bose–einstein condensation of exciton polaritons. *Nature*, 443(7110):409–414, 2006.

[16] S Christopoulos, G Baldassarri Höger Von Högersthal, AJD Grundy, PG Lagoudakis, AV Kavokin, JJ Baumberg, G Christmann, R Butté, E Feltin, J-F Carlin, et al. Room-temperature polariton lasing in semiconductor microcavities. *Physical review letters*, 98(12):126405, 2007.

[17] Alberto Amo, Jérôme Lefrère, Simon Pigeon, Claire Adrados, Cristiano Ciuti, Iacopo Carusotto, Romuald Houdré, Elisabeth Giacobino, and Alberto Bramati. Superfluidity of polaritons in semiconductor microcavities. *Nature Physics*, 5(11):805–810, Nov 2009.

[18] A. Amo, S. Pigeon, D. Sanvitto, V. G. Sala, R. Hivet, I. Carusotto, F. Pisanello, G. Leménager, R. Houdré, E Giacobino, C. Ciuti, and A. Bramati. Polariton superfluids reveal quantum hydrodynamic solitons. *Science*, 332(6034):1167–1170, 2011.

[19] K. G. Lagoudakis, M. Wouters, M. Richard, A. Baas, I. Carusotto, R. André, Le Si Dang, and B. Deveaud-Plédran. Quantized vortices in an exciton–polariton condensate. *Nature Physics*, 4(9):706–710, Sep 2008.

[20] D. Sanvitto, S. Pigeon, A. Amo, D. Ballarini, M. De Giorgi, I. Carusotto, R. Hivet, F. Pisanello, V. G. Sala, P. S. S. Guimaraes, R. Houdré, E. Giacobino, C. Ciuti, A. Bramati, and G. Gigli. All-optical control of the quantum flow of a polariton condensate. *Nature Photonics*, 5(10):610–614, Oct 2011.

[21] Gaël Nardin, Gabriele Grosso, Yoan Léger, Barbara Pitka, François Morier-Genoud, and Benoît Deveaud-Plédran. Hydrodynamic nucleation of quantized vortex pairs in a polariton quantum fluid. *Nature Physics*, 7(8):635–641, Aug 2011.

[22] Giovanni Lerario, Antonio Fieramosca, Fábio Barachati, Dario Ballarini, Konstantinos S Daskalakis, Lorenzo Dominici, Milena De Giorgi, Stefan A Maier, Giuseppe Gigli, Stéphane Kéna-Cohen, et al. Room-temperature superfluidity in a polariton condensate. *Nature Physics*, 13(9):837–841, 2017.

[23] Robert W. Boyd. *Nonlinear Optics, Third Edition*. Academic Press, Inc., USA, 3rd edition, 2008.

[24] Raymond Y. Chiao and Jack Boyce. Bogoliubov dispersion relation and the possibility of superfluidity for weakly interacting photons in a two-dimensional photon fluid. *Phys. Rev. A*, 60:4114–4121, Nov 1999.

[25] Maria Chiara Braidotti, Radivoje Prizia, Calum Maitland, Francesco Marino, Angus Prain, Ilya Starshynov, Niclas Westerberg, Ewan M. Wright, and Daniele Faccio. Measurement of penrose superradiance in a photon superfluid. *Phys. Rev. Lett.*, 128:013901, Jan 2022.

[26] G. Xu, D. Vocke, D. Faccio, J. Garnier, T. Roger, S. Trillo, and A. Picozzi. From coherent shocklets to giant collective incoherent shock waves in nonlocal turbulent flows. *Nature Communications*, 6(1):8131, Sep 2015.

[27] A. Eloy, O. Boughdad, M. Albert, P.-É. Larré, F. Mortessagne, M. Bellec, and C. Michel. Experimental observation of turbulent coherent structures in a superfluid of light sup(a)/sup. *Europhysics Letters*, 134(2):26001, apr 2021.

[28] Shu Jia, Mikko Haataja, and Jason W Fleischer. Rayleigh–taylor instability in nonlinear schrödinger flow. *New Journal of Physics*, 14(7):075009, jul 2012.

[29] M. Abuzarli, T. Bienaimé, E. Giacobino, A. Bramati, and Q. Glorieux. Blast waves in a paraxial fluid of light sup(a)/sup. *Europhysics Letters*, 134(2):24001, apr 2021.

[30] Jeff Steinhauer, Murad Abuzarli, Tangui Aladjidi, Tom Bienaimé, Clara Piekarski, Wei Liu, Elisabeth Giacobino, Alberto Bramati, and Quentin Glorieux. Analogue cosmological particle creation in an ultracold quantum fluid of light. *Nature Communications*, 13(1):1–7, 2022.

[31] Neven Šantić, Adrien Fusaro, Sabeur Salem, Josselin Garnier, Antonio Picozzi, and Robin Kaiser. Nonequilibrium precondensation of classical waves in two dimensions propagating through atomic vapors. *Phys. Rev. Lett.*, 120:055301, Feb 2018.

[32] Pierre-Élie Larré and Iacopo Carusotto. Propagation of a quantum fluid of light in a cavityless nonlinear optical medium: General theory and response to quantum quenches. *Phys. Rev. A*, 92:043802, Oct 2015.

[33] Tangui Aladjidi, Murad Abuzarli, Guillaume Brochier, Tom Bienaimé, Thomas Picot, Alberto Bramati, and Quentin Glorieux. Transit effects for non-linear index measurement in hot atomic vapors, 2022.

[34] Clara Piekarski, Wei Liu, Jeff Steinhauer, Elisabeth Giacobino, Alberto Bramati, and Quentin Glorieux. Measurement of the static structure factor in a paraxial fluid of light using bragg-like spectroscopy. *Phys. Rev. Lett.*, 127:023401, Jul 2021.

[35] Quentin Glorieux. *Quantum Optics in Dense Atomic Media: From Optical Memories to Fluids of Light*. Habilitation à diriger des recherches, Sorbonne Université, December 2018.

[36] Q. Fontaine, T. Bienaimé, S. Pigeon, E. Giacobino, A. Bramati, and Q. Glorieux. Observation of the bogoliubov dispersion in a fluid of light. *Phys. Rev. Lett.*, 121:183604, Oct 2018.

[37] Claire Michel, Omar Boughdad, Mathias Albert, Pierre-Élie Larré, and Matthieu Bellec. Superfluid motion and drag-force cancellation in a fluid of light. *Nature Communications*, 9(1):2108, May 2018.

[38] David Vocke, Kali Wilson, Francesco Marino, Iacopo Carusotto, Ewan M. Wright, Thomas Roger, Brian P. Anderson, Patrik Öhberg, and Daniele Faccio. Role of geometry in the superfluid flow of nonlocal photon fluids. *Phys. Rev. A*, 94:013849, Jul 2016.

[39] Guohai Situ and Jason W. Fleischer. Dynamics of the berezinskii–kosterlitz–thouless transition in a photon fluid. *Nature Photonics*, 14(8):517–522, Aug 2020.

[40] Pierre Azam, Adrien Fusaro, Quentin Fontaine, Josselin Garnier, Alberto Bramati, Antonio Picozzi, Robin Kaiser, Quentin Glorieux, and Tom Bienaimé. Dissipation-enhanced collapse singularity of a nonlocal fluid of light in a hot atomic vapor. *Phys. Rev. A*, 104:013515, Jul 2021.

[41] T. Bienaimé, M. Isoard, Q. Fontaine, A. Bramati, A. M. Kamchatnov, Q. Glorieux, and N. Pavloff. Quantitative analysis of shock wave dynamics in a fluid of light. *Phys. Rev. Lett.*, 126:183901, May 2021.

[42] João D. Rodrigues, José T. Mendonça, and Hugo Terças. Turbulence excitation in counterstreaming paraxial superfluids of light. *Phys. Rev. A*, 101:043810, Apr 2020.

[43] M. J. Jacquet, T. Boulier, F. Claude, A. Maître, E. Cancellieri, C. Adrados, A. Amo, S. Pigeon, Q. Glorieux, A. Bramati, and E. Giacobino. Polariton fluids for analogue gravity physics. *Philosophical Transactions of the Royal Society A: Mathematical, Physical and Engineering Sciences*, 378(2177):20190225, 2020.

[44] Kali E. Wilson, Niclas Westerberg, Manuel Valiente, Callum W. Duncan, Ewan M. Wright, Patrik Öhberg, and Daniele Faccio. Observation of photon droplets and their dynamics. *Phys. Rev. Lett.*, 121:133903, Sep 2018.

[45] Chen-Lung Hung, Victor Gurarie, and Cheng Chin. From cosmology to cold atoms: Observation of sakharov oscillations in a quenched atomic superfluid. *Science*, 341(6151):1213–1215, 2013.

[46] Lars Onsager. Statistical hydrodynamics. *Il Nuovo Cimento (1943-1954)*, 6(2):279–287, 1949.

[47] P. Coullet, L. Gil, and F. Rocca. Optical vortices. *Optics Communications*, 73(5):403–408, 1989.

[48] Richard P Feynman. Chapter ii application of quantum mechanics to liquid helium. In *Progress in low temperature physics*, volume 1, pages 17–53. Elsevier, 1955.

[49] Andrey Nikolaevich Kolmogorov. The local structure of turbulence in incompressible viscous fluid for very large reynolds numbers. *Cr Acad. Sci. URSS*, 30:301–305, 1941.

[50] Robert H Kraichnan and David Montgomery. Two-dimensional turbulence. *Reports on Progress in Physics*, 43(5):547, 1980.

[51] Bill Halperin. *Progress in low temperature physics*. Elsevier, 2005.

[52] Jamil R Abo-Shaeer, Chandra Raman, Johnny M Vogels, and Wolfgang Ketterle. Observation of vortex lattices in bose-einstein condensates. *Science*, 292(5516):476–479, 2001.

[53] Kirk W Madison, Frédéric Chevy, Wendel Wohlleben, and Jean Dalibard. Vortex formation in a stirred bose-einstein condensate. *Physical review letters*, 84(5):806, 2000.

[54] Michikazu Kobayashi and Makoto Tsubota. Quantum turbulence in a trapped bose-einstein condensate. *Physical Review A*, 76(4):045603, 2007.

[55] E. A. L. Henn, J. A. Seman, G. Roati, K. M. F. Magalhães, and V. S. Bagnato. Emergence of turbulence in an oscillating bose-einstein condensate. *Phys. Rev. Lett.*, 103:045301, Jul 2009.

[56] Quentin Fontaine. Paraxial fluid of light in hot atomic vapors, 2020.

[57] Wenjie Wan, Shu Jia, and Jason W. Fleischer. Dispersive superfluid-like shock waves in nonlinear optics. *Nature Physics*, 3(1):46–51, Jan 2007.

[58] David Vocke, Thomas Roger, Francesco Marino, Ewan M. Wright, Iacopo Carusotto, Matteo Clerici, and Daniele Faccio. Experimental characterization of nonlocal photon fluids. *Optica*, 2(5):484–490, May 2015.

[59] Erwin Madelung. Quantentheorie in hydrodynamischer form. *Zeitschrift für Physik*, 40:322–326.

[60] T. Frisch, Y. Pomeau, and S. Rica. Transition to dissipation in a model of superflow. *Phys. Rev. Lett.*, 69:1644–1647, Sep 1992.

[61] Tyler W Neely, Edward Carlo Samson, Ashton S Bradley, Matthew J Davis, and Brian P Anderson. Observation of vortex dipoles in an oblate bose-einstein condensate. *Physical review letters*, 104(16):160401, 2010.

[62] Daniel A Steck. Rubidium 87 d line data. 2001.

[63] D Steck. Rubidium 85 d line data. 2019. *URL https://steck.us/alkalidata/rubidium85numbers. pdf.*

[64] Paul Siddons, Charles S Adams, Chang Ge, and Ifan G Hughes. Absolute absorption on rubidium d lines: comparison between theory and experiment. *Journal of Physics B: Atomic, Molecular and Optical Physics*, 41(15):155004, jul 2008.

[65] W. Zhao and P. Palffy-Muhoray. Z-scan technique using top-hat beams. *Applied Physics Letters*, 63(12):1613–1615, 1993.

[66] Cesar M Nascimento, Márcio A R C Alencar, Sabino Chávez-Cerda, Monique G A da Silva, Mario R Meneghetti, and Jandir M Hickmann. Experimental demonstration of novel effects on the far-field diffraction patterns of a gaussian beam in a kerr medium. *Journal of Optics A: Pure and Applied Optics*, 8(11):947–951, sep 2006.

[67] Omar Boughdad, Aurélien Eloy, Fabrice Mortessagne, Matthieu Bellec, and Claire Michel. Anisotropic nonlinear refractive index measurement of a photorefractive crystal via spatial self-phase modulation. *Opt. Express*, 27(21):30360–30370, Oct 2019.

[68] CF McCormick, DR Solli, RY Chiao, and JM Hickmann. Saturable nonlinear refraction in hot atomic vapor. *Physical Review A*, 69(2):023804, 2004.

[69] I. Shammass, S. Rinott, A. Berkovitz, R. Schley, and J. Steinhauer. Phonon dispersion relation of an atomic bose-einstein condensate. *Phys. Rev. Lett.*, 109:195301, Nov 2012.

[70] P. B. Blakie, R. J. Ballagh, and C. W. Gardiner. Theory of coherent bragg spectroscopy of a trapped bose-einstein condensate. *Phys. Rev. A*, 65:033602, Feb 2002.

[71] D. M. Stamper-Kurn, A. P. Chikkatur, A. Görlitz, S. Inouye, S. Gupta, D. E. Pritchard, and W. Ketterle. Excitation of phonons in a bose-einstein condensate by light scattering. *Phys. Rev. Lett.*, 83:2876–2879, Oct 1999.

[72] S. B. Papp, J. M. Pino, R. J. Wild, S. Ronen, C. E. Wieman, D. S. Jin, and E. A. Cornell. Bragg spectroscopy of a strongly interacting ^{85}Rb bose-einstein condensate. *Phys. Rev. Lett.*, 101:135301, Sep 2008.

[73] Nicholas David Birrell, Nicholas David Birrell, and PCW Davies. Quantum fields in curved space. 1984.

[74] Daniel J. Eisenstein and Charles L. Bennett. Cosmic sound waves rule. *Physics Today*, 61:44–50, 2008.

[75] Andrew R. Liddle and David H. Lyth. *Cosmological Inflation and Large-Scale Structure.* Cambridge University Press, 2000.

[76] Schrödinger, Erwin. The proper vibrations of the expanding universe. *PHYSICA*, 6(7-12):899–912, 1939.

[77] L. Parker. Particle creation in expanding universes. *Phys. Rev. Lett.*, 21:562–564, Aug 1968.

[78] Gerald T Moore. Quantum theory of the electromagnetic field in a variable-length one-dimensional cavity. *Journal of Mathematical Physics*, 11(9):2679–2691, 1970.

[79] Stefano Vezzoli, Arnaud Mussot, Niclas Westerberg, Alexandre Kudlinski, Hatef Dinparasti Saleh, Angus Prain, Fabio Biancalana, Eric Lantz, and Daniele Faccio. Optical analogue of the dynamical casimir effect in a dispersion-oscillating fibre. *Communications Physics*, 2(1):1–6, 2019.

[80] Stephen B Pope and Stephen B Pope. *Turbulent flows*. Cambridge university press, 2000.

[81] Paul A Hwang, David W Wang, Edward J Walsh, William B Krabill, and Robert N Swift. Airborne measurements of the wavenumber spectra of ocean surface waves. part i: Spectral slope and dimensionless spectral coefficient. *Journal of physical oceanography*, 30(11):2753–2767, 2000.

[82] Philipp Mösta, Christian D Ott, David Radice, Luke F Roberts, Erik Schnetter, and Roland Haas. A large-scale dynamo and magnetoturbulence in rapidly rotating core-collapse supernovae. *Nature*, 528(7582):376–379, 2015.

[83] A. N. Kolmogorov. The local structure of turbulence in incompressible viscous fluid for very large reynolds numbers. *Proceedings: Mathematical and Physical Sciences*, 434(1890):9–13, 1991.

[84] Arkady Tsinober. *An informal introduction to turbulence*, volume 63. Springer Science & Business Media, 2001.

[85] Lewis Fry Richardson. Atmospheric diffusion shown on a distance-neighbour graph. *Proceedings of the Royal Society of London. Series A, Containing Papers of a Mathematical and Physical Character*, 110(756):709–737, 1926.

[86] Paul M Chesler, Hong Liu, and Allan Adams. Holographic vortex liquids and superfluid turbulence. *Science*, 341(6144):368–372, 2013.

[87] PA Davidson. Turbulence; an introduction for scientists and engineers. oxford univ. 2004.

[88] Carlo Ferruccio Barenghi. Experiments on quantum turbulence. 1983.

[89] Russell J Donnelly and Charles E Swanson. Quantum turbulence. *Journal of Fluid Mechanics*, 173:387–429, 1986.

[90] Angela C White, Brian P Anderson, and Vanderlei S Bagnato. Vortices and turbulence in trapped atomic condensates. *Proceedings of the National Academy of Sciences*, 111(supplement_1):4719–4726, 2014.

[91] Carlo F Barenghi, Russell J Donnelly, and WF Vinen. *Quantized vortex dynamics and superfluid turbulence*, volume 571. Springer Science & Business Media, 2001.

[92] D Ian Bradley, DO Clubb, Shaun N Fisher, AM Guénault, Richard P Haley, CJ Matthews, George R Pickett, Viktor Tsepelin, and K Zaki. Decay of pure quantum turbulence in superfluid he 3- b. *Physical review letters*, 96(3):035301, 2006.

[93] WF Vinen. Quantum turbulence: achievements and challenges. *Journal of Low Temperature Physics*, 161(5):419–444, 2010.

[94] Andrew W Baggaley and Carlo F Barenghi. Vortex-density fluctuations in quantum turbulence. *Physical Review B*, 84(2):020504, 2011.

[95] Caroline Nore, Malek Abid, and ME Brachet. Kolmogorov turbulence in low-temperature superflows. *Physical review letters*, 78(20):3896, 1997.

[96] Cheng Chin, Rudolf Grimm, Paul Julienne, and Eite Tiesinga. Feshbach resonances in ultracold gases. *Reviews of Modern Physics*, 82(2):1225, 2010.

[97] Michikazu Kobayashi and Makoto Tsubota. Kolmogorov spectrum of superfluid turbulence: Numerical analysis of the gross-pitaevskii equation with a small-scale dissipation. *Physical review letters*, 94(6):065302, 2005.

[98] Narimasa Sasa, Takuma Kano, Masahiko Machida, Victor S L'vov, Oleksii Rudenko, and Makoto Tsubota. Energy spectra of quantum turbulence: Large-scale simulation and modeling. *Physical Review B*, 84(5):054525, 2011.

[99] R. Panico, P. Comaron, M. Matuszewski, A. S. Lanotte, D. Trypogeorgos, G. Gigli, M. De Giorgi, V. Ardizzone, D. Sanvitto, and D. Ballarini. Onset of vortex clustering and inverse energy cascade in dissipative quantum fluids, 2022.

[100] Nir Navon, Alexander L. Gaunt, Robert P. Smith, and Zoran Hadzibabic. Emergence of a turbulent cascade in a quantum gas. *Nature*, 539(7627):72–75, Nov 2016.

[101] E. A. L. Henn, J. A. Seman, E. R. F. Ramos, M. Caracanhas, P. Castilho, E. P. Olímpio, G. Roati, D. V. Magalhães, K. M. F. Magalhães, and V. S. Bagnato. Observation of vortex formation in an oscillating trapped bose-einstein condensate. *Phys. Rev. A*, 79:043618, Apr 2009.

[102] Uriel Frisch. *Turbulence: The Legacy of A. N. Kolmogorov*. Cambridge University Press, 1995.

[103] Robert H Kraichnan. Inertial ranges in two-dimensional turbulence. *The Physics of Fluids*, 10(7):1417–1423, 1967.

[104] Philip S Marcus. Numerical simulation of jupiter's great red spot. *Nature*, 331(6158):693–696, 1988.

[105] Maarten A Rutgers. Forced 2d turbulence: experimental evidence of simultaneous inverse energy and forward enstrophy cascades. *Physical review letters*, 81(11):2244, 1998.

[106] Volker Schweikhard, I Coddington, Peter Engels, Shihkuang Tung, and Eric A Cornell. Vortex-lattice dynamics in rotating spinor bose-einstein condensates. *Physical review letters*, 93(21):210403, 2004.

[107] Xavier Antoine, Weizhu Bao, and Christophe Besse. Computational methods for the dynamics of the nonlinear schrödinger/gross–pitaevskii equations. *Computer Physics Communications*, 184(12):2621–2633, 2013.

[108] Maciej Gałka, Panagiotis Christodoulou, Martin Gazo, Andrey Karailiev, Nishant Dogra, Julian Schmitt, and Zoran Hadzibabic. Emergence of isotropy and dynamic self-similarity in the birth of two-dimensional wave turbulence. *arXiv preprint arXiv:2203.09514*, 2022.

[109] Matthew T. Reeves, Thomas P. Billam, Brian P. Anderson, and Ashton S. Bradley. Inverse energy cascade in forced two-dimensional quantum turbulence. *Phys. Rev. Lett.*, 110:104501, Mar 2013.

[110] Rahil N Valani, Andrew J Groszek, and Tapio P Simula. Einstein–bose condensation of onsager vortices. *New Journal of Physics*, 20(5):053038, may 2018.

[111] Shaun P. Johnstone, Andrew J. Groszek, Philip T. Starkey, Christopher J. Billington, Tapio P. Simula, and Kristian Helmerson. Evolution of large-scale flow from turbulence in a two-dimensional superfluid. *Science*, 364(6447):1267–1271, 2019.

[112] Ashton S. Bradley and Brian P. Anderson. Energy spectra of vortex distributions in two-dimensional quantum turbulence. *Phys. Rev. X*, 2:041001, Oct 2012.

[113] Giorgio Krstulovic and Marc Brachet. Comment on "superfluid turbulence from quantum kelvin wave to classical kolmogorov cascades". *Physical review letters*, 105(12):129401, 2010.

[114] Angela C. White, Carlo F. Barenghi, and Nick P. Proukakis. Creation and characterization of vortex clusters in atomic bose-einstein condensates. *Phys. Rev. A*, 86:013635, Jul 2012.

[115] Shina Tan. Large momentum part of a strongly correlated fermi gas. *Annals of Physics*, 323(12):2971–2986, 2008.

Wei Liu **12 10 2022**

Sujet : Hydrodynamic effects in a paraxial fluid of light

Résumé : Le fluide quantique de la lumière désigne un gaz de photons en interaction faible qui est formé par un faisceau laser paraxial se propageant dans un milieu de Kerr non linéaire en remplaçant la coordonnée temporelle dans le fluide classique par la direction de propagation du faisceau. Il peut être considéré comme un fluide dont la densité est liée à l'intensité du champ, s'écoulant au gradient de la phase comme vitesse dans le plan perpendiculaire à la propagation le long de la coordonnée z de l'axe optique. Dans ce travail, des vapeurs chaudes de Rb comme milieu non linéaire ont été utilisées pour créer un tel fluide photonique. Trois expériences différentes ont été menées afin de déterminer le comportement hydrodynamique du fluide photonique. Tout d'abord, la spectroscopie de Bragg dans un fluide paraxial de lumière en imprimant des analogues de courtes impulsions de Bragg sur le fluide de photons a été mise en œuvre pour explorer le facteur de structure statique et la relation de dispersion de Bogoliubov. Ensuite, la réponse du fluide aux quenches quantiques, changement soudain d'interaction, a été réalisée pour étudier la création d'une particule cosmologique analogue. Enfin, la turbulence quantique a été étudiée dans deux fluides de lumière à contre-courant, signalant une signature claire d'un flux d'énergie cinétique des petites aux grandes échelles de longueur dans un fluide quantique via l'observation d'une loi d'échelle de Kolmogorov dans le spectre d'énergie cinétique incompressible. Tous ces éléments démontrent que le fluide photonique est une plateforme idéale pour explorer la dynamique hors équilibre.

Mots clés : Fluid of light, Kerr medium, Bragg-like spectroscopy, Quantum turbulence, Quantum vortices, Interaction quench, Hydrodynamic instability

Subject : Hydrodynamic effects in a paraxial fluid of light

Abstract: Quantum fluid of light refer to a weakly interacting gas of photons which is formed by a laser beam paraxial propagating through a non-linear Kerr medium by replacing the time coordinate in classical fluid to the beam's propagation direction. It can be considered as a fluid with density related to the field intensity, flowing at the gradient of the phase as velocity in the plane perpendicular to the propagation along optical-axis coordinate z. In this work, warm Rb vapors as nonlinear medium were used to create such a photon fluid. Three different experiments are carried to feature the hydrodynamics behaviour of photon fluid. First of all, Bragg-like spectroscopy in a paraxial fluid of light by imprinting analogues of short Bragg pulses on the photon fluid was implemented to explore the static structure factor and Bogoliubov dispersion relation. Second, the fluid's response to quantum quenches, sudden interaction change, was carried out to study the creation of analogue cosmological particle. Finally, quantum turbulence was studied in two counter-streaming fluids of light, report a clear signature of a flux of kinetic energy from small to large length scales in a quantum fluid via the observation of a Kolmogorov scaling law in the incompressible kinetic energy spectrum. All of these demonstrate that photon fluid is a ideal platform to explore the out of equilibrium dynamics.

Keywords : Fluid of light, Kerr medium, Bragg-like spectroscopy, Quantum turbulence, Quantum vortices, Interaction quench, Hydrodynamic instability